

# Varying-constant cosmology from hyperlight, coupled scalars

Masha Baryakhtar,<sup>1,\*</sup> Olivier Simon,<sup>2,3,4,†</sup> and Zachary J. Weiner<sup>1,‡</sup>

<sup>1</sup>*Department of Physics, University of Washington, Seattle, Washington, 98195, USA*

<sup>2</sup>*Princeton Center for Theoretical Science,*

*Princeton University, Princeton, New Jersey, 08544, USA*

<sup>3</sup>*Department of Physics, Princeton University, Princeton, New Jersey, 08544, USA*

<sup>4</sup>*Stanford Institute for Theoretical Physics,*

*Stanford University, Stanford, California, 94305, USA*

(Dated: Monday 20<sup>th</sup> May, 2024)

The fundamental constants at recombination can differ from their present-day values due to degeneracies in cosmological parameters, raising the possibility of yet-undiscovered physics coupled directly to the Standard Model. We study the cosmology of theories in which a new, hyperlight scalar field modulates the electron mass and fine-structure constant at early times. We find new degeneracies in cosmologies that pair early recombination with a new contribution to the matter density arising at late times, whose predictions can be simultaneously consistent with CMB and low-redshift distance measurements. Such “late dark matter” already exists in the Standard Model in the form of massive neutrinos, but is necessarily realized by the scalar responsible for shifting the early-time fundamental constants. After detailing the physical effects of varying constants and hyperlight scalar fields on cosmology, we find that variations of the electron mass and fine structure constant are constrained at the percent and permille level, respectively, and a hyperlight scalar in the mass range  $10^{-32}$  eV  $\lesssim m_\phi \lesssim 10^{-28}$  eV can impact what variations are allowed while composing up to a percent of the present dark matter density. We comment on the potential for models with a varying electron mass to reconcile determinations of the Hubble constant from cosmological observations and distance-ladder methods, and we show that parameter inference varies significantly between recent baryon acoustic oscillation and type Ia supernova datasets.

## CONTENTS

|   |    |
|---|----|
| I. Introduction                                 | 2  |
| II. Cosmology with varying constants            | 3  |
| A. Early-Universe signatures                    | 5  |
| B. Late-Universe signatures                     | 17 |
| III. Cosmology with coupled, hyperlight scalars | 20 |
| A. Impact on the cosmological background        | 21 |
| B. Impact on cosmological perturbations         | 24 |
| C. Parameter space                              | 27 |
| IV. Cosmological parameter inference            | 29 |
| A. Varying constants                            | 31 |
| B. Coupled, hyperlight scalars                  | 38 |
| C. Implications for cosmological concordance    | 44 |
| V. Conclusions                                  | 48 |

\* [mbaryakh@uw.edu](mailto:mbaryakh@uw.edu)

† [osimon@princeton.edu](mailto:osimon@princeton.edu)

‡ [zweiner@uw.edu](mailto:zweiner@uw.edu)

|   |    |
|---|----|
| Acknowledgments   | 50 |
| A. Numerical implementation of cosmological scalar fields | 50 |
| 1. Dynamics   | 51 |
| 2. Effective fluid treatment                              | 52 |
| 3. Initial conditions                                     | 56 |
| 4. Implementation details                                 | 56 |
| B. Parameter inference                                    | 58 |
| 1. Likelihoods  | 58 |
| 2. Sampling methods                                       | 59 |
| References  | 59 |

## I. INTRODUCTION

Cosmology is an essential frontier to study the dark sector and, at the same time, is a unique probe of the Standard Model and gravity at very early times. The cosmic microwave background (CMB) is largely governed by the physics of photon recombination and acoustic plasma waves, which in turn depend sensitively on quantum electrodynamics and thus the electromagnetic coupling strength and the electron mass in the early Universe. Some theories of physics beyond the Standard Model motivate variations of the fundamental physical constants over cosmological history; such microphysical models introduce new degrees of freedom which influence cosmological dynamics through gravity. The CMB anisotropies are also sensitive to all of the universe’s content through gravitation, both via cosmic expansion and gravitational potentials, and both during and after recombination.

Many previous studies of the CMB have placed limits on phenomenological variations of the fine-structure constant  $\alpha$  [1–12] and of the mass of the electron  $m_e$  [13–19] at recombination under the assumption that the gravitational effects of any new degrees of freedom are negligible. The possibility that fundamental constants—in particular, the electron mass—differed from their present-day values in the early Universe, triggering recombination earlier than standard, is also a candidate proposal [20–23] to reconcile determinations of the present-day expansion rate  $H_0$  as inferred by the CMB in  $\Lambda$ -cold-dark-matter ( $\Lambda$ CDM) cosmology with those based on local, distance-ladder measurements [24–26]. Early recombination alone is insufficient to explain observations of large-scale structure and type Ia supernovae in addition to the CMB, however; existing proposals therefore further invoke spatial curvature [21, 22]. Comparatively little literature has considered specific microphysical models responsible for the variations and investigated whether added matter content qualitatively alters the predicted cosmologies [27–31]. Implementing concrete theories is likewise imperative to understand the field evolution and the interplay of measurements throughout cosmic time—whether nucleosynthesis at earlier times, astrophysical probes at later times, or laboratory experiments today.

In this work and a companion article [32], we test models of a new scalar field that induces early-time shifts in fundamental constants against precision cosmological datasets. We specifically consider a massive, hyperlight field with particle mass  $10^{-32}$  eV  $\lesssim m_\phi \lesssim 10^{-28}$  eV whose Standard Model (SM) couplings effectively modulate the strength of electromagnetism and the mass of the electron. The scalar is produced as a cold, spatially homogeneous field in the early universe and makes up a subcomponent of cosmological dark matter today. In the mass range of interest, the amplitude of the scalar field is frozen until some point after recombination, after which it oscillates and decays; the fundamental constants thus take values before recombination that are constant in

space and time but different from their values today. Our work complements prior study of models akin to quintessence ( $m_\phi \lesssim 10^{-33}$  eV) in which  $\alpha$  varies via a coupling to the photon [33–35].

We show on semianalytic grounds that models with contributions to the matter density at late times—“late dark matter” scenarios—open up a novel degeneracy in the background cosmology that, taken at face value, has the potential to reconcile late-time observations with scenarios of early recombination. The scalar field conjectured to shift the values of constants naturally makes such a late contribution to dark matter, and so do massive neutrinos. The hyperlight scalar fields we consider also suppress structure formation to an extent controlled by their mass and abundance, yielding distinct signatures in the CMB that further test the scenario. We assess the interplay of these effects on quantitative constraints with a detailed analysis of cosmological data and study the effect of various dataset combinations. That the additional freedom of scalar field models allows for CMB observations and low-redshift distance measurements to be simultaneously satisfied in varying- $m_e$  scenarios was observed in the related analysis of Ref. [29], though without identifying its physical origin.

The outline of this paper is as follows. In Section II, we detail the physical impact of varying fundamental constants on the CMB and other cosmological observables. We devise a general set of parameter combinations that encode the main physical effects relevant to the CMB anisotropies in  $\Lambda$ CDM, including parameters that are typically fixed in standard analyses—not just the electron mass and fine-structure constant, but also the present-day CMB temperature, the helium yield, and the density of radiation beyond photons. We then discuss the distinct effects arising from a scalar field hypothesized to be responsible for the variations in the fundamental constants in Section III, considering the scalar’s purely gravitational effects and their interplay with varying constants. Section IV presents our inference of parameters within this extension to the standard cosmological model, comparing the results of scenarios with and without a scalar field. We also critically assess the concordance of current cosmological datasets within the context of cosmologies with a varying electron mass. We conclude in Section V, discussing the potential impact of near-term and future datasets and possible model extensions motivated by Ref. [32].

We use natural units in which  $\hbar = c = 1$  and define the reduced Planck mass  $M_{\text{pl}} \equiv 1/\sqrt{8\pi G} = 2.435 \times 10^{18}$  GeV. Repeated spatial indices (Latin characters) are implicitly summed regardless of their placement. We use upright boldface to denote spatial vectors. Unless otherwise specified, we fix a homogeneous, conformal-time Friedmann-Lemaître-Robertson-Walker (FLRW) spacetime with metric

$$g_{\mu\nu} \equiv a(\tau)^2 \eta_{\mu\nu} \quad (1.1)$$

where  $\eta_{\mu\nu}$  is the “mostly positive” Minkowski metric and  $a(\tau)$  the scale factor. We use primes to denote derivatives with respect to conformal time  $\tau$ . We occasionally work in terms of cosmic time  $t$  (defined by  $dt = a d\tau$ ), and use dots to denote  $t$  derivatives; the Hubble rate is  $H \equiv \dot{a}/a$ .

## II. COSMOLOGY WITH VARYING CONSTANTS

We begin by grounding our discussion with a detailed review of the impact of variations in fundamental constants on cosmology, seeking to quantify the parameter dependence of physical effects measured by cosmological data in the extended  $\Lambda$ CDM parameter space. We focus on the cases where the electron mass  $m_e$  and the fine-structure constant  $\alpha$  are different prior to recombination than at the present day; in this Section we do so without considering additional effects from any specific microphysical model thereof. We denote the constants’ early-time values as  $\alpha_i$  and  $m_{e,i}$ . We first discuss early-universe signatures, summarizing key parameter combinations that are well constrained by data and the resulting degeneracies in the physics up to and including

recombination. We then consider complementary probes of the late universe, after the recombination epoch.

As detailed in this Section, the usual flat  $\Lambda$ CDM model has sufficient parameter freedom to allow for the scale factor of recombination to differ substantially from the standard prediction without affecting the primary CMB anisotropies. In standard cosmology, the scale factor of recombination is fixed by the ratio of the CMB monopole temperature at the present time to that at photon last scattering,  $a_*/a_0 = T_0/T_*$ . The former is directly and precisely measured [36, 37], while the latter is determined by the standard atomic and thermal physics that govern recombination. This degeneracy direction has been explored in the context of the Hubble tension by changing  $T_*$  through variations of the early-time electron mass [21]. Separately, Ref. [38] reframed the Hubble tension as a (counterfactual, if illustrative) tension in the present-day CMB temperature  $T_0$ . Our discussion captures the arguments of Refs. [21, 38] in terms of the common physics from which they derive; we also comment on connections to the rescaling invariance of the Boltzmann and Einstein equations as explored in detail by Refs. [39–41].

Given that the CMB, baryon acoustic oscillations, and supernovae datasets we consider here are individually fit well by the  $\Lambda$ CDM model compared to any known extension thereof, our discussion centers on what degeneracies can be realized in extended parameter spaces that identically reproduce  $\Lambda$ CDM predictions. That is, we take the best-fit  $\Lambda$ CDM model as a proxy for the data itself and investigate correlated changes to parameters that leave its predictions invariant. Such a description is sufficient to anticipate whether an extension of  $\Lambda$ CDM might contain directions in parameter space that should be poorly constrained by data. However, only a quantitative analysis can assess whether a model’s additional freedom in fact improves upon the fit to individual datasets by explaining additional (possibly unanticipated) features in those data. We present the results of parameter inference in Section IV.

Throughout, we refer to the contributions of various species to the present-day, average energy density with the abundance parameters  $\omega_X = \bar{\rho}_{X,0}/3H_{100}^2 M_{\text{pl}}^2$ , where  $H_0 = h \cdot 100 \text{ Mpc}^{-1}\text{km/s} \equiv hH_{100}$ . Specifically,  $\omega_b$ ,  $\omega_c$ ,  $\omega_\Lambda$ ,  $\omega_\gamma$ , and  $\omega_\nu$  are the abundances of baryons, cold dark matter, dark energy, photons, and neutrinos, respectively. We also use  $\omega_m = \omega_b + \omega_c$  and  $\omega_r = \omega_\gamma + \omega_\nu$  to denote the total matter and radiation abundances, including contributions only from species that are nonrelativistic and relativistic at early times, respectively. The early-time energy density of neutrinos is typically quantified in terms of the effective number of degrees of freedom  $N_{\text{eff}}$  as

$$\omega_\nu = \frac{7}{8} \left( \frac{4}{11} \right)^{4/3} N_{\text{eff}} \cdot \omega_\gamma, \quad (2.1)$$

which accounts for the increase in the photon temperature relative to the neutrino temperature due to the entropy transferred from electrons and positrons when they annihilate. In standard cosmology, the neutrinos’ temperature is slightly enhanced by their residual coupling to the plasma during electron-positron annihilation; numerical solutions of the SM kinetic equations yield  $N_{\text{eff}} = 3.044$  [42–44].<sup>1</sup> If electron-positron annihilation occurs earlier (later) due to a heavier (lighter) electron, the neutrino temperature would be larger (smaller) than the SM prediction. However, this effect is small: over the range of electron-mass variations relevant to our main results (at most 20% in either direction), the relative change in  $N_{\text{eff}}$  is a few tenths of a percent [46, 47]. As differences of this size are smaller than the anticipated  $1\sigma$  sensitivity of future CMB experiments like CMB-S4 [48–50], we neglect this effect and fix  $N_{\text{eff}} = 3.044$ .

<sup>1</sup> Calculations of the final digit continue to be refined [45], including finite-temperature QED corrections and neutrino mass mixing [42–44].



## A. Early-Universe signatures

At linear order in perturbation theory, the effect of varying constants is entirely captured by accounting for their time dependence in the Thomson cross section and in the recombination equations whose solution gives the ionization history. These dynamics (implemented in CLASS [51, 52] and HyRec [53, 54]) constitute the focus of our analysis. Subleading effects include changes to the electrons’ and baryons’ energy densities through a varying electron mass and fine-structure constant, respectively. As electrons make up a small fraction  $\propto m_e/m_p \approx 1/1836$  of the total energy density in “baryonic” matter and the electromagnetic contribution to the nucleon masses is at the permille level [32], we neglect these corrections.

In Section II A 1, we study the effect of the fundamental constants on both when and how quickly recombination proceeds. The earlier recombination occurs, the less abundant dark matter and baryons are relative to radiation; Section II A 2 explains the resulting effect on the dynamics of the photon-baryon plasma. Photon diffusion (Section II A 3) is sensitive to the fundamental constants not only implicitly via the time recombination occurs but also explicitly via the Thomson cross section. In addition, the faster recombination occurs, the narrower the interval over which photons last scatter; Sections II A 3 and II A 4 discuss the resulting impact on small-scale damping and the generation of polarization. Finally, the earlier hydrogen recombines, the smaller the sound horizon is at last scattering. Section II A 5 shows how the distance to last scattering must compensate to preserve its manifestation in angular correlations on the sky. Drawing from these derivations, in Section II A 6 we discuss numerous degeneracies in extended  $\Lambda$ CDM parameter space for which the primary CMB anisotropies are completely (or partially) unchanged.

### 1. Recombination

The CMB observed today comprises photons that last scattered off electrons with a distribution in time determined by the physics of electrons recombining into neutral atoms and Thomson scattering. This distribution—the so-called visibility function—encodes both when (i.e., at what temperature) and over what redshift interval most CMB photons last scattered; both features directly impact the visible anisotropies in CMB temperature and polarization. The Thomson scattering rate is

$$\frac{d\kappa}{d\tau} \equiv a\bar{n}_e\sigma_T, \quad (2.2)$$

where the cross section  $\sigma_T = 8\pi\alpha_i^2/3m_{e,i}^2$  and  $\bar{n}_e$  is the number density of free electrons. The visibility function is then defined by

$$g(\tau) = \frac{d\kappa}{d\tau} \exp \left[ - \int_{\tau}^{\tau_0} d\tilde{\tau} \frac{d\kappa}{d\tilde{\tau}} \right]_{\tau=\tilde{\tau}} \equiv \kappa' e^{-\kappa} \quad (2.3)$$

[the latter equality defining  $\kappa(\tau)$  as the optical depth from today,  $\tau_0$ ]. We define the moment of recombination as the time of maximum visibility, with the scale factor of recombination  $a_*$  given by  $g_* \equiv g(\tau(a_*)) = \max g(\tau(a))$ . Quantities with a subscript star generally indicate those evaluated at recombination.

The dependence on the fundamental constants of the Thomson scattering cross section is manifest in its definition, but that of the electron ionization history is slightly more complex. The visibility function peaks roughly when the photons decouple from the plasma, which occurs when the Universe becomes nearly neutral. Defining the ionization fraction  $X_e \equiv \bar{n}_e/n_H$ , where  $n_H$  is the number

density of hydrogen nuclei, ionized and not, and neglecting the presence of helium (which effectively finishes recombining before hydrogen recombination begins),

$$\bar{n}_e = X_e \frac{(1 - Y_{\text{He}})\bar{\rho}_b}{m_{\text{H}}}. \quad (2.4)$$

Here  $Y_{\text{He}} \equiv \bar{\rho}_{\text{He}}/\bar{\rho}_b$  is the helium fraction by mass and  $m_{\text{H}}$  the mass of hydrogen. In spite of the complexities of the recombination process [53, 55–58], its dynamics largely depend on temperature relative to the ionization energy of hydrogen,  $E_I = \alpha_i^2 m_{e,i}/2$ . The temperature at recombination therefore scales as  $T_\star \propto \alpha_i^2 m_{e,i}$ , so

$$a_\star = \frac{T_0}{T_\star} \propto \frac{\sqrt[4]{\omega_\gamma}}{\alpha_i^2 m_{e,i}}. \quad (2.5)$$

The scale factor relative to that at recombination,  $x \equiv a/a_\star$ , proves to be the most convenient time coordinate with which to characterize the CMB anisotropies [21]. Moreover, writing the photon visibility as a dimensionless distribution over  $\ln x$ , i.e., as  $g/aH = e^{-\kappa} d\kappa/d\ln x$ , isolates superficial changes to its shape that only arise in a dimensionful form [e.g., over conformal time as in Eq. (2.3)]. Figure 1 depicts the effect of varying constants on the ionization history  $X_e$  and on the dimensionless visibility function; plotted against the scale factor relative to that of peak visibility, both are nearly indistinguishable when varying the electron mass by 15% in either direction. The rate of recombination increases more noticeably with the fine-structure constant, evident in the change to  $X_e(x)$  in Fig. 1, due to the more sensitive dependence of the effective rates of recombination, photoionization, etc., on  $\alpha_i$  [59, 60]. As a consequence, the visibility function narrows and broadens substantially more when varying the fine-structure constant than the electron mass (i.e., at a commensurate variation in  $a_\star$ ). We discuss the physical impacts of these changes to the visibility and ionization history and empirically determine their dependence on  $\alpha_i$  in Section II A 3. In addition,  $a_\star$  in Fig. 1 increases slightly faster than estimated from the ionization energy in Eq. (2.5)  $\alpha_i$ ; a numerical fit estimates  $a_\star \propto \alpha_i^{-2.08}$ .

## 2. Acoustic oscillations and matter effects

The dynamics of the photon-baryon plasma are primarily driven by three effects: the competition between radiation pressure and gravitational collapse, the increasing importance of matter to the expansion rate and gravitational potentials, and the damping of plasma oscillations on scales below the photons' mean free path. The semianalytic solutions of Ref. [61] (see also Ref. [62]) suggest that the Sachs-Wolfe, Doppler, and damping effects depend on cosmological parameters only through particular dimensionless combinations and depend on wave number only relative to the sound scale at recombination  $1/r_{s,\star}$ , to the comoving Hubble scale at matter-radiation equality  $k_{\text{eq}}$ , and to the effective damping scale  $k_{D,\star}$ . We discuss (and define) the role of each in turn.

The importance of baryons to the dynamics of the plasma is measured by the baryon-to-photon ratio

$$R(x) \equiv \frac{3\bar{\rho}_b}{4\bar{\rho}_\gamma} = R_\star x, \quad (2.6)$$

written in terms of that at recombination,  $R_\star \equiv 3\omega_b a_\star/4\omega_\gamma$ . Acoustic waves in the photon-baryon fluid travel with an effective sound speed

$$c_s(x) = \frac{1}{\sqrt{3}\sqrt{1+R(x)}}, \quad (2.7)$$

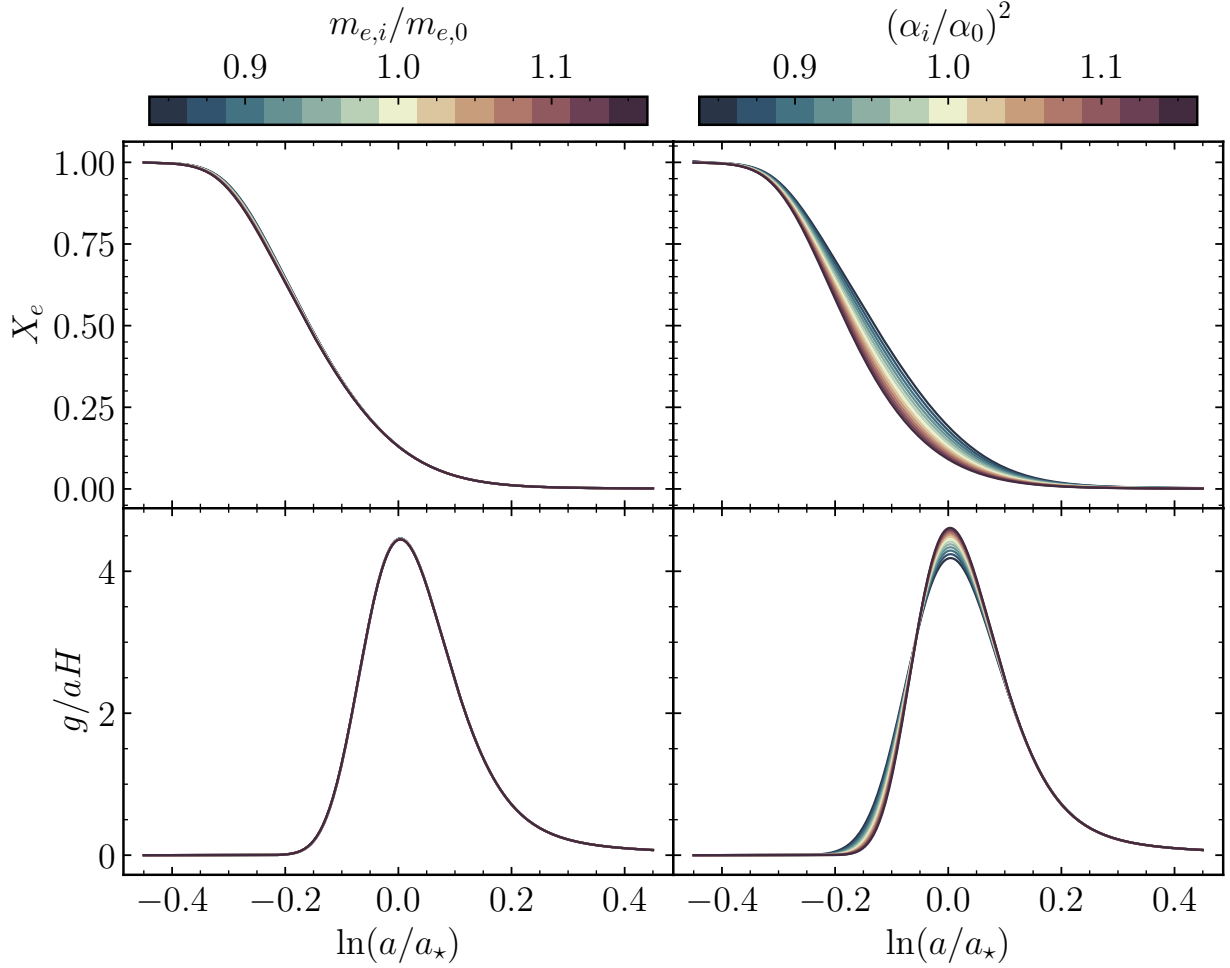


Figure 1. Impact on the ionization fraction (Eq. (2.4), top panels) and the dimensionless visibility function (Eq. (2.18), bottom panels) in cosmologies varying the electron mass  $m_{e,i}$  (left panels) and the fine-structure constant  $\alpha_i$  (right panels) by color. The colors on the right-hand panels label values of  $\alpha_i^2$  so that curves of the same color in the left-hand panels depict the same shift in the time of recombination. Results are plotted versus the logarithm of the scale factor relative to that when the visibility function peaks,  $a_*$ , to emphasize changes in dimensionless shape; these are negligible for varying  $m_{e,i}$  but significant for varying  $\alpha_i$ . Each curve varies  $\omega_b$  and  $\omega_c$  in proportion to  $1/a_*$  to keep baryon to photon and matter to radiation densities fixed at recombination (Section II A 2) and fixes the helium mass fraction  $Y_{\text{He}}$  (whose effect is discussed in Section II A 3). All results also fix the angular size of the sound horizon  $\theta_s$  (Section II A 5), a choice which has a negligible effect on these results.

with a corresponding sound horizon of

$$r_s(a) \equiv \int_0^a \frac{d\tilde{a}}{\tilde{a}} \frac{c_s(\tilde{a})}{\tilde{a}H(\tilde{a})} = \frac{a_*}{\sqrt{3}} \int_0^{a/a_*} dx \frac{1}{\sqrt{1 + R_*x}} \frac{1}{(a_*x)^2 H(x)}. \quad (2.8)$$

Independently of the physical extent of the sound horizon itself, the measured, relative heights of the acoustic peaks tightly constrain  $R_*$ . At recombination, dark energy is negligible and the Universe well described by matter and radiation alone. The latter term in the integrand of Eq. (2.8) thus takes the form

$$a^2 H = (a_*x)^2 H(x) = H_{100} \sqrt{\omega_r} \sqrt{1 + x/x_{\text{eq}}}, \quad (2.9)$$

where

$$x_{\text{eq}} = a_{\text{eq}}/a_{\star} \quad (2.10)$$

is the scale factor at equality relative to that at recombination. Since  $a_{\text{eq}}/a_0 = \omega_r/\omega_m$ ,  $x_{\text{eq}} = \bar{\rho}_{r,\star}/\bar{\rho}_{m,\star}$  measures the ratio of the radiation and matter densities at recombination. Because Eq. (2.9) is independent of  $a_{\star}$ , the sound horizon at recombination [Eq. (2.8)] is simply proportional to  $a_{\star}/\sqrt{\omega_r}$  if  $x_{\text{eq}}$  and  $R_{\star}$  are held fixed; indeed, in a matter-radiation Universe Eq. (2.8) takes the closed form [63]

$$r_{s,\star} = \frac{2a_{\star}\sqrt{x_{\text{eq}}/R_{\star}}}{H_{100}\sqrt{3\omega_r}} \ln \left( \frac{\sqrt{R_{\star}}\sqrt{1+x_{\text{eq}}} + \sqrt{1+R_{\star}}}{1 + \sqrt{R_{\star}x_{\text{eq}}}} \right), \quad (2.11)$$

which is exact in  $\Lambda$ CDM up to the  $\mathcal{O}(10^{-9})$  relative contribution from dark energy at recombination.

The relative importance of matter to gravity (at the background and perturbed level) at early times is fully characterized by when matter-radiation equality occurs relative to recombination ( $x_{\text{eq}}$ ). The heights of the peaks are sensitive to the onset of matter domination via the radiation driving effect [64, 65]: oscillations of the plasma are driven by the decay of the gravitational potentials at horizon crossing, but to a decreasing extent as the Universe becomes increasingly dominated by matter. The early integrated Sachs-Wolfe (early ISW) effect similarly depends on the time evolution of metric potentials as the Universe transitions from radiation domination, i.e., on  $x_{\text{eq}}$  only [66]. Moreover, in Universes that are well described by the matter-radiation solution, the full scale-dependent shape of these effects is identical for cosmologies with the same  $x_{\text{eq}}$ —a feature Ref. [67] emphasized as important beyond simply fixing the relative size of the sound horizon and the comoving horizon at equality. In particular, the comoving Hubble rate in a matter-radiation Universe is

$$aH = \frac{\sqrt{\omega_r}}{a_{\star}} \frac{H_{100}}{x_{\text{eq}}} \sqrt{(x/x_{\text{eq}})^{-2} + (x/x_{\text{eq}})^{-1}} \equiv \frac{k_{\text{eq}}}{\sqrt{2}} \sqrt{(x/x_{\text{eq}})^{-2} + (x/x_{\text{eq}})^{-1}}, \quad (2.12)$$

defining  $k_{\text{eq}}$  as the comoving Hubble scale at equality ( $x = x_{\text{eq}}$ ). Just like the sound horizon, the comoving horizon at equality ( $1/k_{\text{eq}}$ ) scales with  $a_{\star}/\sqrt{\omega_r}$  if  $x_{\text{eq}}$  is held fixed, situating all associated features at the same relative scales.

In sum, the shape of the CMB power spectrum by itself measures relative energy densities at recombination, constraining the parameter combinations  $R_{\star} \propto \omega_b a_{\star}/\omega_{\gamma}$  and  $x_{\text{eq}} \propto \omega_r/\omega_m a_{\star}$ . These combinations may be held fixed trivially because  $\omega_b$  and  $\omega_c = \omega_m - \omega_b$  are free parameters in standard cosmology, in which case  $r_{s,\star}k_{\text{eq}}$  is constant. These phenomena alone are therefore unable to discern whether the photon temperature today or at recombination differ from the SM prediction [Eq. (2.5)], or even if the radiation density  $\omega_r$  is different than that from photons and neutrinos as predicted in the SM.

### 3. Small-scale damping

Fluctuations in the plasma are damped on small scales by two distinct effects, one due to photon diffusion and the other due to the finite duration of recombination. We consider each of their parameter dependence in turn. The damping scale associated to photon diffusion is [68, 69]

$$\frac{1}{k_{D,\star}^2} \equiv \int_0^1 \frac{dx/x}{(a_{\star}xH)^2} \frac{R^2 + 16(1+R)/15}{6(1+R)^2} \left( \frac{d\kappa}{d\ln x} \right)^{-1}. \quad (2.13)$$

The baryon-to-photon ratio  $R$  is invariant as a function of  $x$  in cosmologies with the same value for  $R_\star$ . Because the Thomson scattering rate per  $e$ -fold,  $d\kappa/d\ln x = \bar{n}_e\sigma_T/H$ , is dimensionless, the comoving diffusion scale  $k_{D,\star}$  is proportional to  $k_{\text{eq}}$  [Eq. (2.12)] at fixed  $x_{\text{eq}}$ . Whether or not  $k_{D,\star}/k_{\text{eq}}$  varies with parameters is therefore determined by the dimensionless Thomson scattering rate.

Inserting the definition of free electron number density  $\bar{n}_e$ , Eq. (2.4), and rewriting the baryon abundance in terms of  $R_\star$  gives

$$\frac{d\kappa}{d\ln x} = \frac{n_e(x)\sigma_T}{H} = \frac{R_\star K_\star}{x_{\text{eq}}} \frac{X_e(x)}{\sqrt{(x/x_{\text{eq}})^2 + (x/x_{\text{eq}})^3}} \quad (2.14)$$

where

$$K_\star \equiv 4H_{100}M_{\text{pl}}^2 \frac{\sqrt{\omega_\gamma}\sigma_T}{a_\star^2} \sqrt{\frac{\omega_\gamma}{\omega_r} \frac{1 - Y_{\text{He}}}{m_{\text{H}}}} \quad (2.15)$$

is a rescaling of the Thomson scattering rate at recombination that encodes its parameter dependence complementary to that of  $R_\star$ ,  $x_{\text{eq}}$ , and the ionization history. In more detail, the acoustic dynamics of the plasma (Section II A 2) motivate expressing the density of electron scatterers relative to the photon energy density at recombination, i.e., in terms of the baryon-to-photon ratio  $R_\star$  via  $n_e \propto R_\star x \rho_\gamma = R_\star \rho_{\gamma,\star}/x^4$ . The impact of matter on plasma dynamics suggests expressing the Hubble rate in terms of the (square root of) the total radiation density and encoding the matter contribution with  $x_{\text{eq}}$  as  $H \propto \sqrt{\rho_{r,\star}/x^4} \sqrt{1 + x/x_{\text{eq}}}$ . Their ratio yields an overall dependence on  $\sqrt{\rho_{\gamma,\star}} \propto \sqrt{\omega_\gamma}/a_\star^2 \propto T_\star^2$  times the square root of the fraction of the total radiation density in photons. Finally, the factor of  $(1 - Y_{\text{He}})/m_{\text{H}}$  in Eq. (2.15) simply translates the total number density of baryons to that of electrons that do not recombine into helium.

If the ionization history  $X_e$  is unchanged as a function of  $x$  and both  $R_\star$  and  $x_{\text{eq}}$  are fixed, then the full  $x$  dependence of the integrand of Eq. (2.13) is unchanged. The diffusion damping scale then scales in tandem with  $k_{\text{eq}}$  and  $1/r_{s,\star}$  if  $K_\star$  is fixed. Inserting Eq. (2.5) for  $a_\star$ ,

$$K_\star \propto \alpha_i^6 \sqrt{\frac{\omega_\gamma}{\omega_r} \frac{1 - Y_{\text{He}}}{m_{\text{H}}/M_{\text{pl}}}} \quad (2.16)$$

At fixed  $K_\star$ ,  $x_{\text{eq}}$ , and ionization history, the impact of diffusion damping on CMB anisotropies is independent of both the early-time electron mass  $m_{e,i}$  and the present photon temperature  $T_0$ . Namely, the increase of the electron density relative to the Hubble rate with  $T_\star^2 \propto m_{e,i}^2 \alpha_i^4$  compensates the Thomson cross section's inverse dependence on  $m_{e,i}^2$  but compounds with its proportionality to  $\alpha_i^2$ . The irrelevance of  $T_0$  merely reflects that diffusion damping only depends on the properties of the Universe during recombination, not on the expansion that has elapsed since then. Equation (2.16) further encodes the salient dependence of the diffusion scale on the helium yield and the effective number of neutrino species [Eq. (2.1)].

The diffusion parameter  $K_\star$  captures the relevant parameter dependence of diffusion damping, except for any incurred impact to the ionization history; Fig. 1 shows that this effect is negligible when varying  $m_{e,i}$  but not  $\alpha_i$ . The damping scale involves an integral over  $X_e$ , and to the extent that  $\alpha_i$  simply rescales  $X_e$ , we could estimate  $k_{D,\star} \propto \sqrt{X_e}$  (on top of its other parameter dependence). However, in the short interval before recombination ( $\Delta \ln a \sim 0.4$ ),  $X_e/X_{e,\Lambda\text{CDM}}$  varies rapidly in proportionality between  $\alpha_i^0$  and  $\alpha_i^{-5}$  (with  $R_\star$  and  $x_{\text{eq}}$  fixed); the net effect on the damping scale is an integral over this variation. Changes to the ionization history therefore cancel some of the direct dependence of the damping scale on  $\alpha_i$  in  $K_\star$ . We determine empirically that  $a_\star k_{D,\star} \sim \alpha_i^{1.63}$  at fixed  $Y_{\text{He}}$ . Similarly, the helium mass fraction  $Y_{\text{He}}$  enters both directly in the Thomson scattering rate and through its effect on the ionization history, which does shift appreciably. Leading up to

recombination,  $X_e$  varies rapidly in proportionality between  $(1 - Y_{\text{He}})^0$  and  $(1 - Y_{\text{He}})^{-0.8}$ , reducing the damping scale's overall dependence on  $Y_{\text{He}}$  just as for  $\alpha_i$ . We compute that  $a_\star k_{D,\star} \propto (1 - Y_{\text{He}})^{0.24}$  in total. Moreover, the helium mass fraction is also itself sensitive to  $\alpha_i$  and  $m_{e,i}$  through the dynamics of nucleosynthesis. We derive the dependence of  $Y_{\text{He}}$  on parameters in Ref. [32], leading to  $a_\star k_{D,\star} \sim \alpha_i^{1.42}$ . The helium mass fraction scales much more weakly with the electron mass, leading to  $a_\star k_{D,\star} \propto m_{e,i}^{-0.05}$ .

The second effect that damps small-scale CMB power is due to the nonzero width of the visibility function, which effectively averages rapidly oscillating modes over multiple oscillations [61, 69]. This effect is referred to as Landau damping for its analogy to the damping of oscillations comprising a spread of frequencies. Approximating the visibility function as a Gaussian about its peak as  $g(\tau) \approx \exp(-[\tau - \tau_\star]^2 / 2\sigma_g^2) / \sqrt{2\pi}\sigma_g$ , the comoving width of the last-scattering surface may be approximated by  $\sigma_g = 1/\sqrt{2\pi}g_\star$ . However,  $\sigma_g$  (as an interval in conformal time) also depends explicitly on the expansion rate at recombination, which, for example, is larger for earlier recombination. The effect solely due to the shape of the visibility function is captured by the width of the visibility function relative to  $aH$  (i.e., as a dimensionless distribution over  $\ln x$ ), which is approximately  $a_\star H_\star / \sqrt{2\pi}g_\star$ . The effective Landau damping scale is then most conveniently parameterized as [61]

$$k_L = \frac{\sqrt{6(1 + R_\star)}}{\sigma_g} = \frac{\sqrt{\omega_r}}{a_\star} H_{100} \frac{g_\star}{a_\star H_\star} \sqrt{12\pi(1 + R_\star)(1 + x_{\text{eq}}^{-1})}. \quad (2.17)$$

To the extent that  $X_e$  is a fixed function of  $x$  (such that  $g_\star/a_\star H_\star$  is unchanged) the Landau damping scale is proportional to the aforementioned physical scales at fixed  $R_\star$  and  $x_{\text{eq}}$ .

Figure 1 shows that  $g_\star/a_\star H_\star$  is effectively independent of  $m_{e,i}$  (scaling only  $\sim m_{e,i}^{-0.01}$ ); we empirically find that varying  $\alpha_i$  and  $Y_{\text{He}}$  independently yields

$$\frac{g_\star}{a_\star H_\star} \approx 4.45 \left( \frac{\alpha_i}{\alpha_0} \right)^{0.61} \left( \frac{1 - Y_{\text{He}}}{1 - 0.245} \right)^{0.11} \quad (2.18)$$

at fixed  $R_\star$  and  $x_{\text{eq}}$ . Therefore,  $r_{s,\star} k_L$  scales with roughly one fewer power of  $\alpha_i$  than does  $r_{s,\star} k_{D,\star}$ . Since the Landau and diffusion damping scales are of similar size (and combine in quadrature), measurements of the damping tail do not cleanly translate to measurements of either of the individual parameter combinations in Eqs. (2.16) and (2.18); however, CMB polarization is independently sensitive to  $g_\star/a_\star H_\star$  as discussed next.

#### 4. Polarization

The amplitude of the CMB polarization spectrum relative to the temperature spectrum is also sensitive to the duration of recombination [69]. Polarization is generated by Thomson scattering when the temperature distribution has a nonnegligible quadrupole. The quadrupole is sourced by the dipole of the distribution, which is itself proportional to the time derivative of the temperature fluctuation (the monopole) [69, 70]. Efficient Thomson scattering, however, impedes the growth of anisotropy (like the quadrupole). The observed CMB polarization is thus generated as the photons decouple, when scattering still occurs and generates polarization but not so frequently that the quadrupole is suppressed.

The average interval between scatterings around decoupling is comparable to the width of the visibility function and sets the relative amplitude of the polarization and temperature perturbations proportional to  $c_s k \sigma_g$ —i.e., truly instantaneous recombination generates no polarization. In other words, the longer recombination takes, the more the quadrupole of the temperature distribution is able to grow, generating greater polarization at last scattering. (Incidentally, the amplitude of the



polarization spectrum is also sensitive to the baryon-to-photon ratio  $R_\star$  via the factor of the sound speed  $c_s$ .) Thus, the polarization amplitude uniquely probes the width of the visibility function, with parameter dependence given by Eq. (2.18). Ref. [71] provides subpercent-level constraints directly on the width of the visibility function, introduced as a phenomenological extension of the  $\Lambda$ CDM model; the constraints are driven to a comparable extent by the effects on Landau damping and on the amplitude of the polarization spectrum. We therefore expect CMB polarization data to provide complementary constraining power on variations in the fine-structure constant. Because the shape of the visibility function varies negligibly with the electron mass (per Fig. 1), we further anticipate that polarization offers no unique information for electron-mass variations compared to temperature data.

### 5. Angular power spectra

The angular power spectrum of the CMB measures the scale of the aforementioned features—the sound horizon, the horizon at equality, and the diffusion and Landau damping scales—only relative to the transverse comoving distance to last scattering. In  $\Lambda$ CDM cosmologies with nonzero curvature  $\Omega_k$ , the transverse comoving distance is [72]

$$D_M(a) \equiv \chi(a) \operatorname{sinc} \left[ \sqrt{-\Omega_k} \frac{\chi(a)}{1/H_0} \right], \quad (2.19)$$

where the line-of-sight comoving distance is

$$\chi(a) = \int_a^{a_0} \frac{d\tilde{a}}{\tilde{a}} \frac{1}{\tilde{a}H(\tilde{a})}. \quad (2.20)$$

The transverse distance reduces to the line-of-sight one [ $D_M(a) = \chi(a)$ ] for zero curvature, which we assume for the remainder of the paper. In a Universe with only matter and dark energy, characterized by a scale factor of matter- $\Lambda$  equality  $a_{m-\Lambda} = \sqrt[3]{\omega_m/\omega_\Lambda}$  and a Hubble constant  $h = \sqrt{\omega_m + \omega_\Lambda}$ , the comoving distance Eq. (2.20) integrates to [73]

$$\chi(a) = \frac{2}{\sqrt{\omega_m} H_{100}} [F_M(1; a_{m-\Lambda}) - F_M(a; a_{m-\Lambda})], \quad (2.21)$$

where

$$F_M(a; a_{m-\Lambda}) \equiv \sqrt{a} \cdot {}_2F_1(1/6, 1/2; 7/6, -[a/a_{m-\Lambda}]^3) \quad (2.22)$$

and  ${}_2F_1$  is a hypergeometric function.

The precisely measured angular extent of the sound horizon is a ratio of two scales,  $\theta_s = r_{s,\star}/D_{M,\star}$ , that each depend only on early- or late-time physics. The support of the comoving distance integral in Eq. (2.20) is dominated at late times around matter- $\Lambda$  equality, since  $aH$  decreases in the matter era but increases in dark-energy domination; the sound horizon Eq. (2.8) is of course only sensitive to early times, dominated by the period shortly before recombination. Attempts to explain the discrepancy in  $H_0$  inferences are thus typically categorized as early-time or late-time solutions [74].

The sound horizon at recombination Eq. (2.11) may be written as

$$r_{s,\star} = \frac{2a_\star}{H_{100}\sqrt{3\omega_r}} F_{r_s}(R_\star, x_{\text{eq}}), \quad (2.23)$$

where the dependence on  $x_{\text{eq}}$  and  $R_\star$ , which are constrained by the shape of the CMB power spectrum (Section II A 2), scales as  $F_{r_s}(R_\star, x_{\text{eq}}) \propto x_{\text{eq}}^{0.247} R_\star^{-0.0964}$  when numerically approximated

about the best-fit  $\Lambda$ CDM parameters [75]. The comoving distance to last scattering does not depend explicitly upon either  $a_*$  or  $\omega_r$  but does so implicitly via the matter density when holding  $x_{\text{eq}}$  fixed. Replacing  $\omega_m$  in Eq. (2.21) with  $\omega_r/a_*x_{\text{eq}}$  and taking the limit of a matter Universe, for which  $F_M(a; a_{m-\Lambda} \rightarrow \infty) \rightarrow \sqrt{a}$ ,  $\chi_* \approx \chi(0) = 2\sqrt{a_*x_{\text{eq}}}/\sqrt{\omega_r}H_{100}$ . In this limit,  $\theta_s = \sqrt{a_*}F_{r_s}(R_*, x_{\text{eq}})/\sqrt{3x_{\text{eq}}} \propto \sqrt{a_*}/x_{\text{eq}}^{0.253}R_*^{0.0964}$ . In reality,  $F_M(1; a_{m-\Lambda}) \propto (\sqrt{\omega_m}/h)^{0.193}$  about the best-fit  $\Lambda$ CDM cosmology, which encodes the correction to the distance to last scattering in Universes due to dark energy. Substituting for  $\omega_m$  as above [and accounting for the small difference between  $\chi_*$  and  $\chi(0)$ ],

$$r_{s,*} \propto \frac{a_*}{\sqrt{\omega_r}} x_{\text{eq}}^{0.247} R_*^{-0.0964} \quad (2.24)$$

and

$$\chi_* \propto \omega_m^{-0.403} h^{-0.193} a_*^{-0.0173} = \frac{a_*}{\sqrt{\omega_r}} \left( \frac{\sqrt{\omega_r}}{a_*^{3.18} h} x_{\text{eq}}^{2.09} \right)^{1/5.173}. \quad (2.25)$$

Combining the two generalizes the well-known dependence of  $\theta_s$  on cosmological parameters [75–77] to

$$\theta_s \propto \left( \frac{a_*^{3.18} h}{\sqrt{\omega_r}} x_{\text{eq}}^{-0.810} R_*^{-0.499} \right)^{1/5.173} \propto \left( \frac{T_0^{1.18} h}{\alpha_i^{6.36} m_{e,i}^{3.18} \sqrt{\frac{\omega_\gamma}{\omega_r}} x_{\text{eq}}^{-0.810} R_*^{-0.499}} \right)^{1/5.173}, \quad (2.26)$$

the second proportionality substituting for  $a_*$  with Eq. (2.5). Within the  $\Lambda$ CDM model,  $a_*$  is effectively fixed and *Planck* [75] measures  $x_{\text{eq}}$  and  $R_*$  with roughly 0.9% and 0.7% uncertainty, respectively, while  $\theta_s$  is measured with a comparatively negligible 0.03% uncertainty. Holding  $T_0$  and  $\omega_r/\omega_\gamma$  fixed, the uncertainty on  $x_{\text{eq}}$  therefore translates to a  $\sim 0.7\%$  uncertainty on  $h$ , an estimate reproduced in full parameter inference.

Any given parameterization of the primordial power spectrum must be rescaled to account for the shift in correspondence between wave number (in arbitrary units) and the scales that characterize the physical effects discussed above. The standard power-law model,

$$\Delta_{\mathcal{R}}^2(k) = A_s \left( \frac{k}{k_p} \right)^{n_s-1}, \quad (2.27)$$

is overparameterized with a normalization  $A_s$  and pivot scale  $k_p$ , the latter of which is conventionally fixed. Thus, instead of taking  $k_p$  to scale in tandem with other scales in the problem (i.e. in proportion to  $\sqrt{\omega_r}/a_*$ ), we choose  $A_s$  to fix the value of  $A_s (\sqrt{\omega_r}/a_*)^{n_s-1}$ . Note that, because the Universe reionizes at late times, the observed amplitude of CMB anisotropies is suppressed by a further factor of  $e^{-2\tau_{\text{reion}}}$ , where  $\tau_{\text{reion}}$  is the optical depth to reionization. CMB observations on small scales therefore only constrain the combination  $A_s e^{-2\tau_{\text{reion}}}$ , but reionization also enhances CMB polarization on large scales (multipoles  $\ell \lesssim 30$ ), breaking this degeneracy.

## 6. Degeneracies of the early Universe

We now summarize what parameter directions leave the primary CMB anisotropies invariant per the preceding discussion. Namely, we identify degeneracies that preserve the relative abundance of baryons and photons at recombination,

$$R_* = \frac{3\rho_{b,*}}{4\rho_{\gamma,*}} \propto \frac{3\omega_b}{4\omega_\gamma} \frac{T_0}{\alpha_i^2 m_{e,i}} \propto \frac{3\omega_b}{4\alpha_i^2 m_{e,i} T_0^3} \quad (2.28a)$$

the relative abundance of matter and radiation at recombination,

$$x_{\text{eq}} = \frac{\rho_{r,\star}}{\rho_{m,\star}} \propto \frac{\omega_r}{\omega_m} \frac{\alpha_i^2 m_{e,i}}{T_0} \propto \frac{\alpha_i^2 m_{e,i} T_0^3}{\omega_m} \frac{\omega_r}{\omega_\gamma} \quad (2.28b)$$

the Thomson scattering rate per Hubble time,

$$K_\star \propto \alpha_i^6 \sqrt{\frac{\omega_\gamma}{\omega_r}} \frac{1 - Y_{\text{He}}}{m_{\text{H}}/M_{\text{pl}}}, \quad (2.28c)$$

the width of the dimensionless visibility function,

$$\frac{g_\star}{a_\star H_\star} \propto \alpha_i^{0.61} (1 - Y_{\text{He}})^{0.11} \quad (2.28d)$$

and the angular size of the sound horizon,

$$\theta_s \propto \left( \frac{T_0^{1.18} h}{\alpha_i^{6.36} m_{e,i}^{3.18}} \sqrt{\frac{\omega_\gamma}{\omega_r}} x_{\text{eq}}^{-0.810} R_\star^{-0.499} \right)^{1/5.173}. \quad (2.28e)$$

Equation (2.28) takes the scale factor of recombination to be proportional to  $T_0/\alpha_i^2 m_{e,i}$ , per Eq. (2.5). When all of these parameter combinations and the ionization history are fixed, all the scales that encode early-Universe physics—the inverse sound horizon  $1/r_{s,\star}$ , the horizon at equality  $k_{\text{eq}}$ , the diffusion damping scale  $k_{D,\star}$ , and the Landau damping scale  $k_L$ —scale in proportion to  $\sqrt{\omega_r}/a_\star \propto \alpha_i^2 m_{e,i} T_0 \sqrt{\omega_r/\omega_\gamma}$ .

Figure 2 illustrates the phenomenological impact of varying  $R_\star$ ,  $x_{\text{eq}}$ , and  $\theta_s$  on the CMB temperature power spectrum  $C_\ell^{TT}$  and in particular demonstrates the degeneracy achieved under varying  $m_{e,i}$ . The role played by baryons in acoustic oscillations is clear in the panel varying  $R_\star$ : the relative heights of the first peaks and troughs are reduced at larger  $m_{e,i}$ , for which  $R_\star \propto a_\star \propto m_{e,i}^{-1}$ , and therefore the amplitude of acoustic oscillations, is smaller. Next, if recombination happens closer to matter-radiation equality (as it does if a larger  $m_{e,i}$  triggers recombination earlier, all else equal), radiation has a larger effect on gravity; around recombination, the metric potentials therefore decay relatively faster at horizon entry, increasing the driving of acoustic oscillations. In addition, the decay of the potentials due to radiation enhances the early ISW effect for earlier recombination, since they are constant in a Universe with only cold dark matter. Finally, Fig. 2 shows that holding both  $R_\star$  and  $x_{\text{eq}}$  fixed but not  $\theta_s$  (i.e., holding  $h$  constant instead) effectively shifts the entire spectrum to larger multipoles when recombination happens earlier.

The impact of the remaining parameters on CMB polarization and on small-scale anisotropies is illustrated well when varying  $\alpha_i$ , shown in Fig. 3. The impact of small-scale damping on both temperature and polarization anisotropies is dramatic: the Thomson scattering rate increases more rapidly than the Hubble rate with the fine-structure constant, pushing the effects of diffusion damping to smaller scales (and therefore larger multipoles). In addition, recalling Fig. 1, the dimensionless visibility function also narrows with larger  $\alpha_i$ , reducing the degree of Landau damping. A narrower visibility function also reduces the amplitude of polarization, which is most evident at  $\ell \lesssim 800$  in the middle-left and lower-left panels of Fig. 3; at larger multipoles, the reduction in damping overcomes this suppression. The  $m_{e,i}$ -independence of diffusion damping, Landau damping, and the generation of polarization at fixed  $R_\star$ ,  $x_{\text{eq}}$ , and  $\theta_s$  is evident in the right panels of Fig. 3, where the changes to the CMB spectra are imperceptible even for 15% changes to the early-time electron mass.

The preceding discussion facilitates the interpretation of degeneracies in a variety of proposed extensions to  $\Lambda$ CDM. The degeneracies in scenarios featuring early recombination via varying

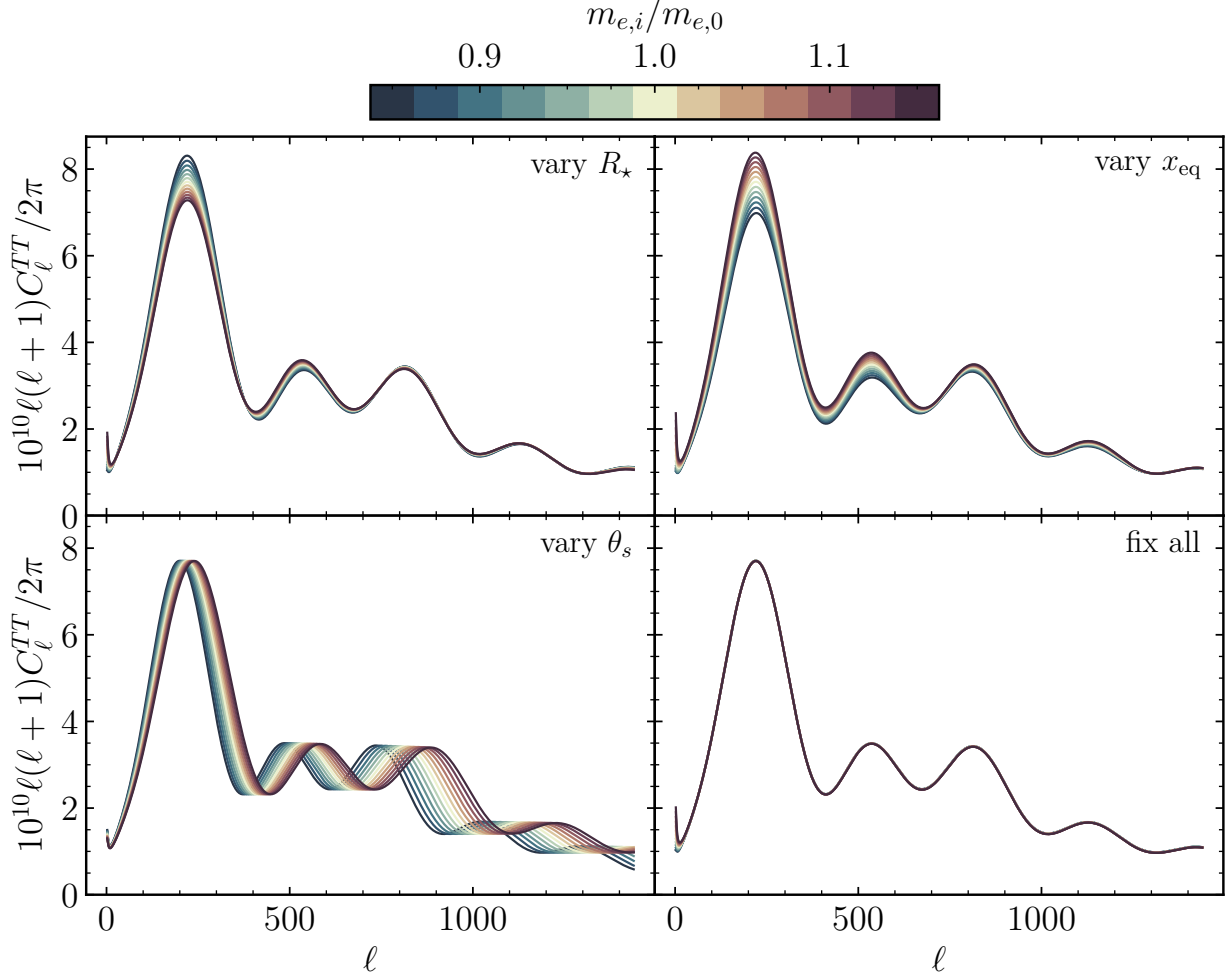


Figure 2. CMB temperature power spectrum in cosmologies varying the electron mass  $m_{e,i}$  by color and holding various combinations of  $R_\star$  [Eq. (2.6)],  $x_{\text{eq}}$  [Eq. (2.10)], and  $\theta_s$  [Eq. (2.26)] fixed to their values in the best-fit  $\Lambda$ CDM cosmology [75]. The top-left and top-right panels fix all but  $R_\star$  and  $x_{\text{eq}}$ , respectively, illustrating the impact of changing ratios of energy densities at recombination. The bottom-left panel varies  $\theta_s$ , shifting the spectrum to larger multipoles when recombination occurs earlier. The bottom-right panel fixes them all, leaving the spectrum largely unchanged. The angular size of the sound horizon is set by choosing  $h$  via numerical optimization; the bottom-left panel simply fixes  $h$ . Each panel also fixes the helium mass fraction  $Y_{\text{He}}$ , the combination  $A_s a_\star^{1-n_s}$ , and the optical depth to reionization  $\tau_{\text{reion}}$ .

constants, discussed in Ref. [21], fix  $R_\star$  and  $x_{\text{eq}}$  by taking constant  $a_\star \omega_b$  and  $a_\star \omega_m$ , as discussed in Section II A 2. Per Eq. (2.26), holding  $\theta_s$  constant then requires  $h \propto a_\star^{-3.18}$ , as found in Ref. [21]. As demonstrated in Ref. [21] and Section II A 3, no additional parameter freedom is required to preserve the diffusion damping scale only when varying the electron mass, for which  $a_\star \propto m_{e,i}^{-1}$ . Furthermore, the ionization history is effectively invariant (as a function of  $a/a_\star$ ) only under varying  $m_{e,i}$ , in which case the diffusion and Landau damping scales imprint at the same angular scale on the sky (i.e.,  $r_{s,\star} k_{D,\star}$  and  $r_{s,\star} k_L$  invariant) and polarization is generated with the same amplitude, as evident in Fig. 3. We therefore expect that early-time variations in the fine-structure constant are much more severely constrained by primary CMB data than the electron mass.

Another class of early-recombination models postulates substantial small-scale inhomogeneities in the baryon distribution, which enhance the recombination rate [78–81]. These changes, however,

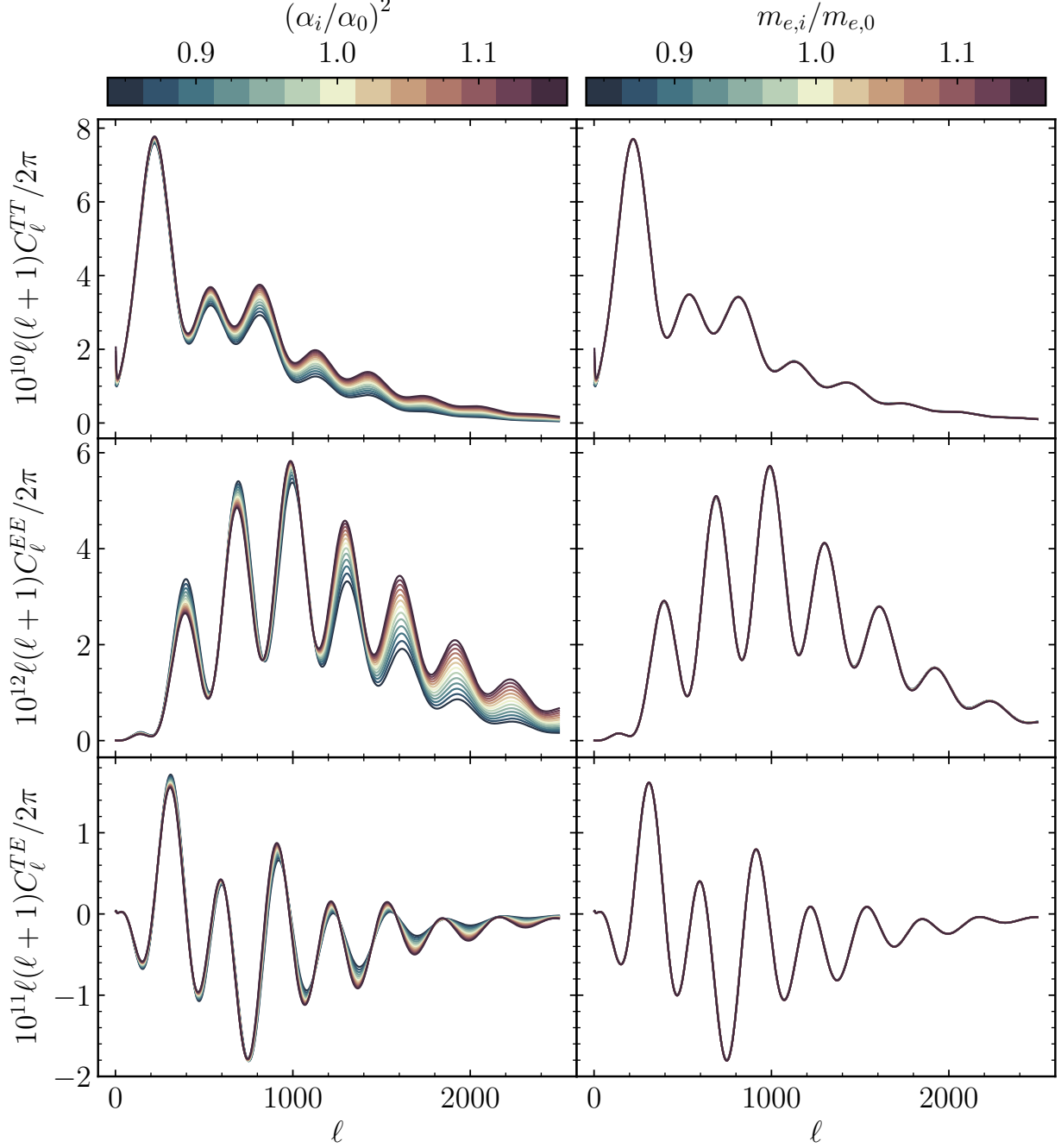


Figure 3. CMB temperature (top panels) and  $E$ -mode (middle panels) auto power spectra and their correlation (bottom panels) in cosmologies varying the fine-structure constant  $\alpha_i$  (left panels) or the electron mass  $m_{e,i}$  (right panels) by color. The impact on small-scale damping and polarization is much more significant under variations of  $\alpha_i$  than of  $m_{e,i}$ , as encoded in Eq. (2.28). Each curve holds all of  $R_\star$ ,  $x_{\text{eq}}$ ,  $\theta_s$ ,  $Y_{\text{He}}$ ,  $A_s a_\star^{1-n_s}$ , and  $\tau_{\text{reion}}$  fixed.

do not preserve the angular extent of the diffusion damping feature [79] as is possible with a varying electron mass; presumably the shape of the visibility function is also affected, with consequences described in Sections II A 3 and II A 4. Similarly, though Eq. (2.26) shows that  $\theta_s$  is preserved when increasing  $N_{\text{eff}}$  (i.e.,  $\omega_r/\omega_\gamma$ ) and  $h$  simultaneously, the diffusion damping rate [Eq. (2.16)] is

not [82–84]. Changes to the damping tail may be partially absorbed by the primordial tilt  $n_s$ , but not without involving the overall amplitude as well as the baryon abundance; varying the fraction of the radiation density that is collisionless has additional, well-studied physical effects on the CMB [40, 85–88]. Equation (2.28c) shows that the effect of a change to the total radiation density on the damping rate may be compensated not just by adjusting the helium yield  $Y_{\text{He}}$ , a commonly studied degeneracy, but also by altering the early-time values of the fine-structure constant or the hydrogen mass.

The scale factor of recombination would also be different if we instead suppose  $T_0$  differs from its measured value. Ref. [38] phrases the CMB’s dependence on  $\omega_b$ ,  $\omega_c$ , and  $T_0$  as being via the combinations  $\omega_b/T_0^3$  and  $\omega_c/T_0^3$ . Since  $T_0^3 \propto \omega_\gamma/T_0 = \omega_\gamma/a_\star T_\star$ , holding  $\omega_b/T_0^3$ ,  $\omega_c/T_0^3$ , and  $T_\star$  fixed also fixes  $R_\star$  and  $x_{\text{eq}}$ . Per Eq. (2.16), the diffusion damping parameter  $K_\star$  is invariant along this direction because both of  $\sqrt{\omega_\gamma}/a_\star^2 \propto T_\star^2$  and  $\omega_\gamma/\omega_r$  are unchanged. Since changing  $T_0$  does not affect physics during recombination (but rather the amount of expansion that has elapsed since then), the visibility function is also unchanged [as a function of  $\ln(a/a_\star)$ ]. Equation (2.26) shows that  $\theta_s$  is fixed if  $h \propto T_0^{-1.18}$ , matching the degeneracy direction identified in Ref. [38]. The effects of  $T_0$  and  $m_{e,i}$  are only distinguished by the latter’s effect on the total radiation density at recombination, explaining why  $h$  scales differently with  $T_0$  and  $m_{e,i}$  at fixed  $\theta_s$ .

The degeneracies discussed in this section are grounded in a scaling invariance of cosmological observables. Because the dynamics of perturbations in the early Universe is linear, the Boltzmann and Einstein equations governing their evolution depend only on the ratio of scales, i.e., are invariant under a common rescaling of the length scales appearing in the problem. Moreover, the initial conditions preferred by current data are, aside from being nearly scale invariant, also scale free: any rescaling of length scales may be absorbed into the over normalization of the primordial power spectrum. Because most cosmological observables are measured as features on the sky, i.e., as dimensionless ratios of length scales, they do not measure the value of any individual scale. The parameters of Eq. (2.28) enumerate the general requirements for a common rescaling of all length scales specifically relevant to early-Universe dynamics, which are met by varying the scale factor of recombination (via  $m_{e,i}$  or  $T_0$  per the above discussion).

A distinct class of models, in which the scale factor of recombination is unchanged, was explored in detail by Refs. [39–41] by taking  $\omega_i \propto \lambda^2$  for all species  $i$ ,  $\sigma_T n_e \propto \lambda$ , and  $A_s \propto \lambda^{1-n_s}$ . A simple realization thereof is to vary both  $T_0$  and  $m_{e,i}$  proportionately, in which scaling the density of all species  $\propto T_0^4$  preserves all of the parameter combinations in Eq. (2.28) without requiring changes to any other parameters. Given that direct measurements of  $T_0$  preclude this possibility, Refs. [39–41] invoke a “mirror” dark sector with the same particle content and parameters as the SM to allow for arbitrarily increasing the abundances  $\omega_i$ , meaning the abundance of the visible sector does not scale with  $\lambda$ . The proportional scaling of the total matter and radiation densities preserves  $x_{\text{eq}}$  as well as  $\theta_s$  (since  $h^2 \propto \sum_i \omega_i$ ), while the nonscaling of the visible photon and baryon densities preserves  $R_\star$ . Constancy of the damping parameter  $K_\star$ , however, requires an additional ingredient. [Note that in Eq. (2.15),  $\omega_\gamma$  and  $Y_{\text{He}}$  are those for the visible sector, while  $\omega_r$  is the radiation density of the entire Universe.] Refs. [39, 40] invoke a differing helium yield  $Y_{\text{He}}$  to achieve the requisite scaling of the Thomson scattering rate, while Ref. [41] instead takes  $m_{e,i} \propto \alpha_i^{-2} \propto \lambda^{-1/3}$  to simultaneously fix  $K_\star$  and  $a_\star$ .

The symmetry of the Einstein-Boltzmann equations is broken by nonequilibrium effects during recombination that alter the ionization history, but only mildly so. (The symmetry is also broken by nonzero neutrino masses, but since they are only bounded and not measured, one is free to rescale them as well.) However, each of the aforementioned possible realizations is constrained by direct measurements of either  $T_0$  or  $Y_{\text{He}}$ , including that varying  $m_{e,i} \propto \alpha_i^{-2} \propto \lambda^{-1/3}$  because the BBN prediction for the helium yield is not invariant under this transformation [32]. Moreover, the arguments of this section demonstrate that the full rescaling symmetry is more restrictive



than necessary to keep *early-time* dynamics invariant. Namely, distinct degeneracy directions are afforded by freeing the scale factor of recombination  $a_\star/a_0$ , whether by varying  $T_0$  or  $T_\star$ . But such scenarios do not achieve the full rescaling symmetry of the Einstein-Boltzmann system. They are distinguished by effects arising at late times, which we turn to now.

## B. Late-Universe signatures

The dynamics of the late Universe are driven by the dark sector and so do not depend explicitly on the fundamental constants. However, given the constraining power of the early universe observables discussed in the previous subsection,  $\Lambda$ CDM parameters—specifically the relative contributions of matter and dark energy to the total energy budget—change along the degeneracy direction as fundamental constants are varied. The discussion thus far has entirely neglected dark energy beyond its effect on the distance to last scattering and the sound horizon, Eq. (2.26). We now focus on the late-time effects of dark energy.

In models that are well described by flat  $\Lambda$ CDM cosmology at late times, the shape of the late-time expansion history is only characterized by the scale factor of matter–dark-energy equality,

$$a_{m-\Lambda} \equiv \sqrt[3]{\omega_m/\omega_\Lambda}. \quad (2.29)$$

Along the degeneracy direction that preserves the primary CMB spectra,  $\omega_m \propto \omega_r/a_\star$  but  $h \approx \sqrt{\omega_m + \omega_\Lambda} \propto \sqrt{\omega_r}/a_\star^{3/2}$ . The dark energy density thus increases much more steeply than the matter density along the degeneracy, drastically altering when matter–dark-energy equality occurs and the physical effects that depend upon it. Matter perturbations grow more slowly in a Universe dominated by dark energy than one dominated by matter; Section IIB 1 discusses the resulting impact on secondary signatures in the CMB and Section IIB 4 that on matter clustering. Datasets that measure distances at low redshift directly trace out the shape of the expansion history and provide independent constraints; these are discussed in Sections IIB 2 and IIB 3.

### 1. Late-time integrated Sachs-Wolfe effect and CMB lensing

While dark energy is entirely negligible near recombination when most of the CMB anisotropies are seeded, at late times its presence alters the dynamics of metric perturbations, sourcing a nonzero integrated Sachs-Wolfe effect and altering the degree to which the primary CMB anisotropies are gravitationally lensed. In a Universe dominated by cold dark matter, the metric potentials (in Newtonian gauge, for instance) are constant. As CMB photons traverse potential wells, the amount by which they blueshift upon entering is precisely compensated by the corresponding redshift as they exit. If large-scale metric potentials instead decay with time, which they do to an extent controlled by the relative abundance of dark energy [89, 90], this cancellation is incomplete, enhancing CMB power. The earlier the dark energy era begins (i.e., the smaller  $a_{m-\Lambda}$  is), the larger this effect. Because matter–dark-energy equality occurs rather near the present, this late ISW effect affects only the largest observable scales—at multipoles  $\ell \lesssim 30$  where cosmic variance strongly limits the CMB’s constraining power.

The CMB is also lensed by matter fluctuations at late times [91], which grow more after horizon crossing in Universes where matter–dark-energy equality occurred later. Whereas an increased absolute change in metric perturbations over time results in an enhanced ISW signal on large scales, the lensing deflection spectrum scales in proportion to the power in matter fluctuations. Both effects are depicted in Fig. 4. The disproportionate increase in the dark energy density required to decrease the distance to last scattering in proportion to the sound horizon [Eq. (2.26)] makes the

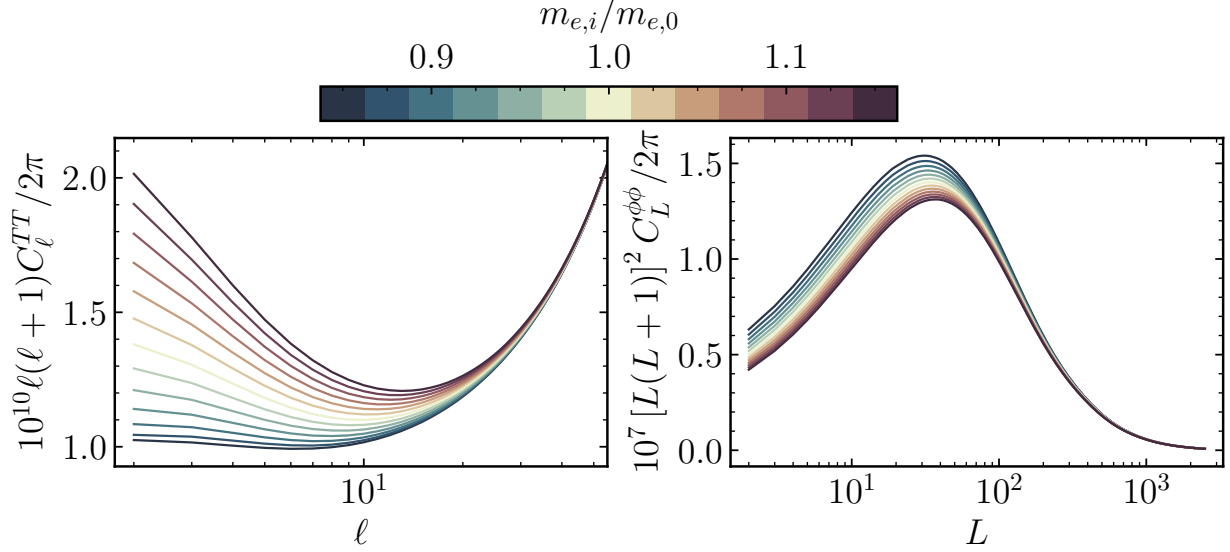


Figure 4. Large-scale CMB temperature (left) and lensing (right) power spectra in cosmologies varying the electron mass  $m_{e,i}$  by color, holding all of  $R_\star$ ,  $x_{\text{eq}}$ ,  $\theta_s$ ,  $Y_{\text{He}}$ ,  $A_s a_\star^{1-n_s}$ , and  $\tau_{\text{reion}}$  fixed. The changes in the power spectra arise due to the correlation of  $a_{m-\Lambda}$  with  $a_\star \propto 1/m_{e,i}$  rather than directly from processes that depend on the constants' values. Therefore, these results are broadly unchanged for commensurate variations in  $\alpha_i^2$  as for  $m_{e,i}$  and are effectively identical under variations in  $T_0$  that yield the same values of  $a_{m-\Lambda}$  when holding  $\theta_s$  and  $x_{\text{eq}}$  fixed.

dark energy era begin earlier, leading to the suppression of lensing power and enhancement of the late ISW effect evident in Fig. 4.

## 2. Baryon acoustic oscillations

Late-time changes to the universe's energy budget may also be constrained directly via distance measurements. First, baryon acoustic oscillations imprint an oscillatory pattern in the matter correlation function that may be treated as a standard ruler. The BAO scale specifically corresponds to a local maximum of the matter density correlation function, but it can be accurately modeled by simply evaluating the comoving sound horizon evaluated at the baryon drag epoch,  $r_d \equiv r_s(a_{\text{drag}})$  [92, 93]. Baryons decouple slightly after recombination,  $a_{\text{drag}} > a_\star$ , because the photon number density is so much greater than that of the baryons, so  $r_d$  is slightly larger than  $r_{s,\star}$ .

The angular BAO scales are extracted from various galaxy surveys and reported as

$$\theta_{\text{BAO}}(a) \equiv \frac{r_d}{D_V(a)} \quad (2.30a)$$

$$\theta_{\text{BAO},\parallel}(a) \equiv \frac{r_d}{cH(a)^{-1}} \quad (2.30b)$$

$$\theta_{\text{BAO},\perp}(a) \equiv \frac{r_d}{D_M(a)}. \quad (2.30c)$$

(We retain factors of  $c$  in this subsection to clearly specify units.) In Eq. (2.30a),

$$D_V(a) = \sqrt[3]{\frac{D_M(a)^2}{H(a)/c} (1/a - 1)} \quad (2.31)$$

is an effective, comoving-volume-averaged distance to a galaxy sample and the transverse distance  $D_M$  in Eq. (2.30c) is defined in Eq. (2.19). While these measurements rely on template modeling in a fiducial cosmology, Ref. [94] showed that any bias in application to modified cosmological models is negligible for existing datasets.

Substituting Eq. (2.21) for the comoving distance in Eq. (2.30c) shows that BAO distances depend on  $H_0$  only through an overall scaling in the combination  $r_d H_0$ :

$$\theta_{\text{BAO},\perp}(a) = \frac{r_d h}{c/H_{100}} \frac{[F_M(1; a_{m-\Lambda}) - F_M(a; a_{m-\Lambda})]^{-1}}{2\sqrt{1 + a_{m-\Lambda}^{-3}}}. \quad (2.32)$$

The dependence on the scale factor  $a$  is through a (nonlinear) function depending on cosmological parameters only via  $a_{m-\Lambda}$ . A sufficient number of BAO measurements, spanning a sufficient range of scale factors about  $a_{m-\Lambda}$ , could therefore constrain  $a_{m-\Lambda}$  independently of  $r_d$  and  $H_0$  individually. (The same conclusions apply for  $\theta_{\text{BAO}}$  and  $\theta_{\text{BAO},\parallel}$ .) Neglecting the small difference between  $r_d$  and  $r_{s,*} \propto a_*/\sqrt{\omega_r}$  [Eq. (2.24)], the overall scaling of Eq. (2.32) then requires that  $h \propto \sqrt{\omega_r}/a_*$ , which differs substantially from  $h \propto \sqrt{\omega_r}/a_*^{3.18}$  as required by the CMB [Eq. (2.26)]. For models that only vary the scale factor of recombination (whether via  $T_0$  or early-time variations in fundamental constants), BAO data therefore offer constraining power in the  $h$ - $a_*$  plane complementary to that of the CMB.

### 3. Low-redshift distances from supernovae

Type Ia supernovae (SNe Ia) occur at a characteristic mass that yields a standard luminosity suitable for inferring distances. The apparent magnitude of each SN Ia (labeled  $i$ ) is parameterized as [95–97]

$$m_i = 5 \log_{10} \left[ \frac{a_i}{a_{i,\text{hel}}} \frac{D_L(a_i)}{10 \text{ pc}} \right] + M_B, \quad (2.33)$$

where  $M_B$  is the fiducial magnitude of an SN Ia (a parameter that itself must be sampled over) and  $D_L$  the luminosity distance,  $D_L(a) = D_M(a)/a$ . The ratio of the CMB-frame ( $a_i$ ) and heliocentric ( $a_{i,\text{hel}}$ ) redshifts inside the logarithm corrects for peculiar velocities [98–100]; SNe distance datasets tabulate both these redshifts and either the apparent magnitude  $m_i$  or the distance modulus  $m_i - M_B$ . Absorbing the peculiar velocity correction into the apparent magnitude via the definition  $\hat{m}_i \equiv m_i - 5 \log_{10}(a_i/a_{i,\text{hel}})$ , we may rearrange Eq. (2.33) into the apparent brightness, which may be interpreted as a “luminosity angle” in analogy to the BAO angles Eq. (2.30):

$$\theta_L(a_i) \equiv \frac{10 \text{ pc} \cdot 10^{-M_B/5}}{D_L(a_i)} = 10^{-\hat{m}_i/5}. \quad (2.34)$$

The numerator of the middle expression acts as a standardized or calibrated luminosity distance.

Akin to BAO distances, without external constraints on the fiducial magnitude  $M_B$  (from, e.g., Cepheids [24–26] or the tip of the red giant branch [101–104]), SN Ia distances only probe the shape of the expansion history, not its absolute scale (i.e.,  $H_0$ ). The “luminosity angle” [Eq. (2.34)] factorizes in the same manner as Eq. (2.32):

$$\theta_L(a_i) = \frac{10^{\log_{10} h - M_B/5}}{c \text{ s/m}} \frac{a_i [F_M(1; a_{m-\Lambda}) - F_M(a_i; a_{m-\Lambda})]^{-1}}{2\sqrt{1 + a_{m-\Lambda}^{-3}}}. \quad (2.35)$$

The Hubble constant is only constrained via the combination  $\log_{10} h - M_B/5$ , and as for BAO a sufficient number of SN Ia distance measurements may constrain the relative amount of dark energy and matter independent of their overall calibration (and of  $H_0$ ).

#### 4. Matter clustering

The clustering of matter is sensitive to the late-Universe expansion history, in addition to nonstandard dynamics of dark matter and dark energy. The amplitude of structure is often quantified by the present-day, root-mean-squared overdensity in spheres of radius  $R$ ,  $\sigma(R)$ , defined by

$$\sigma(R)^2 = \int d \ln k W(k, R)^2 \frac{k^3}{2\pi^2} P_{\text{lin}}(k), \quad (2.36)$$

where  $P_{\text{lin}}$  is the linear matter power spectrum and

$$W(k, R) = \frac{3}{(kR)^3} [\sin(kR) - kR \cos(kR)] \quad (2.37)$$

is the Fourier transform of a top-hat function with radius  $R$ . A standard metric is  $\sigma_8 \equiv \sigma(8 h^{-1} \text{ Mpc})$ , which is most sensitive to scales that entered the horizon in the radiation era; constraints, however, are often quoted as combinations of  $\sigma_8$  and  $\Omega_m$  that are best constrained by particular probes; for example,  $S_8 \equiv \sqrt{\Omega_m/0.3} \sigma_8$  for cosmic shear [105–107].

The clustering of matter is sensitive to the expansion history via two effects. First, the onset of the dark energy era suppresses structure growth; the earlier matter–dark-energy equality ( $a_{m-\Lambda}$ ) occurs, the stronger the effect. Second, even at fixed  $a_{m-\Lambda}$  increasing the total matter density  $\omega_m$  pushes the comoving horizon at matter–radiation equality (which determines the turnover in the matter power spectrum from growing with  $\sim k$  to falling off as  $\sim k^{-3}$ ) to smaller scales  $k_{\text{eq}} \propto \omega_m$  [per Eq. (2.12)], regardless of  $a_*$ . When fixing  $a_{m-\Lambda}$  by taking  $\omega_\Lambda \propto \omega_m$ ,  $h$  scales with  $\sqrt{\omega_m}$  and  $k_{\text{eq}} \cdot 8h^{-1} \text{ Mpc} \propto \sqrt{\omega_m}$ . In other words, the earlier the matter era begins, the less suppressed the scales that contribute to Eq. (2.36) are by their subhorizon evolution during the radiation era, enhancing  $\sigma_8$ . As such, absent modifications to the dynamics of dark matter or the early-Universe expansion history,  $h$  and  $\sigma_8$  are generally positively correlated.

### III. COSMOLOGY WITH COUPLED, HYPERLIGHT SCALARS

In the previous section, we discuss expanded phenomenology of cosmologies with varying fundamental constants without considering a concrete model. A “bottom-up” approach promotes a fundamental constant to a dynamical scalar described by an action principle; the scalar’s value dictates that of the constants and it carries stress-energy [108–110]. Such scalars also arise in theories with extra dimensions as so-called dilaton or moduli fields [111–120]. To realize the scenarios discussed in Section II we consider one such simple model, that of a massive scalar whose amplitude modulates the strength of electromagnetism  $\alpha$  and the mass of the electron  $m_e$ . We take the field to be so light as to have a cosmologically frozen amplitude until some time after recombination, leading to the fundamental constants taking on time-independent values prior to recombination that differ from those measured today.

In Section III A, we review the gravitational impact of the scalar on the background (i.e., spatially homogeneous) cosmology. In particular, we identify a new degeneracy in cosmological parameters when one allows for an increase in the total energy density of matter after recombination relative to that which was present at earlier times. While such a “late dark matter” scenario is necessarily implemented by a hyperlight scalar field that modifies the value of fundamental constants at earlier times, it could also be realized via other mechanisms; massive neutrinos are an additional example. In Section III B we expose how the necessary impact of the scalar’s spatial perturbations on the growth of structure ultimately affects cosmological observables. Finally, in Section III C,

we connect the phenomenological parameters of the modified cosmology (energy densities and fundamental constants) with microphysical model parameters (the mass and amplitude of the field). In combination with Ref. [32], we find that varying-constant cosmologies can be implemented with microphysical parameters that are as yet unconstrained by other probes.

Studying the cosmological impact of a scalar field requires solving the covariant Klein-Gordon equation in the perturbed, expanding spacetime [Eq. (A2)]:

$$\nabla^\mu \nabla_\mu \phi = \frac{dV(\phi)}{d\phi}. \quad (3.1)$$

Numerical solutions for massive scalar fields [i.e., with potential  $V(\phi) = m_\phi^2 \phi^2$ ] provide a unique challenge by introducing a fixed timescale, i.e., the scalar’s oscillation period  $1/m_\phi$ . As we detail in full in Appendix A, we extend CLASS by implementing a scheme recently devised in Ref. [121] that solves the Klein-Gordon equation for some number of oscillations before switching to an effective fluid approximation scheme. The prescription in Ref. [121] for matching onto fluid variables and determining the fluid’s effective equation of state and sound speed provides systematically improved precision compared to prior approaches. As described in Appendix A, we extend Ref. [121]’s results, which were applied only to scalars that begin oscillating in radiation domination, to a generalized background expansion rate [122].

In addition, fundamental constant variations due to a scalar field inevitably acquire spatial dependence, at least to some degree. The resulting fifth-force effects on the dynamics of electron density perturbations may also be ignored because electron density perturbations themselves, again neglecting their suppressed contribution to the Einstein equations, only enter the Boltzmann equation for photons at second order in inhomogeneities [123, 124]. That is, anisotropies generated by Thomson scattering are already first order because scattering in a homogeneous plasma generates no anisotropy; inhomogeneities in the Thomson scattering rate (whether due to inhomogeneities in the electron number density or in the Thomson cross section itself) therefore enter at second order.

### A. Impact on the cosmological background

To solve for the classical evolution of the scalar perturbatively, we expand the scalar into a homogeneous component and a small perturbation as  $\phi(t, \mathbf{x}) = \bar{\phi}(t) + \delta\phi(t, \mathbf{x})$ ; the homogeneous component of the Klein-Gordon equation Eq. (3.1) is then

$$\ddot{\bar{\phi}} + 3H\dot{\bar{\phi}} + m_\phi^2 \bar{\phi} = 0. \quad (3.2)$$

The scalar contributes to the Friedmann equations an energy density  $\bar{\rho}_\phi = \dot{\bar{\phi}}^2/2 + m_\phi^2 \bar{\phi}^2/2$  and a pressure  $\bar{P}_\phi = \dot{\bar{\phi}}^2/2 - m_\phi^2 \bar{\phi}^2/2$ .

If the field is sufficiently light compared to the Hubble rate at recombination,  $H_\star \approx 3 \times 10^{-29}$  eV, the scalar’s effect on the fundamental constants is effectively time independent over the Universe’s entire history up to (and including) recombination. Note that when a scalar’s couplings to matter are large enough, its equation of motion can be significantly modified from Eq. (3.2). Here we implicitly assume that these contributions are negligible; we consider the possibility and its impact on scalar field phenomenology in Ref. [32]. Because the late-time probes discussed in Ref. [32] provide relatively strong constraints on fundamental-constant variations at late times and the present day, the scalar (if it shifts the early-time constants from their present-day values) cannot be too light—it must be rolling at some point so that its oscillation amplitude redshifts by a sufficient amount by the present day. Since in standard cosmology recombination occurs after matter-radiation

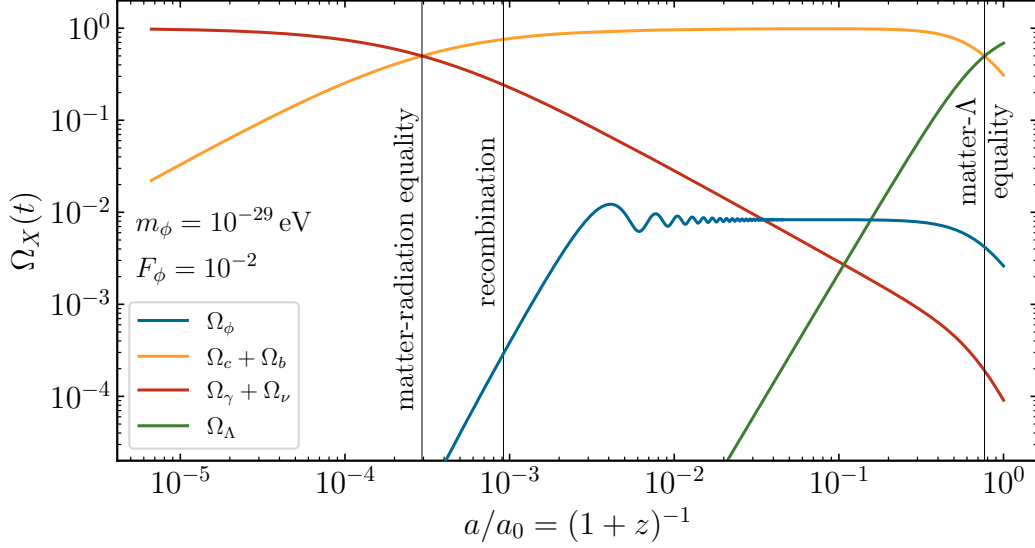


Figure 5. Relative abundances as a function of time,  $\Omega_X(t) = \bar{\rho}(t)/3H^2 M_{\text{pl}}^2$ , of matter (orange), radiation (red), dark energy (green), and a hyperlight scalar field (blue). Here the scalar has a mass  $m_\phi = 10^{-29}$  eV and an abundance  $F_\phi \equiv \bar{\rho}_{\phi,0}/\bar{\rho}_{c,0} = 10^{-2}$  relative to that of CDM.

equality and matter–dark-energy equality was relatively recent, the relevant parameter space for the scenarios we discuss requires the scalar to begin oscillating in the matter-dominated era.

More concretely, at early times ( $H \gg m_\phi$ ) the scalar is approximately frozen at its initial value  $\bar{\phi}_i$ , i.e., the appropriate initial condition for Eq. (3.2) is  $\bar{\phi} \rightarrow \bar{\phi}_i$  and  $\dot{\bar{\phi}} \rightarrow 0$  for  $m_\phi t \rightarrow 0$ . In a matter-dominated Universe with  $H = 2/3t$ , the solution to Eq. (3.2) with these initial conditions is  $\bar{\phi}(t) = \bar{\phi}_i \sin(m_\phi t)/m_\phi t$ . This solution motivates defining the time when oscillations begin by  $H(t_{\text{osc}}) = 2/3t_{\text{osc}} = 2m_\phi/3$ . We further define  $a_{\text{osc}}$  as the scale factor and  $z_{\text{osc}}$  as the redshift at that time. Well before  $t_{\text{osc}}$ , the scalar has negligible kinetic energy compared to that of its potential and therefore gravitates (at the background level) like dark energy. However,  $\bar{\rho}_\phi/\bar{\rho}_m \propto (a/a_{\text{osc}})^3$  in this period, so its contribution to the Einstein equations is entirely negligible until just before  $t_{\text{osc}}$ . Noting that  $a(t) \propto t^{2/3}$  in the matter era, after  $t_{\text{osc}}$  the scalar’s oscillation-averaged energy density and pressure are, to leading order in  $1/m_\phi t$ ,

$$\bar{\rho}_\phi \approx \frac{m_\phi^2 \bar{\phi}_i^2}{2(a/a_{\text{osc}})^3} \quad (3.3)$$

$$\bar{P}_\phi \approx 0, \quad (3.4)$$

just like nonrelativistic matter. (Appendix A 2 discusses the leading corrections to these results.) We define  $\omega_\phi = \bar{\rho}_\phi(t_0)/3H_{100}^2 M_{\text{pl}}^2$  as for the other density parameters.

The most important gravitational effect of the scalar on the background cosmology is therefore its delayed contribution to the matter density at late times, illustrated in Fig. 5. So long as the scalar begins rolling well before matter–dark-energy equality, any cosmological distance may effectively be computed in a pure  $\Lambda$ CDM cosmology that counts the scalar field’s energy density toward the total CDM density. Certainly any distance measurement at  $a \ll a_{\text{osc}}$  is well described in this approximation. The integral that defines the comoving distance, Eq. (2.20), has most of its support where  $1/aH$  is largest; in the matter- and dark-energy-dominated limits,  $1/aH \propto a^{1/2}$  and  $a^{-1}$ , respectively, placing the peak of the integrand at the epoch of equality. More concretely, the small- $a$  limit of Eq. (2.22),  $F_M(a, a_{m-\Lambda}) \propto a^{7/2}$ , quantifies the (un)importance of early time



deviations from a pure  $\Lambda$ CDM cosmology on the full comoving distance in Eq. (2.21). As such, the comoving distance to recombination may also be approximated by simply augmenting the CDM density to include the scalar's, ignoring its differing dynamics before  $a_{\text{osc}} \ll a_{m-\Lambda}$ . (The scale factor of equality  $a_{m-\Lambda}$  is also implicitly defined with reference to this combined, late-time matter density.)

Defining the late-to-early matter density ratio  $A_m$  and inserting  $\omega_{m,\text{late}} = A_m \omega_{m,\text{early}}$  for the matter density in the comoving distance to recombination [Eq. (2.25)], the parameter dependence of  $\theta_s$  in Eq. (2.26) extends to

$$\theta_s \propto \left( \frac{a_\star^{3.18} h A_m^{2.09}}{\sqrt{\omega_r}} x_{\text{eq}}^{-0.810} R_\star^{-0.499} \right)^{1/5.173}. \quad (3.5)$$

The additional freedom afforded by  $A_m$  enables preserving both  $a_\star^{3.18} h A_m^{2.09} / \sqrt{\omega_r}$  and

$$a_{m-\Lambda} = \left( \frac{A_m \omega_{m,\text{early}}}{\omega_\Lambda} \right)^{1/3} = \left( \frac{1}{h^2 / A_m \omega_{m,\text{early}} - 1} \right)^{1/3} \quad (3.6)$$

at any value of  $a_\star$ , i.e.,  $h$  and  $A_m$  provide two parameters to satisfy both conditions. (We take  $\omega_r$  to be fixed here, though our arguments generalize straightforwardly to scenarios that vary  $T_0$  rather than  $T_\star$ .) The latter condition is more algebraically tractable when phrased as requiring  $\Omega_m = A_m \omega_{m,\text{early}} / h^2 \propto A_m / a_\star x_{\text{eq}} h^2$  to be fixed. The resulting degeneracy direction has  $A_m \propto a_\star^{-1.034}$  and  $h \propto a_\star^{-1.017}$ .

This degeneracy direction *also* nearly exactly preserves  $h r_d$  as constrained by BAO distance measurements when  $a_{m-\Lambda}$  is also fixed [per Eq. (2.32)]. Measurements of the BAO scale at various redshifts—including that by the CMB at recombination—trace out the expansion history using a common ruler; distances probing either side of matter–dark-energy equality may only jointly agree at an arbitrary size of the sound horizon if  $a_{m-\Lambda}$  remains the same. In other words, the absolute scale (via  $h$ ) and shape (via  $a_{m-\Lambda}$ ) of the late-Universe expansion history are both free to change to satisfy that any individual BAO measurement (or  $\theta_s$ ), but fitting multiple simultaneously requires the shape ( $a_{m-\Lambda}$ ) to be unchanged. Furthermore, as argued in Section II B 3 SN Ia distance measurements (sans calibration) themselves are only sensitive to  $a_{m-\Lambda}$  (within flat the  $\Lambda$ CDM-like models considered here).

Prior literature studying electron mass variation as a solution to the Hubble tension [21–23] considered allowing for spatial curvature to address the inconsistency between the distance to recombination and late-Universe distances. The analysis here points to additional matter at late times as a more natural solution, even on an *ad hoc* basis, which in addition avoids confrontation with the expectation in inflationary cosmologies that spatial curvature is negligible. Whether models with scalar fields fulfilling these cosmologically motivated requirements are theoretically and phenomenologically tenable first requires mapping the parameterization of their cosmological effects ( $A_m$  and the early-time  $m_{e,i}$ ) to their fundamental parameters.

The background-level effect of the scalar field closely resembles that due to massive neutrinos. Namely, a single neutrino species with mass  $m_\nu$  and temperature  $T_\nu = \sqrt[3]{4/11} \sqrt[4]{N_{\text{eff}}/3} T_\gamma$  becomes exactly semirelativistic at a redshift

$$z_{T_\nu=m_\nu} + 1 = \frac{m_\nu}{T_\nu(a_0)} = 356.56 \frac{m_\nu}{0.06 \text{ eV}} \left( \frac{N_{\text{eff}}}{3.046} \right)^{-1/4} \quad (3.7)$$

and has a present-day density of

$$\omega_{\nu,\text{massive}} = \frac{3\zeta(3)}{2\pi^2} \frac{T_\nu^3}{3H_{100}^2 M_{\text{pl}}^2} = \frac{m_\nu}{93 \text{ eV}} \left( \frac{N_{\text{eff}}}{3.046} \right)^{3/4}. \quad (3.8)$$

Neutrino oscillation experiments require the sum of the neutrino masses to be greater than 0.06 eV [125–127], while *Planck* combined with BAO data places an upper limit of 0.12 eV (within  $\Lambda$ CDM) [75]; the heaviest neutrino species thus becomes nonrelativistic no earlier than  $z \sim 700$  but no later than  $z \sim 100$ . Massive neutrinos therefore contribute to the matter density only well after recombination (but still well before matter–dark-energy equality) with an abundance proportional to their mass, achieving the same effect encoded by  $A_m$  in Eqs. (3.5) and (3.6). The neutrino mass therefore plays the same role as  $\omega_\phi$  for the scalar field; if the sum of the neutrino masses is taken as a free parameter (rather than being fixed to a fiducial, minimal value as in most analyses) in addition to the early-time electron mass, we would expect the two to be positively correlated when considering CMB data in conjunction with low-redshift distance datasets. This correlation was indeed observed in Ref. [23]; its physical origin is explained by the arguments of this section.

However, the neutrinos’ masses determine both their abundance and the redshift at which they become matterlike (whereas the scalar’s abundance is set by both its mass and its initial misalignment), which means massive neutrinos can only contribute so much extra matter density without becoming nonrelativistic before recombination; concretely, Eqs. (3.7) and (3.8) combine into

$$\omega_{\nu,\text{massive}} = 6.45 \times 10^{-4} \frac{z_{T_\nu=m_\nu} + 1}{356.56} \frac{N_{\text{eff}}}{3.046}. \quad (3.9)$$

Thus, if all three neutrino flavors becomes semirelativistic at recombination, their present-day density is of order 5% of the CDM density. A massive scalar has the potential to make a greater contribution to the late-time matter density while still doing so only well after recombination.

In otherwise standard cosmological scenarios, the background-level effect of hyperlight scalars and massive neutrinos also reduces the Hubble constant inferred from CMB data: the increase in density in the matter era makes the Universe smaller without changing the sound horizon, requiring a compensatory reduction in the dark energy density to maintain the distance to last scattering. Equation (3.5) shows that  $h \propto A_m^{-2.09}$  at fixed  $a_\star$  (and  $x_{\text{eq}}$  and  $R_\star$ ). Per Eq. (3.9), a massive neutrino species with fiducial mass  $m_\nu = 0.06$  eV increases the total matter density by  $\approx 0.5\%$  relative to that from baryons and CDM ( $\omega_c + \omega_b \approx 0.14$ ), explaining why the CMB prefers values of  $h$  about a percent lower in cosmologies with versus without massive neutrinos. An anticorrelation between  $\omega_\phi$  and  $h$  is likewise evident in the results of Ref. [128] for ultralight axions with mass below  $\sim 10^{-29}$  eV.

If the scalar’s potential is steeper than quadratic about its minimum, the scalar’s energy density redshifts faster than that of matter once it begins oscillating. In this case, its gravitational effects would be important only in the brief interval near the beginning of its oscillations. While such effects are substantial in, e.g., early dark energy scenarios where a scalar starts oscillating around matter–radiation equality [129–133], the impact of a massless scalar that does so after recombination should be much less important.

## B. Impact on cosmological perturbations

A hyperlight scalar’s effect on the expansion history may be well understood as an enhancement of the late-time CDM density, as described in the previous subsection; the dynamics of its perturbations, however, are qualitatively distinct from CDM. A scalar’s mass  $m_\phi$  associates a Jeans scale to its perturbations, which is parametrically  $k_J \sim a\sqrt{Hm_\phi}$  at any given time; fluctuations on larger scales cluster like CDM, but on smaller scales they oscillate [121, 134–136]. Perturbations in CDM then grow more slowly on scales where not all of the matter content clusters, again in close analogy to massive neutrinos [137, 138] (which effectively behave as warm dark matter and have

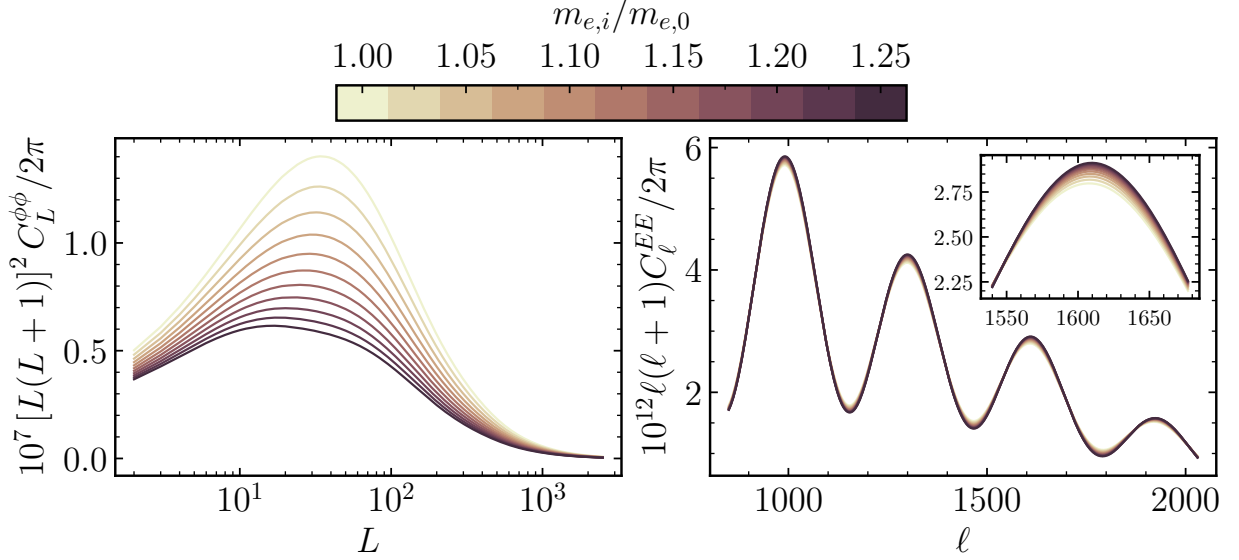


Figure 6. CMB lensing (left) and  $E$ -mode (right) power spectra in cosmologies varying the early-time electron mass  $m_{e,i}$  with a scalar field, by color. Each curve holds all of  $R_*$ ,  $x_{\text{eq}}$ ,  $\theta_s$ ,  $Y_{\text{He}}$ ,  $A_s a_*^{1-n_s}$ , and  $\tau_{\text{reion}}$  fixed. The scalar field has mass  $m_\phi = 10^{-30}$  eV and a density chosen to (approximately) fix the scale factor of matter–dark-energy equality via the degeneracy derived from Eq. (3.6). The plot inset in the right panel displays the  $E$ -mode power spectrum zoomed in to highlight the decreased smearing of one of the acoustic peaks.

a free-streaming scale associated to their temperature). On scales where a fraction  $f$  of matter does not cluster, the growth rate of CDM density fluctuations  $\delta_c \propto a^p$  is reduced from  $p = 1$  to  $p \approx 1 - 3f/5$  [135]. Appendix A 1 provides more detailed exposition on the dynamics of scalar fields, their perturbations, and their contribution to the Einstein equations.

In the mass range of interest,  $m_\phi \lesssim 10^{-28}$  eV, the Jeans scale is cosmologically macroscopic: writing  $H \sim m_\phi/(a/a_{\text{osc}})^{3/2}$  for scalars that begin oscillating in the matter era, the Jeans scale evolves as  $k_J \sim a_{\text{osc}} m_\phi \sqrt[4]{a/a_{\text{osc}}}$ . Before oscillations begin, the scalar’s energy density is small relative to the total density (evident in Fig. 5), so it has a negligible impact on the dynamics of CDM and baryons. Because of the weak scaling with  $a$ , a hyperlight scalar suppresses the growth of structure roughly on scales smaller than the horizon when oscillations begin,  $k_{\text{osc}} \equiv a_{\text{osc}} m_\phi \sim (120 \text{ Mpc})^{-1} \sqrt[3]{m_\phi/10^{-28} \text{ eV}}$ , at all times after it begins oscillating. The modifications to the growth of structure affect the CMB via the ISW effect and gravitational lensing; the latter is constrained both by direct reconstruction of the CMB lensing potential and by smearing of the acoustic peaks.

Figure 6 depicts the impact of a hyperlight scalar field on CMB lensing. The results follow the degeneracy identified in Section III A with varying  $m_{e,i}$ , setting the scalar field energy density to fix  $a_{m-\Lambda}$  as discussed below Eq. (3.6). The specific parameter dependence is made concrete in Section III C; the scalar’s present energy density relative to that of CDM is approximately  $\omega_\phi/\omega_c \approx 1.2(m_{e,i}/m_{e,0} - 1)$  [see Eq. (3.17) below]. The lensing spectrum is greatly suppressed by the presence of the scalar on all scales, but especially the smaller scales which, at late times, lens the primary CMB anisotropies, smearing the acoustic peaks. The latter effect is subtle but most evident in the  $E$ -mode power spectra displayed in Fig. 6, where the cases with the largest early-time electron mass  $m_{e,i}$  (and therefore the largest contribution from the scalar field) reach the point where the peaks are essentially unaltered by structure at late times. These findings are similar to

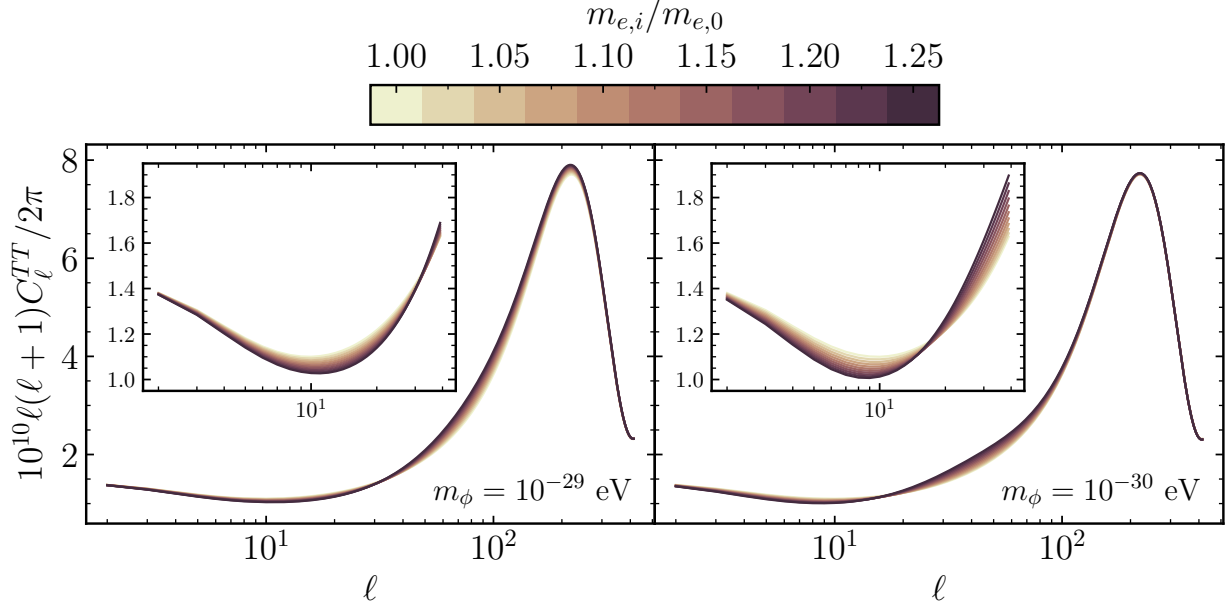


Figure 7. Large-scale CMB temperature power spectrum in cosmologies varying the electron mass  $m_{e,i}$  with a scalar field, by color. Each curve holds all of  $R_*$ ,  $x_{\text{eq}}$ ,  $\theta_s$ ,  $Y_{\text{He}}$ ,  $A_s a_*^{1-n_s}$ , and  $\tau_{\text{reion}}$  fixed and additionally includes a scalar field with mass  $m_\phi = 10^{-29}$  eV (left) or  $10^{-30}$  eV (right) with a density chosen to (approximately) fix the scale factor of matter–dark-energy equality via the degeneracy derived from Eq. (3.6). The inset panels zoom in on  $\ell < 40$ .

those in Ref. [139], which studied the purely gravitational effects of ultralight axions.<sup>2</sup> Observe also that the suppression of the lensing potential is far more drastic (at fixed  $m_{e,i}/m_{e,0}$ ) along the degeneracy direction with a hyperlight scalar than for that without one (Fig. 4).

As discussed in Section IIB 1, in Universes dominated by cold matter the ISW contribution to CMB anisotropies vanishes, a feature contingent on density fluctuations growing exactly as  $\delta\rho/\bar\rho \propto a$ . The ISW effect sourced by a hyperlight scalar is depicted in Fig. 7 for two different masses. With  $m_\phi = 10^{-29}$  eV, the scalar begins oscillating at  $z_{\text{osc}} \approx 390$ , which is near the earliest it can while remaining effectively frozen during recombination (i.e., such that any shift in fundamental constants is constant during recombination). However, this is still early enough to noticeably enhance the temperature power spectrum at the first acoustic peak (at  $\ell \sim 200$ ). With a lighter scalar, e.g., with  $m_\phi = 10^{-30}$  eV (and  $z_{\text{osc}} \approx 86$ ), the ISW effect is irrelevant at  $\ell > 100$  but is slightly more pronounced at smaller multipoles. Indeed, in both cases the ISW effect has nontrivial scale dependence, even suppressing power on large scales rather than enhancing it (as in smaller scales). The same features are again evident in cosmologies with ultralight axions [128]. The scalar’s full behavior—its homogeneous oscillations and dark-energy-like behavior beforehand, and the growth of fluctuations on large scales—has effects beyond the suppression of structure below the Jeans scale discussed here. The dynamics of the scalar’s perturbations therefore provide a possible means to constrain its mass through gravitational effects alone; see Refs. [128, 139–142] for more detailed exploration.

Scalars in the mass range we consider also suppress structure on scales that contribute to  $\sigma_8$ , defined in Section IIB 4. At present, the CMB-derived value of  $\sigma_8$  (within  $\Lambda$ CDM) is mildly discrepant with that inferred from large-scale structure probes [143]. While the discrepancy is not

<sup>2</sup> Note that the gravitational effects of pseudoscalars/axions and scalars are identical, up to the choice of the potential. Constraints on axions like those in Refs. [128, 139–142] therefore apply equally well to scalars without additional couplings.

nearly so severe as that of  $H_0$  between *Planck* and the SH0ES-calibrated distance ladder, it is worth noting that hyperlight scalars could in principle reconcile it, since those with masses  $m_\phi \lesssim 10^{-24}$  eV do not cluster on the scales to which  $\sigma_8$  is sensitive. Ref. [139] explored this possibility in detail, including constraints from galaxy clustering. However, since  $h$  is negatively correlated with  $\omega_\phi$  at fixed  $a_\star$  (as explained in Section III A),  $h$  and  $\sigma_8$  are positively correlated when increasing  $\omega_\phi$ . The exacerbation of the discrepancy between  $\sigma_8$  inferred from large-scale structure and CMB datasets in cosmologies that raise the CMB’s preference for  $H_0$  is cited as a common feature of  $\Lambda$ CDM extensions. On the other hand, a hyperlight scalar that also modifies the fundamental constants and triggers early recombination has the potential to simultaneously reduce the CMB’s preference of  $\sigma_8$  and raise that of  $H_0$ . Similar conclusions were drawn for the “axi-Higgs” model in Ref. [29], in which an ultralight axion shifts the electron mass by shifting the Higgs VEV at early times. Ignoring the effect of the Higgs VEV on the proton mass (which is not a valid approximation, as argued in Ref. [32]), the phenomenologies of the “axi-Higgs” scenario and of a hyperlight scalar coupled directly to the electron are effectively identical.

Finally, ultra- and hyperlight components of dark matter can suppress structure on nonlinear scales in a manner that may not be well captured by standard methods to estimate nonlinear corrections to the matter power spectrum [144, 145]. Scalars in the mass range we consider, however, do not cluster on observationally relevant scales or redshifts [140, 146, 147]. Moreover, nonlinear structure growth substantially impacts the CMB lensing potential only on scales smaller than those *Planck* measures [91]. Since we consider no other CMB lensing observations, we therefore follow Refs. [128, 139–142] in neglecting any nonlinear effects in the matter power spectrum.

### C. Parameter space

The mass of a scalar that begins oscillating in the matter-dominated era is related to the matter density as

$$m_\phi^2 = \frac{9H(t_{\text{osc}})^2}{4} \approx \frac{3}{4} \frac{\bar{\rho}_c(t_0) + \bar{\rho}_b(t_0)}{a_{\text{osc}}^3 M_{\text{pl}}^2}, \quad (3.10)$$

neglecting the scalar’s own contribution to the total energy density at that time. Using Eq. (3.3), the scalar’s energy density relative to that of CDM (at  $t > t_{\text{osc}}$ ) is therefore

$$F_\phi \equiv \frac{\bar{\rho}_\phi}{\bar{\rho}_c} = \frac{m_\phi^2 \bar{\phi}_i^2 / 2(a/a_{\text{osc}}^3)}{\bar{\rho}_c(t_0)/a^3} = \frac{3(1 + \omega_b/\omega_c)}{4} \bar{\varphi}_i^2, \quad (3.11)$$

where  $\bar{\varphi}_i$  is the initial homogeneous component of the rescaled field

$$\varphi \equiv \frac{\phi}{\sqrt{2}M_{\text{pl}}}. \quad (3.12)$$

Observe that this expression is independent of the mass  $m_\phi$  and holds for masses between (3/2 times) the Hubble rate at matter-radiation equality,  $3H_{\text{eq}}/2 \approx 3.4 \times 10^{-28}$  eV and that at matter–dark-energy equality,  $3H_{m-\Lambda}/2 \approx 2.6 \times 10^{-33}$  eV. The matter-era solution is then

$$\bar{\phi}(t) \equiv \sqrt{2}M_{\text{pl}}\mathcal{A}(t) \sin m_\phi t, \quad (3.13)$$

where the time-dependent, squared oscillation envelope for at  $t > t_{\text{osc}}$  is

$$\mathcal{A}(t)^2 = \frac{4}{3} \frac{F_\phi}{1 + \omega_b/\omega_c} \left( \frac{a(t)}{a_{\text{osc}}} \right)^{-3}. \quad (3.14)$$

In Ref. [32], the shift in a fundamental parameter  $\lambda$  (i.e.,  $\alpha$  or  $m_e$ ) is parameterized in terms of the scalar field by

$$\lambda(\varphi) \approx \lambda(0) [1 + g_\lambda(\varphi)], \quad (3.15)$$

where  $\lambda(0)$  is the vacuum value of the parameter, i.e., when the scalar is at the minimum of its potential. (For consistency with prior literature, we replace the subscript  $\alpha$ 's with  $e$ 's for the photon couplings,  $g_e \equiv g_\alpha$ .) A shift in the inverse scale factor of recombination, with fundamental-constant dependence given by Eq. (2.5), may therefore be written in terms of the scalar's couplings to the SM as

$$\frac{\Delta a_\star^{-1}}{a_\star^{-1}} \approx \frac{m_{e,i} - m_{e,0}}{m_{e,0}} + 2 \frac{\alpha_i - \alpha_0}{\alpha_0} = g_{m_e}(\bar{\varphi}_i) + 2g_e(\bar{\varphi}_i). \quad (3.16)$$

One may translate the  $\alpha_i$  dependence of any other quantity in Eq. (2.28) (e.g., those parameterizing the effects on small-scale damping and CMB polarization in Sections II A 3 and II A 4) analogously. For a scalar field that is frozen during recombination, these relationships, combined with Eq. (3.11), fully specify the correspondence between the phenomenological parameters ( $F_\phi$  and the early-time values of  $m_e$  and  $\alpha$ ) to the fundamental parameters of the model (those parameterizing  $g_{m_e}$  and  $g_e$  in addition to the initial condition  $\bar{\varphi}_i$ ).

To phrase the degeneracy direction identified in Section III A in terms of  $F_\phi$ , write  $\omega_{m,\text{late}} = (1 + F_\phi)\omega_c + \omega_b$ , such that  $A_m = 1 + F_\phi/(1 + \omega_b/\omega_c)$ . When  $A_m \propto a_\star^{-1.034}$ , which ensures that matter–dark-energy equality occurs at the same scale factor regardless of  $a_\star$  (along the identified degeneracy),

$$\frac{F_\phi}{1 + \omega_b/\omega_c} \approx 1.034 \frac{\Delta a_\star^{-1}}{a_\star^{-1}} \quad (3.17)$$

for small shifts  $\Delta a_\star^{-1}$ . The scalar must therefore make a relative contribution to the matter density at late times that is commensurate with the shift in recombination. This condition is approximately independent of the scalar's mass, so long as it begins oscillating after recombination (and therefore after the matter era begins) but sufficiently long before matter–dark-energy equality. More precisely, lighter scalars begin contributing to the matter abundance later and affect the distance to last scattering over a shorter interval. Scenarios with lighter scalars therefore require a slightly larger increase in response to an increase in  $a_\star^{-1}$  than given by the coefficient 1.034 in Eq. (3.17) (but still order unity), which is derived in Section III A under the assumption that the scalar contributes to the matter density at all times after recombination.

Per Eq. (3.11), to realize the condition of Eq. (3.17) the scalar thus must have a near-Planckian initial condition. Combining with Eq. (3.16),

$$\bar{\varphi}_i^2 = \frac{\bar{\phi}_i^2}{2M_{\text{pl}}^2} \approx \frac{4}{3} \cdot 1.034 [g_{m_e}(\bar{\varphi}_i) + 2g_e(\bar{\varphi}_i)]. \quad (3.18)$$

Ref. [32] motivates models in which the leading contributions to  $g_\lambda$  are quadratic:  $g_\lambda(\varphi) \approx d_\lambda^{(2)} \varphi^2/2$ . Because the scalar's energy contribution is *also* quadratic in the field's value, the degeneracy direction Eq. (3.18) lies at a fixed value of the dimensionless coupling coefficient. In this case, the early-time variation in fundamental constants [ $\lambda_i \equiv \lambda(\bar{\varphi}_i)$ ] may be written as

$$\frac{\lambda_i}{\lambda(0)} - 1 = g_\lambda(\bar{\varphi}_i) = d_\lambda^{(2)} \bar{\varphi}_i^2/2 = \frac{2d_\lambda^{(2)} F_\phi}{3(1 + \omega_b/\omega_c)}. \quad (3.19)$$



For instance, when  $g_e(\bar{\varphi}_i)$  is negligible, we expect the quadratic coupling  $d_{m_e}^{(2)} \approx 1.45$  to quantify the degeneracy direction in cosmological data. Interestingly, we show in Ref. [32] that such  $\mathcal{O}(1)$  quadratic scalar couplings to electrons and photons are allowed by all other experimental probes.

The cosmological data we consider depend only on the early-time values of  $m_e$  and  $\alpha$ , i.e., on  $g_{m_e}(\bar{\varphi}_i)$  and  $g_e(\bar{\varphi}_i)$  regardless of their functional form (again, when the field remains frozen until after recombination). The scalar’s cosmological abundance is conveniently parameterized like other species via  $F_\phi$ , since  $\omega_\phi \equiv F_\phi \omega_c$ . The simplest parameterization of the model for parameter inference using cosmological data is therefore simply that of the early-time constants,  $m_{e,i}$  and  $\alpha_i$ , and  $F_\phi$ . However, physically motivated priors may only be (directly) phrased in terms of the fundamental parameters. In particular, while  $F_\phi$  depends only on  $\bar{\varphi}_i^2$ , variations in  $m_{e,i}$  and  $\alpha_i$  are given by the product of (some power of) the field amplitude  $\bar{\varphi}_i$  and dimensionless coupling coefficients. Any fixed shift in a fundamental constant may be accommodated by arbitrarily small  $\bar{\varphi}_i$  with a large enough coupling. Within this class of models and taking quadratic couplings as an example, the limit of a gravitationally negligible scalar,  $\bar{\varphi}_i^2 \ll 1$  and  $d_\lambda^{(2)} \gg 1$ —the limit of strong coupling, in other words—corresponds to that of prior work that considered variations in fundamental constants only at a phenomenological level.

Aside from neglecting the potential cosmological importance of the late dark matter contribution of a hyperlight scalar motivated in Section III A, the strong-coupling limit runs afoul of the considerations of microphysical models in Ref. [32]. The effective scalar potential sourced by matter becomes substantial and can affect the scalar’s dynamics at early times, even before recombination. Shifts in fundamental constants that are time-independent through the end of recombination, as studied by prior work on a phenomenological basis, thus require that the responsible scalar contributes to gravity to some extent. We exclude regimes in which the constants evolve before recombination from our analysis here but discuss the possibility in more detail in Ref. [32].

The opposite, weakly coupled limit is specified by  $\bar{\varphi}_i \gtrsim 1$ . One might exclude this regime on the grounds that the scalar then traverses a super-Planckian field distance [148], but such a regime is surely entirely excluded observationally, given that a scalar with  $m_\phi \gtrsim H_0$  would have come to dominate the energy density of the Universe before the start of coherent oscillations and cause a period of inflation when  $\bar{\varphi}_i \gtrsim 1$ . One might then wonder whether some or all of the Universe’s present-day dark energy can in fact made up of the scalar (e.g.  $m_\phi \lesssim H_0$ ). By its very nature, a species that behaves like dark energy or a slowly varying cosmological “constant” (e.g., a quintessence field) must have a nearly flat bare potential (which is true of the  $m_\phi^2 \phi^2$  potential when  $m_\phi \ll H_0$ ). Such a requirement would preclude any significant variation of the field between the present-day and earlier times. However, the effective potential sourced by the cosmological bath of SM matter and radiation (or even dark matter [149, 150]) can easily dominate the bare potential at early times. We therefore cannot outright exclude the possibility of significant variations in fundamental constants at early times from a field that is today dark-energy-like without considering concrete models of its interactions and their constraints from other probes. We restrict our analysis to scalars as subcomponents of the present-day dark matter for simplicity.

#### IV. COSMOLOGICAL PARAMETER INFERENCE

We now test the models and hypothesized parameter degeneracies discussed in Sections II and III using cosmological data. Insofar as the degeneracy directions identified in Sections II and III (which are calculated about the best-fit  $\Lambda$ CDM cosmology) hold throughout parameter space, we expect  $\Lambda$ CDM extended with a hyperlight scalar coupled to the electron to satisfy CMB, BAO, and SN Ia data at any  $m_e$  with  $h \propto m_e$  and  $F_\phi \equiv \omega_\phi/\omega_c \approx m_{e,i}/m_{e,0} - 1$ . Moreover, beyond simply reproducing the best-fit  $\Lambda$ CDM prediction, the additional freedom afforded by the electron-coupled scalar can

in principle enable precise changes in predictions that better fit the data but are inaccessible within the  $\Lambda$ CDM parameter space. The scalar’s matter contribution could also enhance the consistency of these datasets when  $\alpha$  is varied, but the impact on small-scale damping and CMB polarization presumably remains as the strongest limitation on the scenario. Quantitatively testing these questions requires an analysis of those data using full numerical solutions to the Einstein-Boltzmann equations (and the Klein-Gordon equation).

We first establish baseline expectations for phenomenological varying-constants scenarios (i.e., without a scalar field) in Section IV A, analyzing in detail the individual and joint constraining power of CMB and low-redshift distance measurements. Then Section IV B studies the impact of consistently including a coupled scalar field as microphysical realization of time-varying fundamental constants. Before proceeding, we describe the methods and datasets we employ in our analysis.

In parameter inference, we sample over the standard set of  $\Lambda$ CDM parameters with broad, uninformative priors: the present baryon and CDM densities,  $\omega_b \sim \mathcal{U}(0.005, 0.035)$  and  $\omega_c \sim \mathcal{U}(0.01, 0.25)$ ; the Hubble rate  $h \sim \mathcal{U}(0.25, 1.1)$ ; the tilt and amplitude of the scalar power spectrum,  $n_s \sim \mathcal{U}(1.61, 3.91)$  and  $A_s$  [the latter via the combination as  $\ln(10^{10} A_s) \sim \mathcal{U}(1.61, 3.91)$ ]; and the redshift of reionization  $z_{\text{reion}} \sim \mathcal{U}(4, 12)$ . Here we use  $\mathcal{U}(a, b)$  to denote a uniform prior between  $a$  and  $b$ . In some circumstances it proves more computationally efficient to sample over the angular scale of the sound horizon  $\theta_s \sim \mathcal{U}(0.9, 1.1)$  in place of  $h$ ; we comment on the impact of this choice where it is used. We exclude the possibility of a negative dark energy density (which is otherwise accessible in allowed parameter space in some situations). We sample over  $m_{e,i}/m_{e,0}$  and  $\alpha_i/\alpha_0 \sim \mathcal{U}(0.7, 1.3)$  whenever considering variations of each parameter. We fix a single massive neutrino with the standard, minimal mass  $m_\nu = 0.06$  eV; representing the other two by a relativistic fluid with an effective number of degrees of freedom of 2.0308 yields a total early-time  $N_{\text{eff}}$  [Eq. (2.1)] of 3.044. Appendix B 2 details our methods for sampling via Markov Chain Monte Carlo (MCMC).

In the following, we consider a variety of datasets of the types described in Section II and discuss their implementations in more detail in Appendix B 1. We use the 2018 *Planck* likelihoods via the `Plik_lite` variants that are marginalized over the parameters of the foreground models [75, 151]. These likelihoods require an additional parameter  $y_{\text{cal}}$  characterizing the overall map calibration, sampled with the standard Gaussian prior with mean 1 and standard deviation 0.0025 [151]. We use BAO measurements from a common combination of surveys: the Six-degree Field Galaxy Survey (6dFGS) [152] (with an effective sample redshift  $z = 0.106$ ), the SDSS Main Galaxy Sample (MGS) DR7 [153] ( $z = 0.15$ ), the Baryon Oscillation Spectroscopic Survey (BOSS) DR12 galaxies ( $z = 0.38$  and  $0.51$ ), and the Extended Baryon Oscillation Spectroscopic Survey (eBOSS) DR16 luminous red galaxies (LRG) [154, 155] ( $z = 0.70$ ). Note that the constraining power of this combination is dominated by eBOSS measurements, at least for the models we consider; we refer to this commonly used combination as the SDSS+ BAO dataset. We separately use recent BAO measurements from Dark Energy Spectroscopic Instrument (DESI) DR1 [156–158], using data from all tracers; we note that these results are yet unpublished at the time of writing. Finally, we use supernova distance measurements from the Pantheon [95], Pantheon+ [96, 97], DES 5YR [159], and Union3 [160] results; we sample over the overall normalization via the degenerate combination  $\log_{10} h - M_B/5 \sim \mathcal{U}(3.7, 3.73)$  that is well constrained independently of external measurements of the fiducial magnitude  $M_B$  (or of  $h$ , for that matter). That is, we do not include calibration from, e.g., Cepheids [24–26] or the tip of the red giant branch [101–104].

## A. Varying constants

### 1. Planck data alone

We first seek to test whether the parameter degeneracies argued for in Section II bear out in a complete analysis of CMB data. Figure 8 displays the posterior distribution for  $\Lambda$ CDM with a varying early-time electron mass, evaluated with *Planck* 2018 CMB and lensing likelihoods. The results indeed display a strong degeneracy, which the red curves show correspond closely to the direction  $\omega_b \propto m_{e,i}$ ,  $\omega_c \propto m_{e,i}$ , and  $h \propto m_{e,i}^{3.18}$ . The posterior is cut off at low values of these parameters almost exclusively by requiring  $h^2 \geq \omega_b + \omega_c$  (i.e., requiring a nonnegative dark energy density). The posteriors are therefore asymmetric, falling off at values of  $m_{e,i}/m_{e,0} \gtrsim 0.92$ . Namely, arbitrarily large values of the electron mass are *not* as favored as those with  $m_{e,i}/m_{e,0} < 1$ . As a consequence, 97.5% of the posterior lies where  $h < 0.72$ —not the resounding solution to the Hubble tension the results of, e.g., Fig. 3 might promise. Moreover, the median of the marginalized posterior over the Hubble constant is  $h = 0.47$ , and that of the early-time electron mass is  $m_{e,i}/m_{e,0} = 0.90$ .

We identify several effects that disfavor larger  $m_{e,i}$  (and therefore larger  $h$ ). As argued in Section II, the degeneracy in the varying electron mass model is effectively perfect so far as early-time effects are concerned, but the CMB is sensitive to the late Universe via the ISW effect and lensing (Section II B 1). In Fig. 9 we display the low- $\ell$  temperature power spectrum and the lensing power spectrum evaluated over a representative sample of the posterior. The early-time electron mass correlates strongly to the ISW enhancement of the temperature power spectrum at low multipoles because  $h$  is strongly constrained to increase with  $m_{e,i}$  in order to correctly locate the acoustic peaks. As explained in Section II B 1,  $h$  must decrease so rapidly with decreasing  $m_{e,i}$  that matter–dark-energy equality is pushed to much later times (even to the future,  $a_{m-\Lambda} > 1$ ). As illustrated as well by Fig. 4, matter overdensities therefore decay less, enhancing the lensing spectrum relative to  $\Lambda$ CDM and reducing the ISW enhancement of large-scale temperature power. The data in the left panel of Fig. 9 suggest that the ISW effect by itself prefers late recombination to dark energy, given that most of their central values skew low, even compared to curves at the lower boundary of the posterior (which corresponds to negligible dark energy density). Indeed, a lack of power on large angular scales is a persistent and unexplained feature of CMB observations [161–166].

In addition, lensing data also appear to favor the enhanced peak evident in Fig. 9, but it is challenging to compare the relative constraining power of the first few data points that skew high to those at higher multipoles that skew low (and have smaller error bars). More likely, the enhanced lensing power is favored by the “lensing anomaly” of *Planck* data [75, 167–169] in which the acoustic peaks exhibit greater lensing-induced smoothing than predicted in  $\Lambda$ CDM. Such a conclusion was drawn in Ref. [38], which studied CMB power spectrum constraints on its present-day temperature  $T_0$ ; as argued in Section II A 6, varying  $T_0$  and  $m_{e,i}$  should exhibit nearly identical phenomenology.

Finally, the shape of a chosen prior is not necessarily negligible over posteriors so broad as those in Fig. 8. For the results in Fig. 8 (and any results using CMB data alone), we sample over  $\theta_s$  instead of  $h$  (using numerical optimization to solve for  $h$  in this case), as is conventional in MCMC analyses of CMB data. In scenarios with varying electron mass, uniformly sampling over  $h$  and  $m_{e,i}$  covers a broad range of values for  $\theta_s$ , most of which lie far from the narrow range of  $\theta_s$  values allowed by *Planck*. The angular size of the sound horizon  $\theta_s$ , suitably calculated, provides a measure of a broadly model-independent feature in the data that is well constrained (the angular locations of the acoustic peaks) and whose posterior allows for more efficient MCMC sampling (in terms of effective sample size per MCMC sample). But  $\theta_s$  and  $h$  are nonlinearly related, meaning a uniform prior for one results in a nonuniform prior for the other. Equation (2.26) (which is evaluated near the  $\Lambda$ CDM best-fit parameters) allows us to estimate that the effective prior on  $h$  from sampling uniformly in  $\theta_s$  is  $\partial\theta_s/\partial h \sim h^{-0.81}$ , a trend that is roughly reproduced by direct samples from our

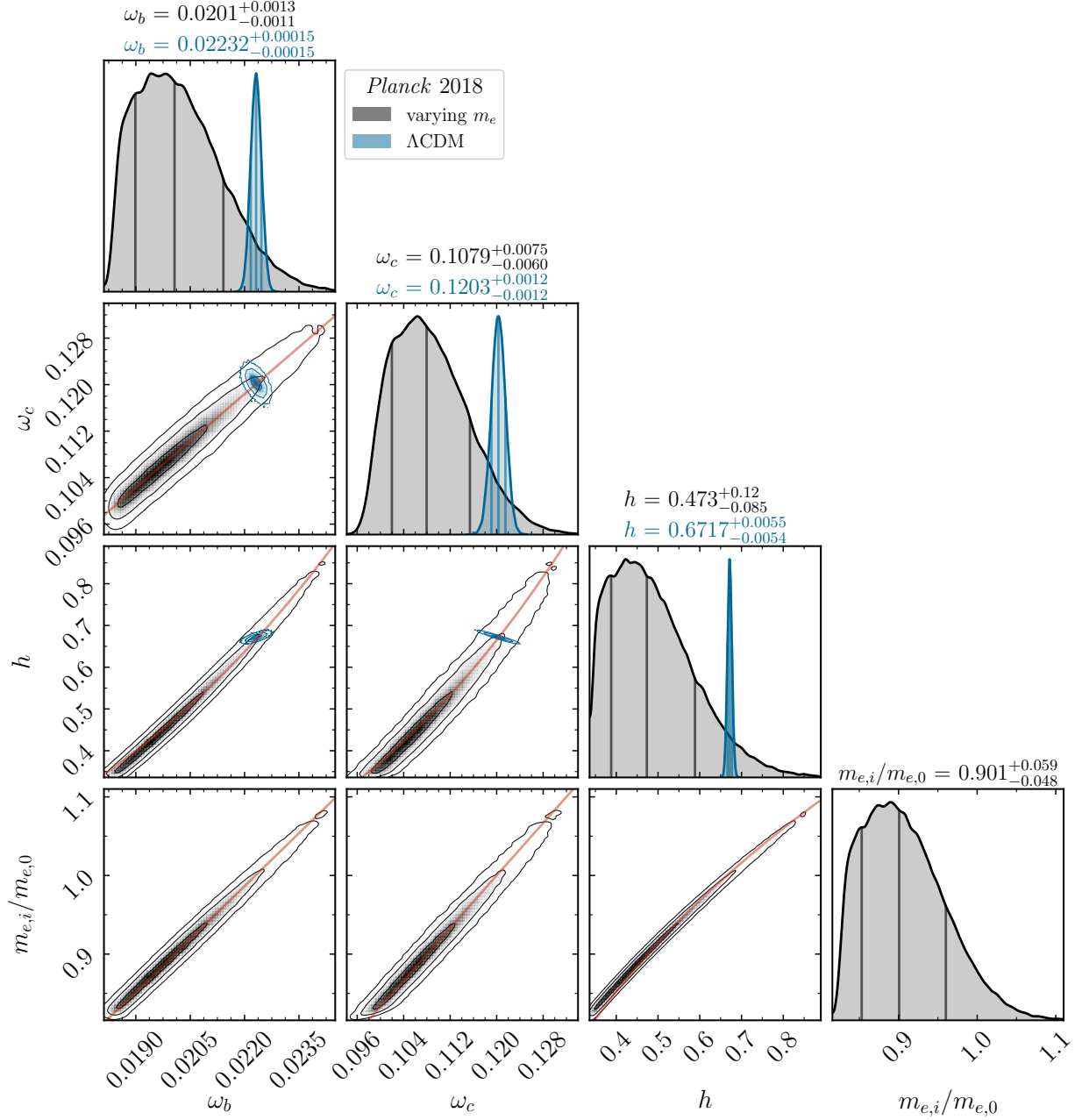


Figure 8. Posterior distribution over a subset of the parameters of the varying electron mass model without a scalar field (grey) which exhibits extended degeneracies compared to standard  $\Lambda$ CDM (blue), using the likelihood for the full set of *Planck* 2018 data including lensing (see Appendix B1). The panels along the diagonal depict kernel density estimates of marginalized, one-dimensional posteriors in each parameter, with vertical lines marking the median and 16th and 84th percentiles. These one-dimensional posteriors are normalized relative to their peak value to facilitate comparison. The median and corresponding  $\pm 1\sigma$  uncertainties for each parameter are reported above the diagonal panels. The lower panels display the marginalized, two-dimensional joint posterior density for pairs of parameters as a histogram and the 1, 2, and 3 $\sigma$  contours thereof (i.e., the 39.3%, 86.5%, and 98.9% mass levels). Contours are slightly smoothed to mitigate noise due to the binning of such narrow distributions, but not to an extent that artificially broadens their extent. Red lines in each panel depict the expected degeneracy direction derived in Section II A 5 which is largely born out in the data:  $\omega_b$  and  $\omega_c \propto m_{e,i}$  and  $h \propto m_{e,i}^{3.18}$ .

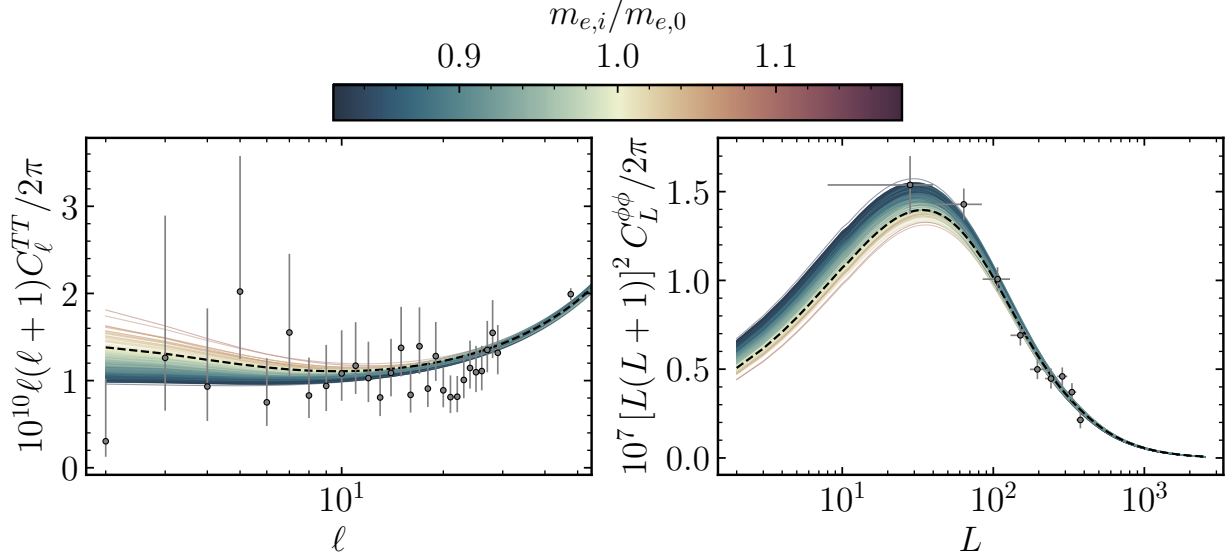


Figure 9. Large-scale CMB temperature (left) and lensing (right) power spectra for 1000 cosmologies sampled from the posterior in Fig. 8, i.e., that for the varying electron mass model (without a scalar field) subject to *Planck* 2018 data. Each curve is colored according to its value of  $m_{e,i}/m_e$  as indicated by the color bar. The binned *Planck* 2018 spectra and standard errors are superimposed in grey, and the result for the  $\Lambda$ CDM best-fit cosmology is depicted in dashed black. These results may be compared with those in Fig. 4 (though the vertical scales are not identical).

prior. This scaling does not explain all (nor even most) of the trend displayed in Fig. 8, however. Such a penalty on larger  $h$  is entirely negligible for  $\Lambda$ CDM with contemporary datasets, where  $h$  is constrained at the 1% level or better, but it is of at least marginal consequence for attempts to address the Hubble tension with models that achieve broader posteriors on  $h$  (like that in Fig. 8).<sup>3</sup>

Turning to variations in the fine-structure constant, Fig. 10 presents parameter constraints from *Planck* 2018 data alone in analogy to Fig. 8. Due to the strong dependence of small-scale damping (Section II A 3) and of the amplitude of the polarization spectrum (Section II A 4) on  $\alpha_i$ , illustrated in Fig. 3, no extended degeneracy of  $\Lambda$ CDM parameters with  $\alpha_i$  appears. Because  $h$  is even more sensitive to  $\alpha_i$  than to  $m_{e,i}$  at fixed  $\theta_s$  [Eq. (2.26)], the posterior distribution over  $h$  broadens slightly compared to  $\Lambda$ CDM, with a standard deviation roughly twice as large. In contrast to  $m_{e,i}$ , the fine-structure constant is also correlated with the tilt of the scalar power spectrum  $n_s$  [defined in Eq. (2.27)]. Though diffusion and Landau damping effectively have exponential dependence on scale, *Planck*’s observations cover only a limited range of scales where they are relevant, enabling a partial degeneracy with the power-law tilt of the initial power spectrum. Because the pivot scale  $k_p$  that parameterizes the primordial power spectrum [Eq. (2.27)] is larger than the inverse sound horizon at recombination, a bluer spectrum (larger  $n_s$ ) reduces the amplitude of the first peak and requires a larger amplitude  $A_s$  to compensate. The degeneracy between  $A_s$  and  $\alpha_i$  is evident in our results, but weaker than that between  $n_s$  and  $\alpha_i$  and also does not affect the marginalized posterior over  $A_s$ . Finally, we note that neither the lensing nor low- $\ell$  anomalies discussed around Fig. 9 for varying  $m_{e,i}$  are relevant in the parameter space available when varying  $\alpha_i$ .

Figure 11 displays residuals of the CMB power spectrum relative to the  $\Lambda$ CDM best fit, evaluated for a representative sample of the posterior for the varying- $m_e$  and varying- $\alpha$  scenarios using only

<sup>3</sup> As both  $h$  and  $\theta_s$  are derived parameters, a uniform prior in one is not necessarily any more motivated than in the other; one could equally well choose the dark energy density  $\omega_\Lambda$ . A more theoretically grounded prior (and choice of parameterization) would require a concrete model of dark energy.

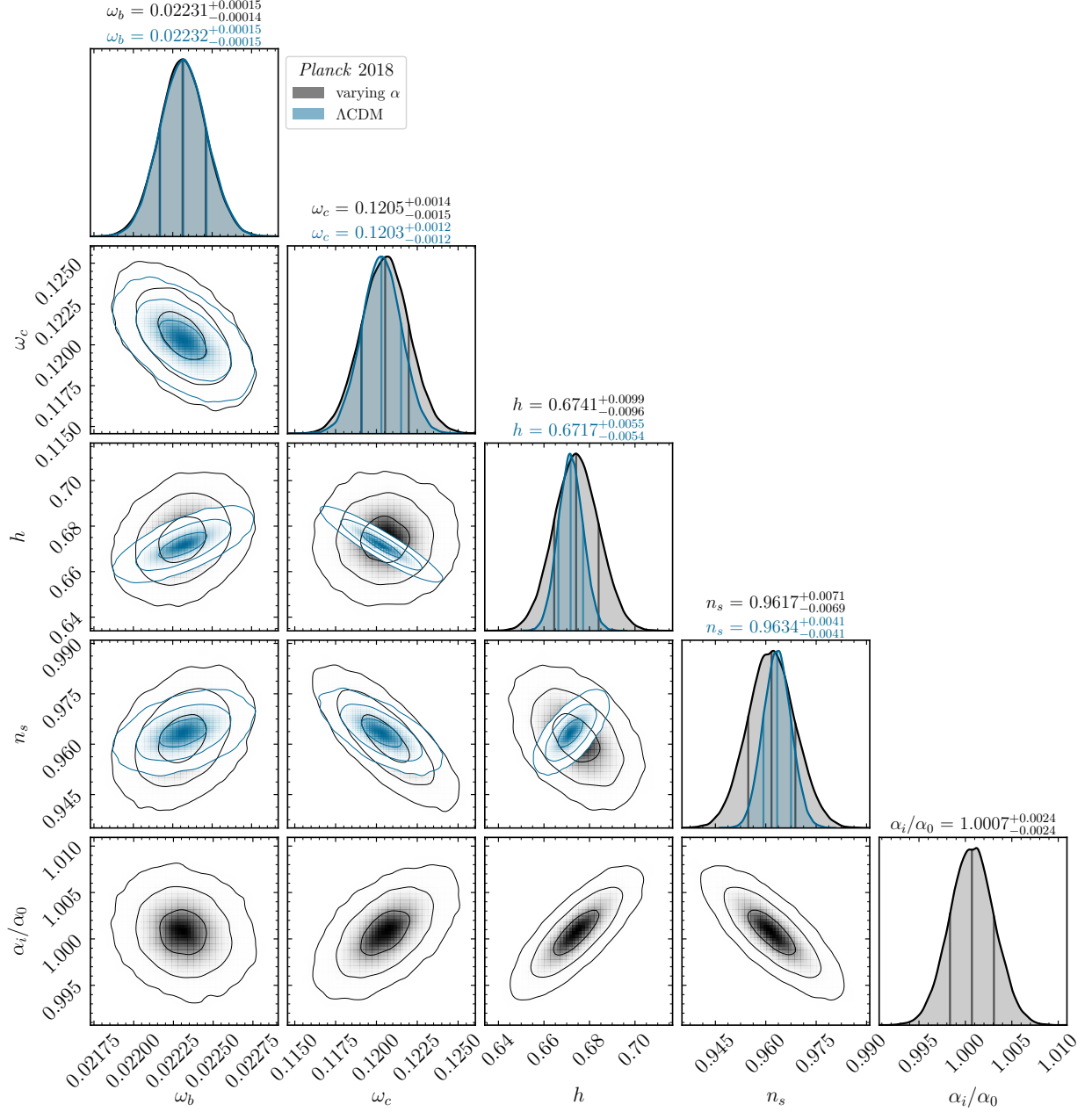


Figure 10. Posterior distribution over a subset of the parameters of the varying fine-structure constant model (without a scalar field), using the likelihood for the full set of *Planck* 2018 data including lensing (see Appendix B 1). Results are depicted as described in the caption of Fig. 8, additionally plotting the scalar spectral tilt  $n_s$  due to its correlation with  $\alpha_i/\alpha_0$ .

the *Planck* 2018 likelihoods. Beyond the differences exhibited at low  $\ell$  in Fig. 9, the residuals in the varying- $m_e$  scenario exhibit no clear trend with  $m_{e,i}$ , nor any easily identifiable systematic effect. Aside from noticeable oscillations in the  $TE$  cross correlation residuals, the lack of particularly distinguishable features is consistent with the expectation from Section II that no important physical effects correlate uniquely with the electron mass (within the full extended  $\Lambda$ CDM parameter space).

The residuals for the varying- $\alpha$  scenario display several features in line with the expectations from the effect of the fine structure constant on the damping tail and polarization discussed in



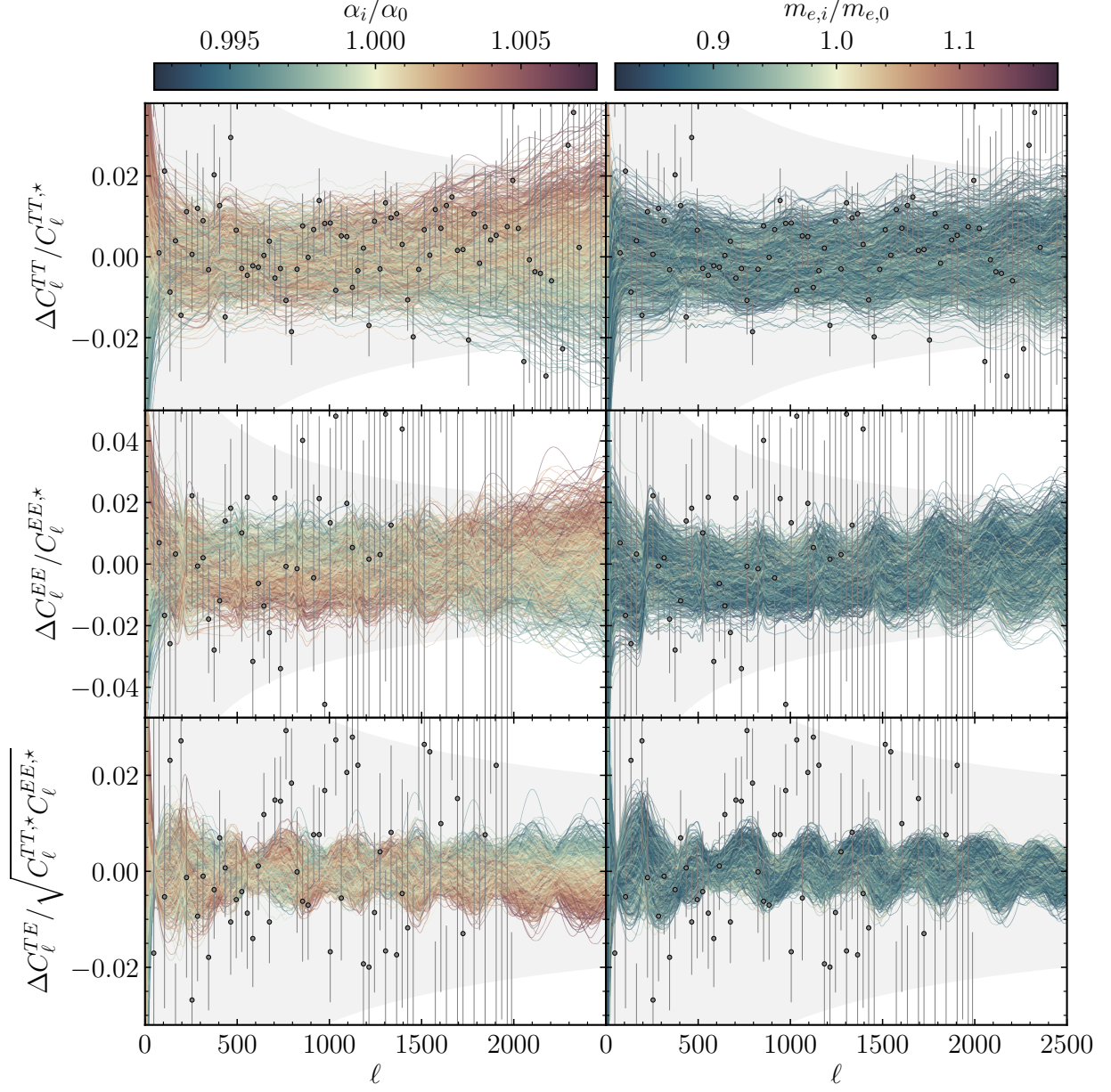


Figure 11. Residuals of the CMB power spectrum relative to the best-fit  $\Lambda$ CDM result,  $\Delta C_\ell^{XY} = C_\ell^{XY} - C_\ell^{XY,*}$ , evaluated for 1000 cosmologies sampled from the posterior of the varying- $\alpha$  (left panels) and  $-m_e$  (right panels) models with the *Planck* 2018 likelihoods alone. In order to illustrate the correlation between parameters and features in the residuals, each curve is colored by its value of the fundamental constant that is varied as indicated by the respective color bar. The top and middle panels depict relative difference of the temperature and  $E$ -mode auto power spectra, respectively, while the bottom panels depict the residual of the  $TE$  cross correlation normalized by  $\sqrt{C_\ell^{TT,*}C_\ell^{EE,*}}$ . The binned *Planck* 2018 spectra and standard errors are superimposed in grey, and the shaded grey regions show the extent of cosmic variance for each multipole  $\ell$  (i.e., relative errors of  $\sqrt{2/(2\ell+1)}$ ). (*Planck*'s error bars can be smaller because they are binned over a range of multipoles.) Note that the color scales are symmetric about one even when the posterior is not (as is the case for  $m_{e,i}/m_{e,0}$  in the right panels).



Section II and Fig. 3. The correlation of damping with  $\alpha_i$  is particularly evident at high multipoles, with larger (red) and smaller (blue)  $\alpha_i/\alpha_0$  displaying increased and decreased small-scale power, respectively. In addition, the enhancement of moderate-scale ( $\ell \sim 500 - 1200$ ) polarization power for *smaller*  $\alpha_i/\alpha_0$  (in contrast to the trend at larger  $\ell$ ) due to the broadened visibility function is also evident in Fig. 11, as anticipated in Fig. 3. More recent CMB polarization observations, like the Atacama Cosmology Telescope [170] and the South Pole Telescope [171, 172] would likely marginally improve upon *Planck*'s ability to constrain  $\alpha_i$  via the effect with cosmic-variance-limited measurements at  $\ell \gtrsim 1000$ . However, the ultimate constraining power of features on moderate scales is limited by cosmic variance; current and future high-resolution CMB experiments clearly have great potential to improve upon the fine-structure constant constraints of *Planck*. In particular, Fig. 3 suggests that high-resolution observations can break the degeneracy of  $\alpha_i$  and  $n_s$  evident in Fig. 10. While the residuals in the varying- $m_e$  scenario also exceed cosmic variance on scales beyond *Planck*'s resolution, they do not appear to correlate with  $m_{e,i}$  to any noticeable degree; this suggests that high-resolution CMB observations may not substantially improve bounds on electron mass variation.

## 2. Impact of low-redshift distance measurements

We now consider the impact of constraints on the late-Universe expansion history on the findings of the previous section. In particular, the CMB itself provides very weak constraints on the early-time electron mass that are mostly driven by *Planck*'s mild (and possibly anomalous) preference for late recombination in a Universe with a much lower dark energy abundance than in  $\Lambda$ CDM. However, Section II B 2 shows that the BAO scale at late times exhibits a distinct degeneracy between  $h$  and  $a_\star$  (at fixed  $a_{m-\Lambda}$ ). To provide effective constraints using BAO data alone, we impose an additional prior on  $R_\star$  and  $x_{\text{eq}}$  derived from the posteriors in Fig. 8. In particular, a bivariate normal distribution with means (0.620, 0.321), autocovariances  $(1.7, 0.66) \times 10^{-5}$ , and cross-covariance  $4.1 \times 10^{-6}$  effectively reproduces posteriors for  $R_\star$  and  $x_{\text{eq}}$  using *Planck* 2018 data for *both*  $\Lambda$ CDM and varying- $m_e$  cosmologies (as Section II argued should be the case). This prior effectively includes the information from the shape of the CMB as measured by *Planck* that drives constraints on  $\omega_b$  and  $\omega_c$  marginalized over the angle subtended by the sound horizon,  $\theta_s$ . Without this information, BAO data alone would be unable to pick out a unique degeneracy between  $h$  and  $a_\star$ .

Figure 12 compares the posteriors for  $h$  and  $m_{e,i}$  or  $\alpha_i$  when using *Planck* 2018 data and the SDSS+ BAO dataset (including the above-described prior) separately and jointly. Without any additional mechanism, varying constant scenarios may only simultaneously fit both *Planck* and BAO data where their individual posteriors have overlapping support. Their combined constraints lie modestly far from the peak of either posterior (and in fact is localized at larger values of  $h$  and  $m_{e,i}$  than either individual posterior). The  $2\sigma$  mass levels for both cases in fact hardly overlap, further highlighting that *Planck* data prefer quite a different late-time Universe via the shape of the CMB than preferred by BAO measurements or by measurements of the distance to last scattering in  $\Lambda$ CDM. Nevertheless, the posterior is localized in the  $h$ - $m_{e,i}$  plane about  $m_{e,i} \approx m_{e,0}$  and  $h$  near its  $\Lambda$ CDM region. Under variations in the fine-structure constant, a broad degeneracy with  $h$  is allowed by BAO data, since it and the prior on  $R_\star$  and  $x_{\text{eq}}$  are only sensitive to  $\alpha_i$  via its effect on  $a_\star$ . Comparing these results with those including *Planck* data highlights how precisely CMB observations can measure the early-time fine structure constant. The datasets combined constrain the early-time electron mass to deviate at only the percent level and the fine-structure constant at the 0.2% level from their values measured today.

For neither varying  $\alpha_i$  nor  $m_{e,i}$  do the posteriors in Fig. 12 using only BAO data lie precisely

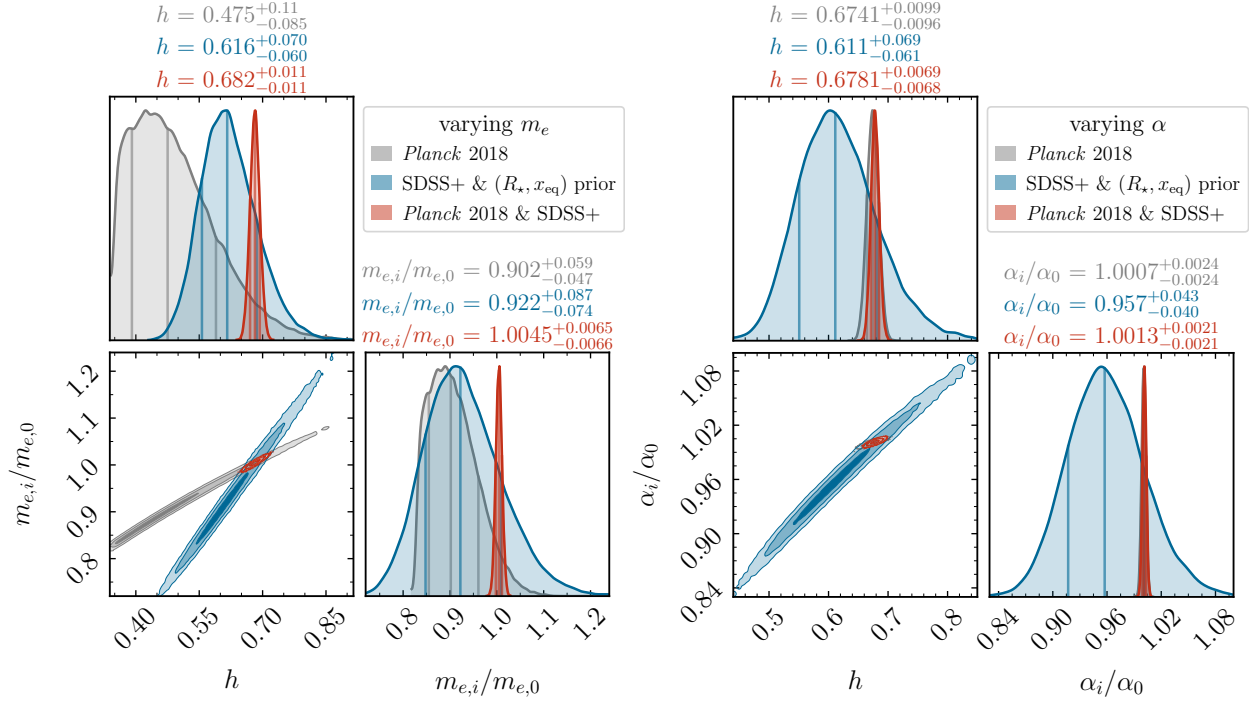


Figure 12. Posterior distribution over  $h$  and  $m_{e,i}/m_{e,0}$  (left) or  $\alpha_i/\alpha_0$  (right) in cosmologies with varying constants without a scalar field. The same quantities are depicted in Figs. 8 and 10, comparing results using the *Planck* 2018 likelihoods (grey); the BAO dataset from eBOSS, SDSS, and 6dFGS described in the text (blue); and both simultaneously (red). The diagonal panels display kernel density estimates of the one-dimensional, marginalized posterior relative to their peak value, and the lower panels depict 1, 2, and 3 $\sigma$  mass levels of the two-dimensional joint posterior, again slightly smoothed to facilitate comparison.

along  $h \propto 1/a_*$ , as would be expected from Section II B 2 if  $a_{m-\Lambda}$  were well constrained. The BAO measurements we employ in reality only cover a relatively narrow range of redshifts and are insufficient in number and precision to fully measure  $a_{m-\Lambda}$  independently of the overall normalization in Eq. (2.32), i.e., they remain slightly correlated. While eBOSS provides additional BAO measurements from tracers beyond LRGs like quasars, emission line galaxies, and Lyman- $\alpha$  absorption [173], cosmological constraints from these are known to be mildly inconsistent [174–177]. However, DESI DR1’s results from various spanning redshifts  $\sim 0.3$  to 2.33 may be more justifiably combined [156]. We compare to results with *Planck* combined instead with DESI data in Fig. 13; the posterior shifts over the  $h - a_{m-\Lambda}$  degeneracy to larger values of  $h$  and smaller  $a_{m-\Lambda}$ . This shift is driven not just by DESI’s preference for an early onset of dark-energy domination (evident in its  $\Lambda$ CDM results as well [156]) but also for a slightly larger uncalibrated amplitude  $hr_d$ . However, we note that the posterior of  $hr_d$  shifts to lower values by several percent when excluding DESI DR1’s LRG results in redshift bins  $z = 0.51$  and  $0.71$ ; these data appear to be mild outliers with a fair amount of leverage when interpreted within  $\Lambda$ CDM cosmology [156], so we caution against interpreting this result too seriously.

Type Ia supernova datasets can also measure the scale factor of matter–dark-energy equality  $a_{m-\Lambda}$ , and they do so independently of the sound horizon and with distance measurements out to slightly higher redshifts than LRG-derived BAO measurements. Since the degeneracy direction that preserves  $\theta_s$  does not hold  $a_{m-\Lambda}$  fixed (i.e., has  $a_{m-\Lambda}$  strongly correlated with  $m_{e,i}$ ), these datasets should yield different preferences for  $m_{e,i}$  (and therefore  $h$ ) if they prefer different  $a_{m-\Lambda}$ . Figure 13 shows that this is the case, to an extent: the medians of the marginalized posteriors for  $h$  vary by 3 – 8% percent when *Planck* data is combined with one of the SDSS+ BAO dataset, DESI’s DR1

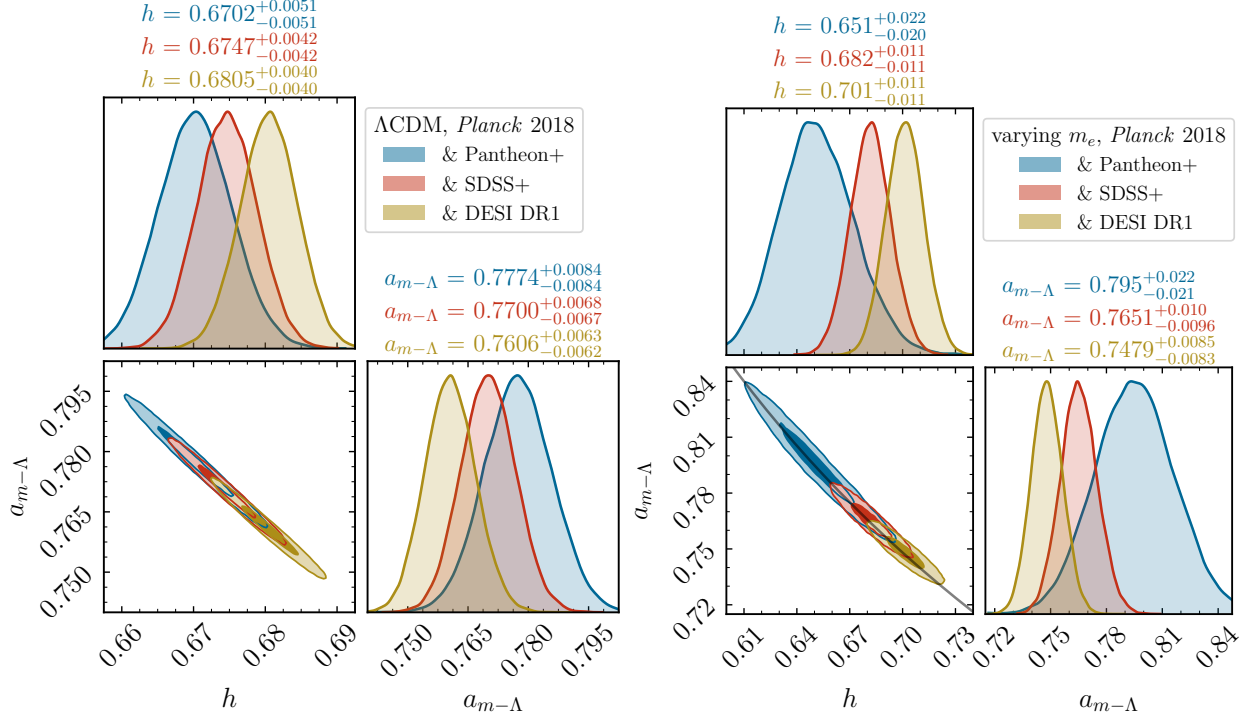


Figure 13. Posterior distribution over  $h$  and  $a_{m-\Lambda}$  (a derived parameter) in  $\Lambda$ CDM (left) and varying- $m_e$  scenarios (right), comparing results that use the *Planck* 2018 likelihoods combined with one of the Pantheon+ (blue), SDSS+ BAO (red), and DESI DR1 BAO (gold) datasets. The diagonal panels display kernel density estimates of the one-dimensional, marginalized posterior relative to their peak value, and the lower panels depict 1 and  $2\sigma$  mass levels of the two-dimensional joint posterior. Note that the left panels span a much broader range in  $h$  and  $a_{m-\Lambda}$  than do the right ones. The grey line in the lower left panel depicts the expected degeneracy inferred from Eq. (2.26), i.e., with  $\omega_m \propto m_{e,i}$  and  $h \propto m_{e,i}^{3.18}$ .

BAO measurements, or the Pantheon+ dataset. Because  $h$  varies rather sensitively with  $m_{e,i}$  along the posteriors, the corresponding variation in inferred values for  $m_{e,i}$  is less than 2.5%. Further, the posteriors in the  $h - a_{m-\Lambda}$  plane show a strong correlation as expected, affirming that constraints from the SN datasets (which include no external calibration on the fiducial brightness magnitude  $M_B$ ) derive from their measurement of the shape of the expansion history.

The  $\Lambda$ CDM posteriors in Fig. 13 are more mutually consistent across dataset combinations in spite of being much narrower than those that vary the electron mass, since in  $\Lambda$ CDM  $h$  is constrained to simultaneously satisfy *Planck*'s precise measurement of  $\theta_s$ . The varying- $m_e$  model, not so restricted, allows the posteriors on  $a_{m-\Lambda}$  to be mostly driven by late-time datasets. Indeed, the constraints on  $a_{m-\Lambda}$  in the left panels of Fig. 13 nearly match those each individually infers for the flat  $\Lambda$ CDM model [96, 156, 173]. Similar conclusions apply to the fine-structure constant, since it also affects the scale factor of recombination, but to a lesser degree given that the CMB constrains  $\alpha_i$  independently of its effect on  $a_\star$ .

## B. Coupled, hyperlight scalars

We now study the effect of consistently accounting for a hyperlight scalar hypothesized to couple to the electron or photon, realizing the fundamental-constant variations in Section IV A. We numerically implement the scalar field's dynamics as described in Section III (with further details in Appendix A). In addition to the parameters specified in Section IV, we sample over the scalar's

present energy density relative to that of CDM, i.e.,  $F_\phi = \omega_\phi/\omega_c \sim \mathcal{U}(0.0, 0.3)$ . Directly sampling over the scalar’s mass  $m_\phi$  is challenging because observables are only weakly sensitive to its value (within the mass range we consider); again following Refs. [128, 139–142], we therefore fix  $m_\phi$  to a single value in parameter inference. We take a fiducial mass  $m_\phi = 10^{-30}$  eV, commenting on other choices in Section IV B 2. Because we only consider scalars that begin oscillating in the matter era,  $F_\phi$  uniquely determines the scalar’s initial misalignment  $\bar{\phi}_i$  via Eq. (3.11). We take purely adiabatic initial conditions, assuming any isocurvature perturbations in  $\phi$  generated during inflation are negligible.

### 1. Planck data alone

The arguments of Section III that cosmological data should favor a hyperlight scalar with energy contribution proportional to the increase in the electron mass hinge upon the assumption that  $\Lambda$ CDM provides an effectively optimal fit to features determined by late-time dynamics. In particular, Section III shows that when *increasing*  $h$  to compensate for a smaller sound horizon at larger  $m_e$ , the scalar’s contribution to the matter density can restore the relative amount of dark energy and matter (i.e., the scale factor at which they are equal,  $a_{m-\Lambda}$ ). Though *Planck* data by itself does not favor the parameter space in which this effect is relevant, a hyperlight scalar still opens up additional freedom in the late-time expansion history that could allow for larger  $m_{e,i}$  without altering  $\theta_s$ . Constraining the model with *Planck* 2018 likelihoods alone therefore tests the extent to which they can tolerate hyperlight subcomponents of dark matter (or whether any features in the data are actually better explained by hyperlight scalar fields).

Figure 14 shows that *Planck* 2018 data only allows a hyperlight scalar to marginally affect the results without a scalar (Section IV A 1). The posteriors over  $h$  and  $m_{e,i}$  peak at slightly smaller values, but the degeneracy between  $h$  and  $m_{e,i}$  is largely unmodified by including a scalar field. The posterior over  $F_\phi$  in this case is also marginally broader than that without any SM couplings, but only at lower  $h$ . At these smallest values of  $h$ , the late ISW effect due to the onset of the dark energy era is negligible, opening up room for a hyperlight scalar to induce more of a ISW contribution to the CMB on large scales. The 95th percentile of the marginalized posteriors over  $F_\phi$  thus increase from 0.0127 when no constants vary to 0.0152 when  $m_{e,i}$  varies. (We note that our results without varying constants are consistent with those from Ref. [139], which obtains bounds of order  $10^{-2}$  for masses  $10^{-30} \lesssim m_\phi/\text{eV} \lesssim 10^{-28}$ .) Such strong constraints demonstrate how sensitive *Planck* is to the dynamics of dark matter perturbations.

For scalars with photon couplings (which are already strongly constrained by high-multipole *Planck* measurements) we might expect the constraints on  $F_\phi$  to correspond closely to constraints on hyperlight scalar fields without varying constants. Figure 14 corroborates this expectation: the marginalized posterior over  $F_\phi$  is unchanged relative to  $\Lambda$ CDM. The results in Fig. 14 do, on the other hand, exhibit a slight anticorrelation between  $F_\phi$  and  $h$  in all cases, even for  $\Lambda$ CDM with a hyperlight scalar field. This effect may in part be again understood via the arguments of Section III A regarding the scalar’s effect on the distance to last scattering: at constant  $a_\star$ , Eq. (3.5) shows that fixing the size of the sound horizon  $\theta_s$  requires  $h \propto A_m^{-2.09} \sim (1 + F_\phi)^{-2.09}$ . For the varying- $m_e$  scenario, the impact of this effect is negligible compared to the degeneracy between  $h$  and  $m_{e,i}$ . As such, the CMB residuals depicted in Fig. 11 are qualitatively unchanged by the inclusion of a scalar, and similar conclusions may be drawn.

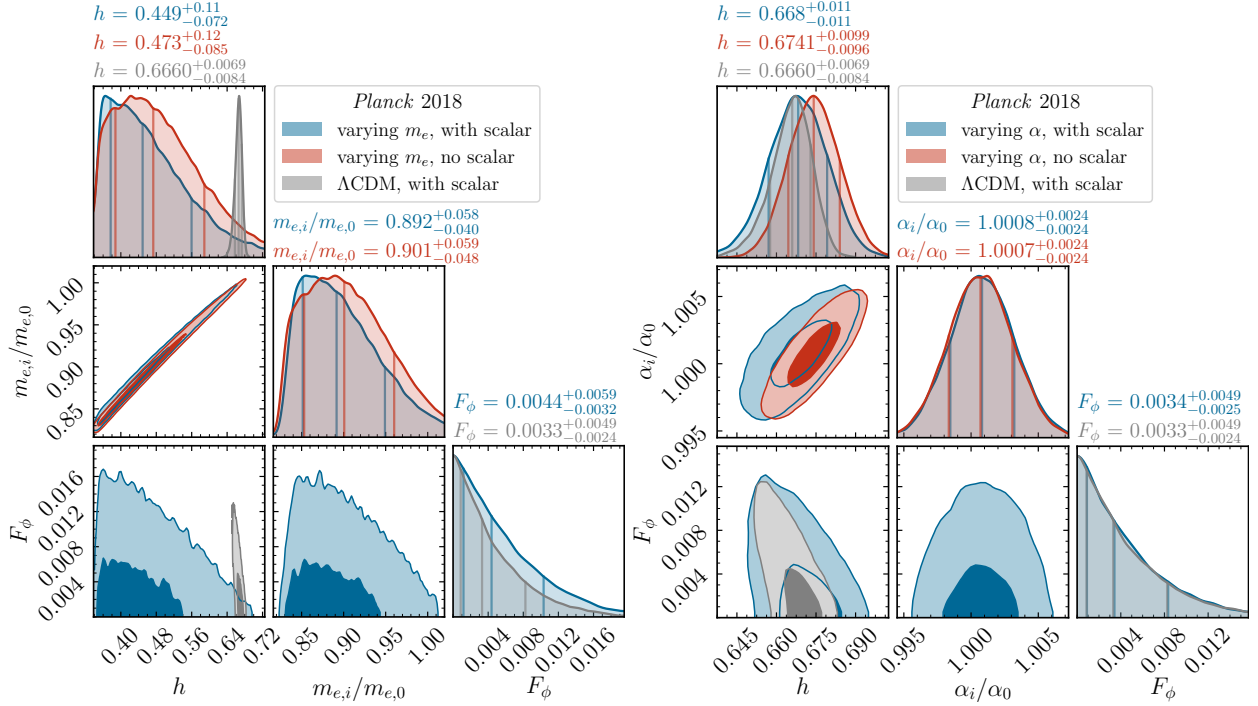


Figure 14. Posterior distribution over  $h$ ,  $m_{e,i}/m_{e,0}$  (left) or  $\alpha_i/\alpha_0$  (right), and the fraction  $F_\phi$  of the CDM density contributed by a scalar field with mass  $10^{-30}$  eV. Depicted are results for varying constant scenarios without (blue) and with (red) scalar fields as well as for  $\Lambda$ CDM with a scalar field (grey), all using *Planck* 2018 likelihoods alone. The diagonal panels display kernel density estimates of the one-dimensional, marginalized posterior relative to their peak value, and the lower panels depict 1 and  $2\sigma$  mass levels of the two-dimensional joint posterior, again slightly smoothed to facilitate comparison.

## 2. Impact of low-redshift distance measurements

While *Planck*'s preference is for  $m_{e,i} < m_{e,0}$ , preempting the regime in which the scalar's could realize a novel degeneracy direction, the features in the data that drive it hold only marginal constraining power. We might therefore only expect this degeneracy to bear out when including direct measurements of the late-time expansion history that would yield stronger constraints on  $a_{m-\Lambda}$ . In particular, per Section III A, fixing  $\theta_s$  requires a disproportionate increase in  $\omega_\Lambda$  relative to that in  $\omega_c$  and  $\omega_b$  (imposed by the structure of the acoustic peaks); late dark matter provides a means to restore the relative amount of dark energy and matter at late times. Including a hyperlight scalar field in the cosmological background thus opens up a degeneracy that can satisfy both CMB and BAO measurements of the angular size of the sound horizon at any value of  $m_{e,i}$ . On the other hand, Fig. 14 show that the CMB disfavors a substantial contribution from a hyperlight scalar, even without varying constants; the arguments of Section III B suggest this is due to its effects on the dynamics of perturbations. We now test whether including low-redshift distance data drives the former effect to outweigh the CMB's constraints on the latter and realizes the degeneracy anticipated in Section III A. Given that BAO data has a substantial impact on  $m_{e,i}$  constraints (Fig. 12), we also assess whether other low-redshift distance datasets independently exhibit similar preferences.

Figure 15 indicates that low-redshift distance data do not outweigh *Planck*'s constraining power on nonclustering subcomponents of dark matter: the degeneracy of Section III A where  $h \propto m_{e,i}$  is not realized. The posteriors in the  $h$ - $m_{e,i}$  plane still lie along the same parameter direction

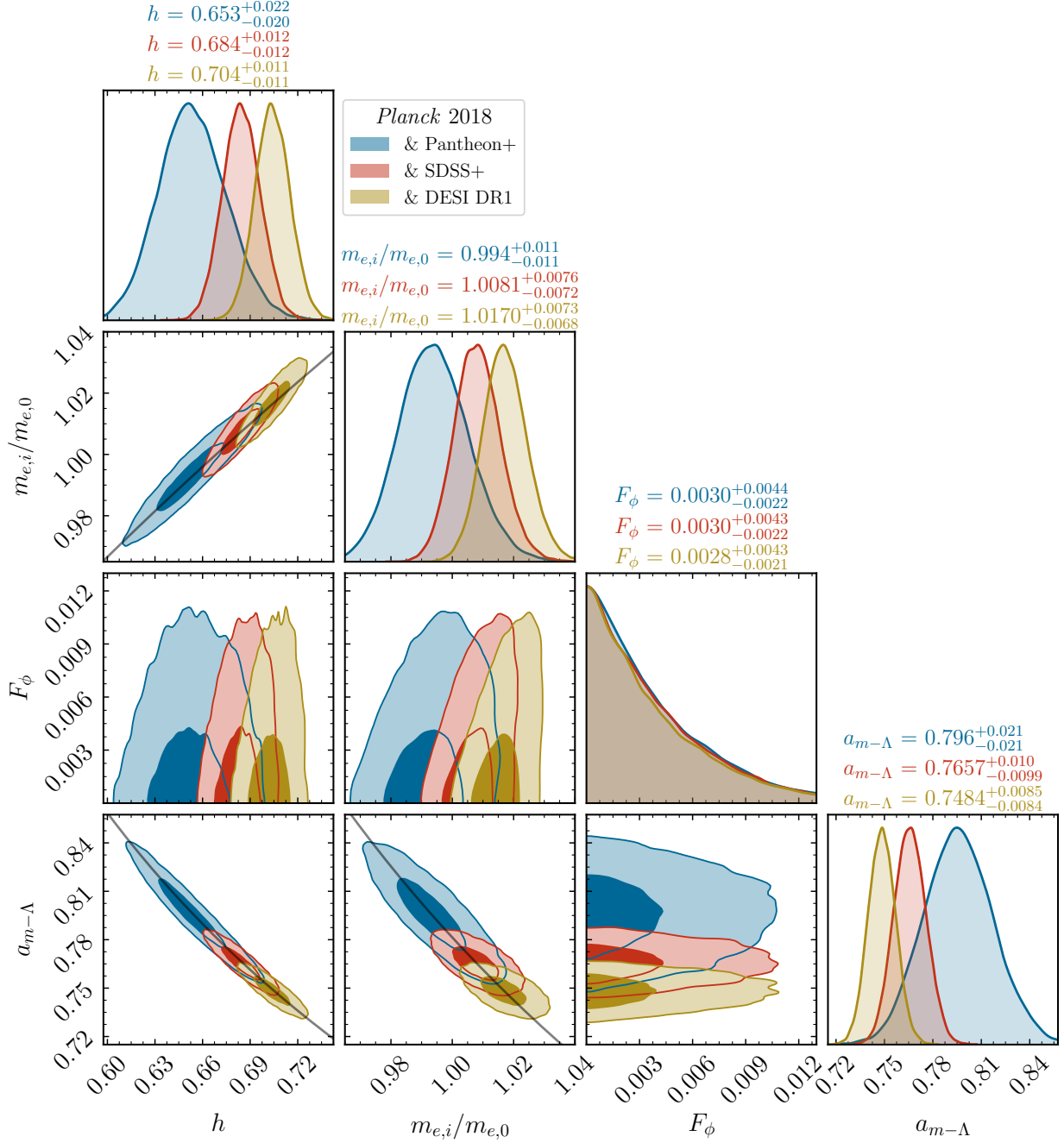


Figure 15. Posterior distribution over a subset of the parameters of the electron-coupled scalar model (with  $m_\phi = 10^{-30}$  eV) and the scale factor of matter–dark-energy equality  $a_{m-\Lambda}$ . Posteriors use the likelihood for the full set of *Planck* 2018 data separately combined with the Pantheon+ (blue), SDSS+ BAO (red), and DESI DR1 BAO (gold) datasets. The 1 and 2 $\sigma$  contours of the marginalized two-dimensional posteriors are depicted as in Fig. 14. Grey lines depict the degeneracy inferred from Eq. (2.26) for scenarios *without* a scalar field, i.e., with  $\omega_m \propto m_{e,i}$  and  $h \propto m_{e,i}^{3.18}$ .

as for phenomenological varying constants (Figs. 12 and 13). The joint posteriors over  $m_{e,i}$  and  $F_\phi$  do, however, display some degree of correlation, indicating that the relationship expected in Section III A would hold more clearly if the CMB did not disfavor the effect of hyperlight scalars



on spatial perturbations. Indeed, the marginalized posteriors over  $F_\phi$  are identical among the four cases, and the constraints are (marginally) sharpened compared to that for *Planck* alone (Fig. 14).

Finally, we note that our electron-coupling results are nearly insensitive to the scalar’s mass  $m_\phi$  in the range  $10^{-31}$  eV to  $10^{-29}$  eV. In particular, the marginalized posteriors over the standard  $\Lambda$ CDM parameters and  $m_{e,i}$  do not change to a discernible degree for any choice of dataset combination. Constraints on  $F_\phi$  are slightly more sensitive to  $m_\phi$ , but in a manner entirely consistent with constraints on ultralight axions of Ref. [139]. For  $m_\phi/\text{eV} = 10^{-29}$ ,  $10^{-30}$ , and  $10^{-31}$ , we obtain 95% upper limits of  $10^2 F_\phi = 1.01$ , 1.12, and 1.79, respectively, from *Planck* 2018 combined with the SDSS+ BAO dataset. These results again indicate that the constraints on  $F_\phi$  are largely driven by effects that are not significantly correlated with any other cosmological parameter.<sup>4</sup> Given that the scalar’s gravitational effect is predominantly on large scales, we have no reason to suspect different findings for scalars coupled instead to the photon.

These results illustrate the power of the CMB to discriminate between models of small subcomponents of dark matter, even independent of their effect on the background cosmology. Though hyperlight scalars are not a successful realization of late dark matter, other possibilities with different dynamics could well be. In fact, the Standard Model provides one such candidate: massive neutrinos, which we consider now.

### 3. Comparison to massive neutrinos

Having established that hyperlight scalars modify structure growth too severely to make a sizeable contribution to the late-time matter abundance, we consider another realization of late dark matter that is contained within the SM: massive neutrinos. One could simultaneously vary the neutrino masses and include a hyperlight scalar as a microphysical realization of varying constants, but the results are not materially different. As discussed in Section III A, within  $\Lambda$ CDM massive neutrinos increase the matter density after recombination, requiring a reduced dark energy density (and so a smaller  $h$ ) to offset the decrease in distance to last scattering (just as for a hyperlight scalar). A BAO measurement of  $hr_d$  (see Section II B 2) breaks this degeneracy, yielding the strongest current constraints on neutrino masses from cosmological data [75, 156]. DESI’s first data release, already reaching the level precision of prior surveys, yields stronger constraints on  $\sum m_\nu$  that are driven by its preference for  $hr_d$  several percent (or  $\sim 1\sigma$ ) larger relative to SDSS’s [156].<sup>5</sup>

Since late dark matter allows for early recombination without altering the relative amount of dark energy and matter at late times,  $h$  and  $\sum m_\nu$  are instead positively correlated. Figure 16 compares results in varying- $m_e$  scenarios featuring late dark matter in the form of a massive neutrino or a hyperlight scalar. We sample over the neutrino mass with a uniform prior between 0 and 1 eV. The tail of the posterior density over  $(\omega_\nu + \omega_\phi)/(\omega_c + \omega_b)$ , i.e., the increase in the matter density at late times, demonstrates the *Planck* tolerates a marginally larger abundance of late dark matter in the form of neutrinos than in a hyperlight scalar. The posteriors for the hyperlight scalar scenario are centered at slightly larger  $h$  and  $m_{e,i}$  only because this case takes a fiducial neutrino mass  $m_\nu = 0.06$  eV, which effectively imposes a prior  $(\omega_\nu + \omega_\phi)/(\omega_c + \omega_b) > 5 \times 10^{-3}$ . Because (uncalibrated) BAO distances depend only on the background cosmology at late times, the marginal posteriors over  $a_{m-\Lambda}$  are effectively identical. Ultimately, hyperlight scalars and massive neutrinos are comparably constrained as late dark matter components because their dynamics are qualitatively similar (as discussed in Section III).

<sup>4</sup> Ref. [139] shows that constraints from *Planck* 2018 data improve upon the 2015 data release due to an improved measurement of  $\tau_{\text{reion}}$ , which breaks a degeneracy between  $A_s e^{-2\tau_{\text{reion}}}$  and  $F_\phi$  that arises from a hyperlight scalar’s suppression of large-scale power.

<sup>5</sup> Part of this shift is due to DESI LRG datapoints, which are in up to a  $3\sigma$  tension with SDSS in some redshift bins [156]; future data releases may clarify whether this discrepancy is statistical.



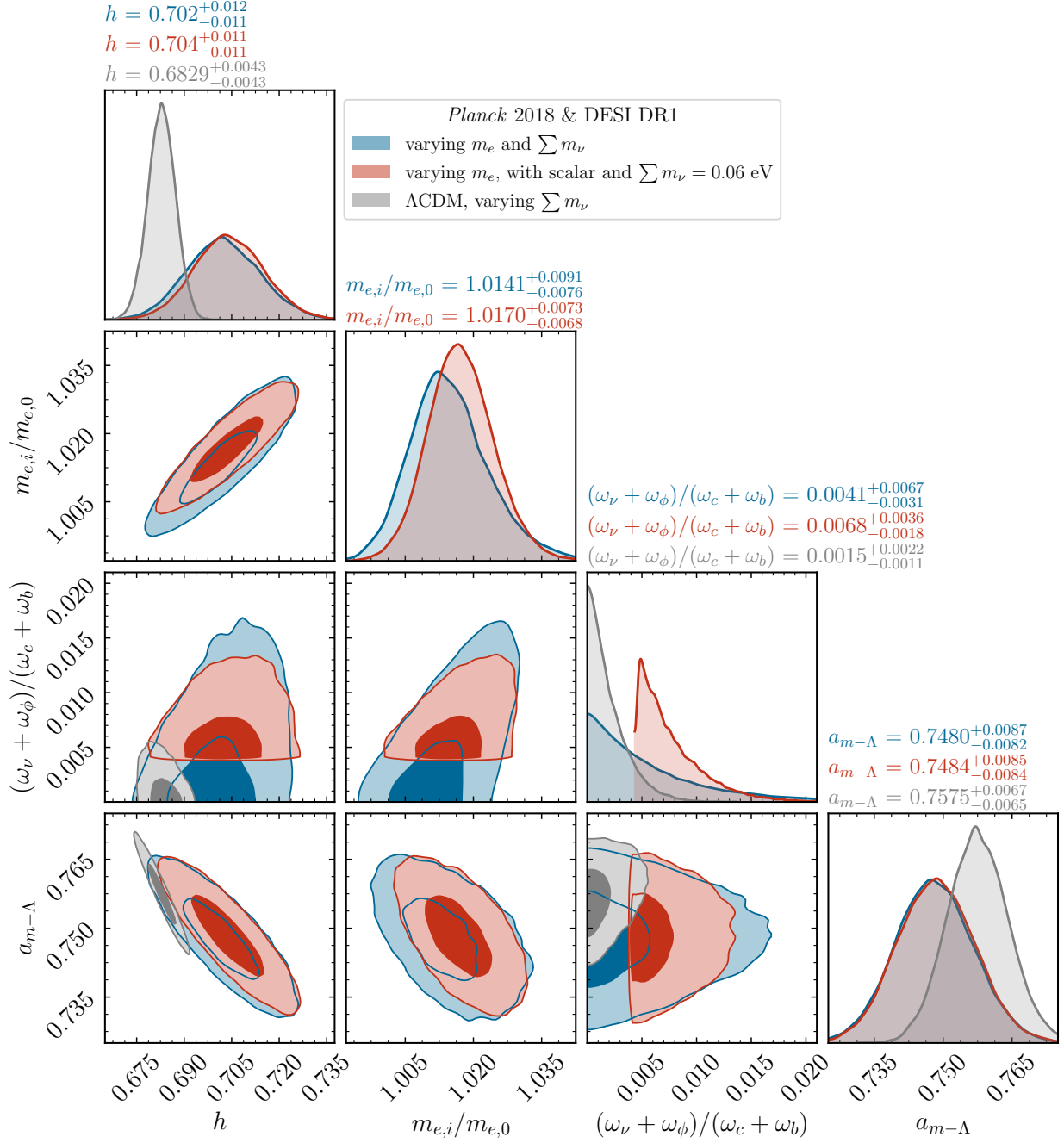


Figure 16. Comparison of posterior distributions in scenarios varying the electron mass and the abundance of a late dark matter component from either massive neutrinos (blue) or a new, hyperlight scalar with mass  $10^{-30}$  eV (red). Results for  $\Lambda$ CDM with a varying neutrino mass are depicted in grey for comparison. Each scenario takes a single massive neutrino state whose mass either is a free parameter or, in the case that includes a scalar, is fixed to 0.06 eV. The posterior is depicted over the Hubble constant  $h$ , the early-time electron mass  $m_{e,i}/m_{e,0}$ , the net abundance of late dark matter relative to baryons and CDM  $(\omega_\nu + \omega_\phi)/(\omega_c + \omega_b)$ , and the scale factor of matter–dark-energy equality  $a_{m-\Lambda}$ . All results use the likelihood for the full set of *Planck* 2018 data combined with DESI DR1 BAO data. The 1 and 2 $\sigma$  contours of the marginalized two-dimensional posteriors are depicted as in Fig. 14 and the diagonal panels depict the one-dimensional marginal posteriors, each normalized to unity.

The 95th percentile of the posterior over  $\sum m_\nu$  increases from 0.073 eV in  $\Lambda$ CDM to 0.239 eV when varying the early-time electron mass, similar to that found in Ref. [23]. The latter result precisely matches the constraint within  $\Lambda$ CDM from *Planck* 2018 data alone (i.e., without BAO data) [75], which again establishes that the primary constraints on early recombination with late dark matter derive from the new component’s effects on structure and not those on the expansion history. This result also highlights the sensitivity of cosmological inference of the neutrino masses to the underlying cosmological model: the  $\Lambda$ CDM result nearly rules out the inverted mass hierarchy, in early recombination scenarios cosmological data provide no discriminatory power.

### C. Implications for cosmological concordance

The findings of the previous sections for varying- $m_e$  cosmologies—the impact of consistently including a scalar field as a microphysical realization of the scenario and the lack of strong concordance among datasets—have important implications for the interpretation of contemporary tensions between cosmological datasets. Prior literature pointed to the degeneracy of the varying- $m_e$  model as a preferred means to infer a larger Hubble constant from CMB data [20–23] that could be (relatively more) consistent with that measured via the distance ladder [24–26]. The results of Fig. 8, however, suggest that the CMB by itself prefers negligible dark energy in models where its abundance is not predominantly fixed by the distance to last scattering, because such models have the additional freedom to better fit the deficit in temperature power on large scales and the excess lensing of the acoustic peaks (relative to  $\Lambda$ CDM) evident in *Planck* 2018 data.

On its own, *Planck* 2018 data therefore prefers late recombination: a lighter early-time electron mass and an even lower value of  $h$  than in  $\Lambda$ CDM, regardless of whether one accounts for the gravitational effect of a scalar field coupled to the electron. This finding, though evident in prior work [20, 22] (and to a slightly lesser extent in results using previous *Planck* data releases [59, 60]), has not been emphasized in discussions of the model as a solution to the Hubble tension, nor has its physical origin been explored. Though the broad posteriors superficially appear to reduce the tension, in no region of parameter space does the model *simultaneously* improve the fit to both CMB data and the calibrated distance-ladder datasets that prefer larger  $h$ .<sup>6</sup> Setting aside questions of whether the lensing and low- $\ell$  anomalies have a statistical or systematic origin, we conclude that a varying electron mass alone does not meaningfully restore concordance of these datasets.

*Planck*’s preference for late recombination derives from features that can be better explained by delaying the transition to dark-energy domination, but SNe and BAO distances directly measure the shape of the expansion history (i.e.,  $a_{m-\Lambda}$ ) in this epoch. Figure 15 shows that even these direct probes (each combined with *Planck* and without external calibration for SNe) are far from concordant within the varying- $m_e$  model. Because  $h$  and  $m_{e,i}$  correlate so strongly with  $a_{m-\Lambda}$ , their marginal posteriors only agree to the extent of the datasets’ individual preferences for  $a_{m-\Lambda}$ .<sup>7</sup> Results inferred from current SNe and BAO datasets are particularly discrepant, as evident in Fig. 17. These divergent preferences are especially pronounced for the very recent Union3 and DES 5YR SNe datasets, which both prefer a transition to dark-energy domination even later than does the Pantheon+ result, yielding correspondingly smaller  $h$  and  $m_{e,i}$ . Curiously, the posteriors from the 2018 Pantheon dataset in Fig. 17, though much broader than the others, agree much better with *Planck* combined with either BAO dataset.

<sup>6</sup> Ref. [178] succinctly makes the general point that a proper Bayesian interpretation of a model’s compatibility with multiple datasets requires marginalizing likelihoods over parameter space—i.e., metrics beyond the improvement to the best fit point (a point in parameter space with vanishing posterior mass) or the number of standard deviations between inferred parameter values (which provides little information on whether a model better explains different datasets in the same part of parameter space).

<sup>7</sup> Constraints on the flat  $\Lambda$ CDM model are usually quoted in terms of  $\Omega_m$ . We center our discussion on  $a_{m-\Lambda} = \sqrt[3]{\Omega_m/(1 - \Omega_m)}$  both because it more directly connects to the shape of the late-time expansion history and because a late dark matter component (like a hyperlight scalar) changes the late-time matter abundance but not the early-time one (Section III A).

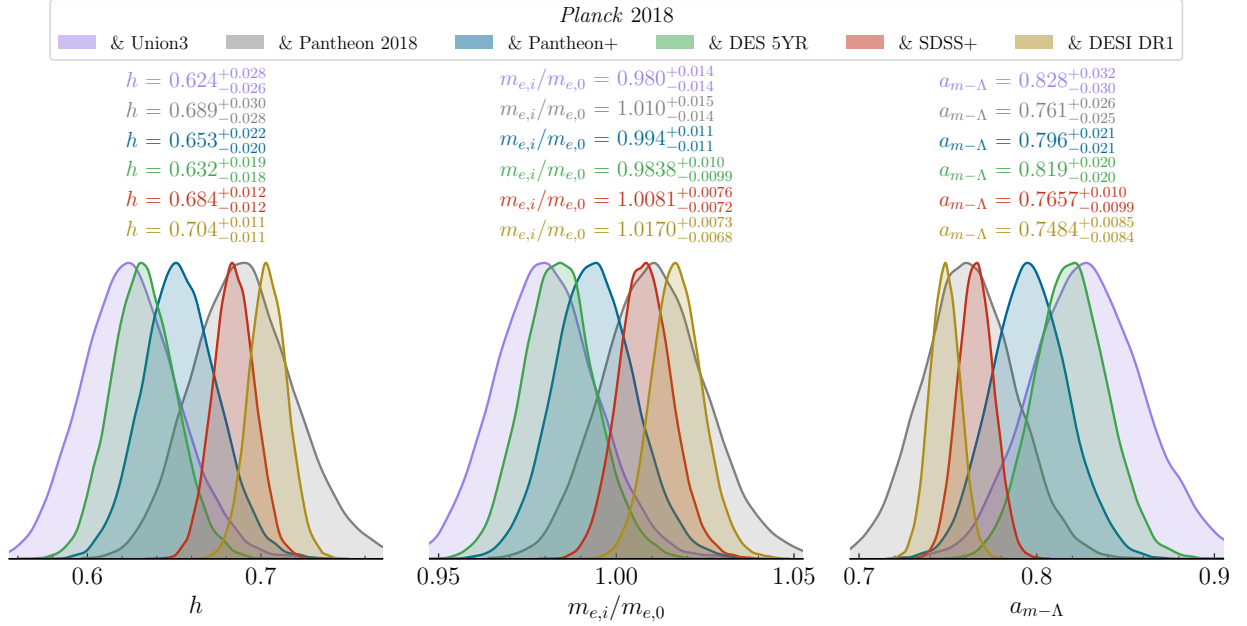


Figure 17. Posterior distributions over  $h$ ,  $m_{e,i}/m_{e,0}$ , and  $a_{m-\Lambda}$  for the electron-coupled scalar model (with  $m_\phi = 10^{-30}$  eV), using the likelihood for the full set of *Planck* 2018 data separately combined with the Pantheon 2018 (grey), Pantheon+ (blue), DES 5YR (green), SDSS+ BAO (red), and DESI DR1 BAO (gold) datasets. Titles report the corresponding median and  $\pm 1\sigma$  quantiles of each distribution. Note that results for the varying- $m_e$  model without a scalar field are nearly identical, with posteriors over  $h$  and  $m_{e,i}$  shifted marginally to lower values.

These discrepancies in late time datasets yield highly divergent interpretations of concordance. At one end, the naïve Gaussian tension between *Planck* combined with DES ( $h \approx 0.632 \pm 0.018$ ) remains above the  $5\sigma$  level with Pantheon+ and SH0ES ( $h \approx 0.735 \pm 0.01$ ) [96], despite the broader posteriors over  $h$  afforded by early recombination scenarios. In strong contrast, *Planck* combined with DESI yields  $h \approx 0.704 \pm 0.011$ , apparently a mere  $2\sigma$  discrepancy with Pantheon+ and SH0ES. We reiterate that a substantial contribution to DESI's preference for larger  $h$  is driven by its LRG data, which within  $\Lambda$ CDM are in slight tension with SDSS's [156]. Finally, because  $h$  varies rather rapidly with the electron mass at fixed  $\theta_s$ , the discrepancy in measurements of  $m_{e,i}$  in Fig. 17 is less severe but still impedes a quantitative identification of a consensus constraint from cosmological datasets on  $m_{e,i}$ .

Setting aside the more discrepant datasets (Fig. 17), even the improved agreement on  $h$  in early recombination scenarios between the *Planck* and DESI combination and the SH0ES-calibrated distance ladder does not fully capture the degree of the tension. These two dataset combinations are also in a  $2\sigma$  tension in their (marginalized) posteriors over  $a_{m-\Lambda}$ , as seen in Fig. 17. Moreover,  $h$  and  $a_{m-\Lambda}$  are anticorrelated in early recombination models as constrained by *Planck*, such that decreasing the discrepancy in one of  $h$  or  $a_{m-\Lambda}$  only exacerbates that in the other. Concordance must be assessed in the full two-dimensional parameter space that characterizes the late-Universe expansion history; as shown in Fig. 18, the posteriors in the  $h$ - $a_{m-\Lambda}$  plane hardly overlap even in their  $3\sigma$  mass levels. While a late dark matter contribution could increase  $h$  without reducing  $a_{m-\Lambda}$  in principle (Section III A), within the hyperlight scalar field model *Planck* does not allow abundances large enough to do so. Even in a scenario where this additional degeneracy is realized, the discrepant inference of  $a_{m-\Lambda}$  by BAO and SNe data (which trace the same interval of redshift) cannot be fully reconciled—a problem for any model in which the late-time expansion history is

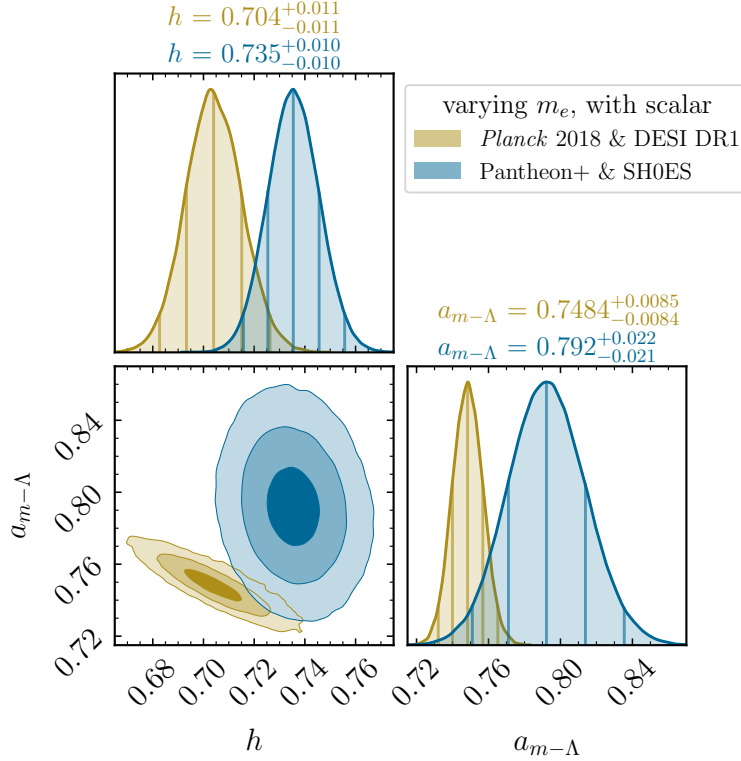


Figure 18. Posterior distribution over  $h$  and  $a_{m-\Lambda}$  from *Planck* 2018 and DESI DR1 BAO data for the electron-coupled scalar model (gold) and from Pantheon+ with SH0ES-calibrated Cepheids (blue). The vertical lines in the diagonal panels depict the median and 2.5th, 16th, 84th, and 97.5th percentiles of the marginalized posterior distributions. These one-dimensional posteriors are kernel density estimates normalized relative to their peak value to facilitate comparison. The median and corresponding  $\pm 1\sigma$  uncertainties for each parameter are reported above the diagonal panels. The lower panels display the 1, 2, and  $3\sigma$  contours (i.e., the 39.3%, 86.5%, and 98.9% mass levels) of the marginalized, two-dimensional posterior.

well described by flat  $\Lambda$ CDM.

For these reasons, we do not analyze the combination of *Planck* 2018 data with the SH0ES-calibrated distance ladder. Posteriors for these combined datasets would localize at parameters between their individual preferences, obfuscating the fact that the individual likelihoods are degraded in this resulting parameter space. Prior work has in addition admonished the usage of a SH0ES-derived prior directly on  $H_0$ , emphasizing the importance of including the full magnitude-redshift sample from Pantheon SNe, calibrated by SH0ES Cepheids, to provide genuine constraints on modifications to late-time cosmology [179, 180]. Our results demonstrate the importance of doing so more generally, because modifications to early-time cosmology can correlate to changes in the late-time expansion history. In early recombination models, the disproportionate increase in the matter and dark-energy densities cause the late-time expansion history to depart (in shape, or  $a_{m-\Lambda}$ ) from that directly measured by current SN datasets, underscoring the potential hazards in interpreting analyses that combine the Cepheid-calibrated distance ladder with CMB (and BAO) data.

As anticipated in Section II A 6, our results bear a close resemblance to those for the (counterfactual) cosmologies in which the present-day CMB temperature  $T_0$  is treated as an otherwise unconstrained parameter [38, 181]. The correlated impact on the late-time expansion history is common to both scenarios, as is the role of CMB lensing and the ISW effect [38, 182]. The preceding considerations also apply (to a reasonable extent) to early recombination mechanized by small-scale

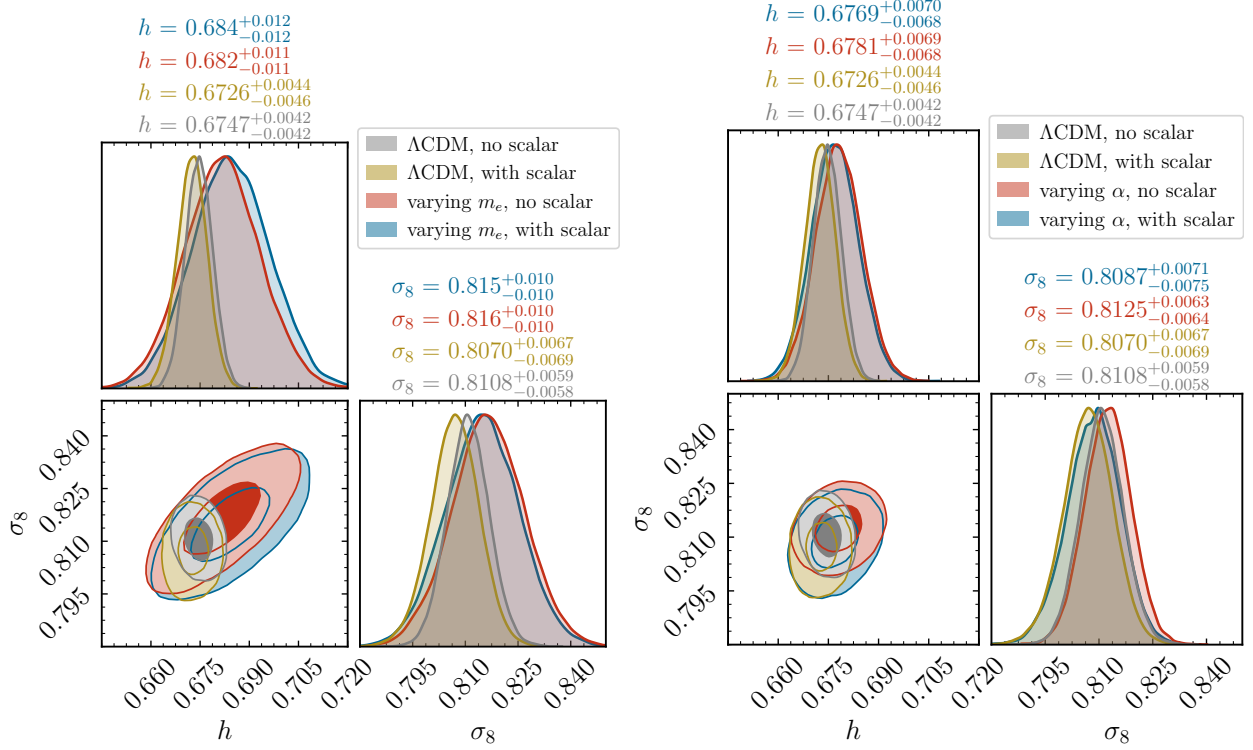


Figure 19. Posterior distribution over  $h$  and  $\sigma_8$  (the latter a derived quantity) in scenarios vary  $m_{e,i}/m_{e,0}$  (left) or  $\alpha_i/\alpha_0$  (right). Both cases also compare results with  $\Lambda$ CDM with and without a scalar. Scenarios with a scalar field take its mass to be  $10^{-30}$  eV, and all cases use *Planck* 2018 likelihoods and the SDSS+BAO datasets enumerated in the text.

inhomogeneities in the baryon distribution [78–81] mentioned in Section II A 6. These scenarios only prefer a larger Hubble constant when combining *Planck* data with datasets like SH0ES [78], indicating that (superficially) alleviating the tension comes at the cost of degrading the *Planck* likelihoods.

Having assessed the joint effect of varying constants and hyperlight scalars on the background evolution in the  $h$ - $a_{m-\Lambda}$  space, we now turn to the model’s impact on matter clustering and the Hubble constant. Low-redshift probes prefer larger  $h$  but smaller  $\sigma_8$  (or  $S_8 \equiv \sqrt{\Omega_m/0.3}$ ), but a common feature of proposed  $\Lambda$ CDM extensions is a positive correlation between, e.g.,  $h$  and  $\sigma_8$  [183, 184]. This expectation may be understood on general grounds via the arguments of Section II: the radiation driving and early ISW effects constrain the CDM abundance at recombination, requiring a larger matter abundance today if recombination occurs at higher density, whether because it occurs early or in the presence of additional new degrees of freedom. Absent other effects, early-time modifications to cosmology that lead to inference of larger  $h$  typically also infer a larger amplitude of matter clustering.

On the other hand, per Section III B (and, e.g., Ref. [139]), a hyperlight scalar subcomponent of dark matter in general suppresses matter clustering. The correlation between the abundance of the scalar ( $F_\phi$ ) and the early-time shift in the electron mass ( $m_{e,i}/m_{e,0} - 1$ ) outlined in Section III A would achieve an anticorrelation between  $h$  and  $\sigma_8$  if it had borne out in the full data analysis. Indeed, Fig. 19 evinces a broadening of the posteriors (projected into the space of  $h$  and  $\sigma_8$ ) in this direction for varying- $m_e$  cosmologies that include a scalar compared to those that do not. However, *Planck* data itself ultimately curtails the extent of this effect in parameter space; the results here ultimately do not depart dramatically from those of Ref. [139], which considered hyperlight scalars

with only gravitational interactions. The degree of the effect is comparable to the extent hyperlight scalars may reduce  $\sigma_8$  in standard  $\Lambda$ CDM, except that (as explained in Section IV B)  $F_\phi$  and  $h$  are themselves anticorrelated in this case. Coupled hyperlight scalars therefore provide at the least an example model that can accommodate CMB data at larger  $h$  but smaller  $\sigma_8$ .

## V. CONCLUSIONS

The cosmic microwave background, long lauded as a precision probe of the early Universe, depends sensitively on the physics of quantum electrodynamics. In this work we consider microphysical realizations of scenarios in which the fundamental parameters of QED—the electromagnetic fine-structure constant and electron mass—take on different values during recombination than at the present day. Companion work [32] discusses theories of new scalar fields whose couplings vary fundamental constants in spacetime, emphasizing that consistency with theoretical considerations and independent probes restricts the viable space of models. Crucially, Ref. [32] shows that mechanizing shifted early-time fundamental constants that only start evolving toward their present-day values after recombination *requires* the scalar field to have a nonnegligible abundance. Here we investigate the cosmological impact of a new scalar through both its direct coupling and its gravitational coupling to SM matter.

Variations in the fine-structure constant and the electron mass, regardless of their origin, primarily affect the release of the CMB via their well-studied impacts on recombination, shifting the temperature and duration of last scattering, and on Thomson scattering. These effects are not independently constrained by data in  $\Lambda$ CDM cosmology, however; in Section II we clarify the physical origin of degeneracies between the fundamental constants and  $\Lambda$ CDM parameters. In particular, we enumerate how CMB anisotropies largely probe the state of the Universe at last scattering, whenever it may have occurred, and how the rate of recombination—namely, the redshift interval over which visible CMB photons last scattered—impacts the generation of polarization and the suppression of small-scale anisotropies. Sections II A and III A describe the combinations of standard parameters that directly encode the most important physical effects that imprint in CMB anisotropies, generalizing those of prior work [77, 185, 186]. In doing so, we uncover the connection between modified recombination scenarios and the CMB monopole temperature, if treated as an otherwise unmeasured parameter. In particular, when either of the present-day CMB temperature and the early-time electron mass is not fixed, the Hubble constant is no longer uniquely constrained to fix the angular extent of the sound horizon precisely measured by CMB anisotropies—the same “geometric” degeneracy characteristic to cosmologies with nonzero spatial curvature [185].

The correlation of fundamental constants with  $\Lambda$ CDM parameters inevitably affects cosmological dynamics at late times, to which the CMB anisotropies are only weakly sensitive. Low-redshift distance measurements, whether from type Ia supernovae or baryon acoustic oscillations, therefore play a crucial role in breaking degeneracies by directly measuring the shape of the late-time expansion history, even without calibrating their absolute distances. When including low-redshift distance datasets, cosmological data constrain electron mass variations at the percent level and fine-structure constant variations at nearly the permille level. On the other hand, Section III A identifies a novel solution that combines early recombination with “late dark matter,” i.e., an enhancement of the matter abundance after recombination. The SM already offers a source of late dark matter: massive neutrinos, which become nonrelativistic well before the present but after recombination. Moreover, Section III shows that a hyperlight scalar field, invoked to mechanize variation of fundamental constants between recombination and the present day, must begin oscillating and boost the matter abundance after recombination as well. The positive correlation between  $h$  and the abundance of late dark matter (measured by the sum of the neutrino masses or by  $F_\phi$  for a scalar) along this



degeneracy is especially notable in contrast to the *anticorrelation* between the two in  $\Lambda$ CDM.

Though early recombination with late dark matter realizes a degeneracy in the cosmological background, the scenarios are distinguished (and therefore testable) through the behavior of the new component’s perturbations. Section IV carefully studies the complementary impact of individual datasets in constraining these scenarios and provides quantitative evidence for the physical effects outlined in Sections II and III. Section IV B further illustrates how the perturbations of a hyperlight scalar suppress the growth of structure and source an integrated Sachs-Wolfe effect, signatures which ultimately restrict the scalar abundance allowed by *Planck* data to no more than  $\mathcal{O}(1\%)$  of the dark matter’s.

A heavier electron at early times, which triggers recombination at a higher temperature, has been touted as an extension to  $\Lambda$ CDM for which cosmological data infer a Hubble constant  $H_0$  in better agreement with distance-ladder measurements. In Section IV C we critically assess this claim, arguing that because the physical effects of Section II lead *Planck* data to prefer late recombination to early recombination, a superficial reduction in the  $H_0$  tension comes at the cost of degrading the fit to individual cosmological datasets. Moreover, though the degeneracy introduced by the scalar’s contribution to the late-time matter abundance (identified in Section III) offers the potential to simultaneously satisfy CMB and low-redshift observations at arbitrarily large  $H_0$ , *Planck* data too strongly disfavors the impact of a hyperlight scalar’s perturbations to fully realize this effect. To the extent that *Planck* data *does* allow for hyperlight scalars, however, slightly larger electron masses and Hubble constants are allowed compared to scenarios without a scalar. We show that similar conclusions apply to massive neutrinos as an alternative realization of late dark matter. An interesting question for further study is whether any motivated models of late dark matter affect the dynamics of perturbations in a manner the CMB is more amenable to.

Because low-redshift datasets play such a crucial role in breaking degeneracies in varying electron mass scenarios, any discord between them is put on full display. Sections IV A 2 and IV B 2 show that the diverging preferences in the uncalibrated late-time expansion history (i.e., its shape as encoded by the scale factor of matter–dark-energy equality  $a_{m-\Lambda}$ ) propagate directly to the electron mass and  $h$ . In particular, Section IV C highlights an increasing discrepancy in the cosmologies preferred by recent BAO datasets and recent SNe datasets that, combined with *Planck*, vary in their inferred  $h$  between  $0.704 \pm 0.011$  and  $0.632 \pm 0.018$ . The former result derives from the recent DESI DR1 BAO measurements [156–158] and is larger than that from prior BAO data, a shift driven in part by an increase its inferred the dimensionless amplitude  $hr_d$ . Section IV C also emphasizes the importance of a holistic interpretation of the agreement between posteriors derived from, e.g., CMB and BAO data with those from the SH0ES-calibrated distance ladder: even with the additional freedom afforded to early-recombination (and varying- $T_0$ ) cosmologies, no independent dataset combination prefers a late-time expansion history that agrees with the SH0ES-calibrated distance ladder in both calibration ( $h$ ) and shape ( $a_{m-\Lambda}$ ).

Future high-resolution CMB observations [48, 187] will greatly improve measurements of temperature and polarization anisotropies deep into the damping tail, promising substantially stronger constraints on fine-structure constant variations. Even current and near-term datasets from ground-based experiments [170–172] offer increased constraining potential. While no physical effect positions high-resolution observations to better constrain electron-mass variations, alternative CMB datasets can weigh in on the influence of features in *Planck* data suspected to be systematic in origin. The lensing anomaly in particular is absent in other datasets, including recent reanalyses of *Planck* data [188, 189]. Bounds on the abundance of hyperlight scalars (coupled to the SM or not) could too be alleviated because the same systematic effects effectively disfavor the their impact on structure growth, as has already been observed for bounds on the neutrino masses [189]. Future BAO and SNe datasets will also provide substantially more precise measurements of the late-time expansion history, better breaking degeneracies in CMB constraints on early recombination. We will study

constraints from these more recent datasets and forecast bounds from upcoming observations in future work.

In a companion article [32], we apply the results of Section IV B to constrain concrete extensions of the SM with new scalar fields coupled to the electron and photon. Ref. [32] discusses numerous challenges in constructing models that are both theoretically consistent and allowed by independent constraints from other astrophysical and laboratory measurements. In viable theories, the cosmological constraints of Section IV B in particular yield leading bounds on hyperlight, quadratically coupled scalars that become matterlike in the matter dominated era.

This work restricts its analysis to regimes that realize the phenomenological scenarios of prior study, in which the change to the fundamental constants remains fixed through recombination. The theoretical developments of Ref. [32], however, motivate scenarios in which the scalar (and so the fundamental constants) evolve before recombination under the influence of the cosmological abundance of SM matter. Such a regime resembles attempts to address coincidence problems in early dark energy via couplings to dark matter [190, 191] or neutrinos [192, 193] to explain why the early dark energy field becomes dynamical around the time of recombination. Moreover, a complete treatment of coupled scalars requires an extension to heavier masses for which the scalar begins oscillating before recombination of its own volition. Time-dependent fundamental constants around recombination may yield qualitatively different CMB signatures via, for instance, the interplay of changes to the shape of the visibility function and diffusion damping rate at earlier times.

In addition, scalars may equally well couple to other SM content like the Higgs, quarks, and gluons, which would affect the masses of baryons and mediate fifth forces between them. Fifth forces between electrons are present in the scenarios we considered here, but their effect is negligible because inhomogeneities in the electron fluid are themselves negligible in linear perturbation theory (see Section III). We leave a general study of the cosmological signatures of coupled scalars, including the effect of evolution prior to recombination and scalar-mediated forces on the CMB and large-scale structure, to future work.

## ACKNOWLEDGMENTS

We thank Nikita Blinov, David Cyncynates, Junwu Huang, Mikhail Ivanov, Hongwan Liu, Cristina Mondino, Caio Nascimento, Maxim Pospelov, Murali Saravanan, Sergey Sibiryakov, Neal Weiner, and Tien-Tien Yu for helpful conversations and especially Marilena Loverde for many useful and extended discussions. M.B. is supported by the U.S. Department of Energy Office of Science under Award Number DE-SC0024375. M.B. and Z.J.W. are supported by the Department of Physics and College of Arts and Science at the University of Washington. O.S. was supported by the Department of Physics and a DARE Fellowship from the Office of the Vice Provost for Graduate Education at Stanford University. This work made use of the software packages `emcee` [194–196], `corner.py` [197], `NumPy` [198], `SciPy` [199], `matplotlib` [200], `xarray` [201], `ArviZ` [202], `SymPy` [203], and `CMasher` [204].

## Appendix A: Numerical implementation of cosmological scalar fields

The gravitational effects of cosmological scalar fields have been studied in contexts including ultralight dark matter [128, 134, 139–142, 205–208], scalar field dark energy [209, 210], and early dark energy [129–131, 133]. A scalar field’s potential typically introduces a new timescale of cosmological importance, which in the simplest case of potentials with minima is the scalar’s oscillation period. Scalars with quadratic potentials generically oscillate with a fixed period much

shorter than the age of the Universe (unless their mass is close to the Hubble constant  $H_0$ , a regime to which we do not restrict ourselves).

To mitigate the onerous computational cost required to accurately solve for scalar fields' dynamics, a variety of effective fluid treatments for scalar fields have been utilized in prior literature [128, 130, 131, 134, 205, 206, 211, 212]. We follow Ref. [121], which systematically developed a fluid approximation for massive scalar fields that enabled semianalytically and empirically calibrating the effective equation of state and sound speed describing the fluid. The scheme devised by Ref. [121] entails solving the scalar's equation of motion (the Klein-Gordon equation) directly for its first few oscillations (when fluid approximations are largely insufficient) before switching to the effective fluid approximation. The matching procedure of Ref. [121] also improves substantially upon prior methods. We extend CLASS [51, 52] by implementing the scheme proposed by Ref. [121] to enable an efficient and accurate treatment of scalar fields. (The implementation is available at Ref. [122].) For completeness, we briefly review the formalism and definitions necessary to specify the scheme, referring to Ref. [121] for full details and comparison with previous fluid treatments.

### 1. Dynamics

In a general spacetime, the action for a minimally coupled scalar field is  $S_\phi = \int d^4x \sqrt{-g} \mathcal{L}_\phi$  in terms of its Lagrangian density

$$\mathcal{L}_\phi = -\frac{1}{2} \partial_\mu \phi \partial^\mu \phi - V(\phi). \quad (\text{A1})$$

The scalar's Euler-Lagrange equation is

$$\nabla_\mu \nabla^\mu \phi = \frac{dV}{d\phi}, \quad (\text{A2})$$

where  $\nabla_\mu$  is the covariant derivative compatible with the metric  $g$ . We parameterize a general, perturbed, conformal-time Friedmann-Lemaître-Robertson-Walker (FLRW) metric with

$$g_{\mu\nu} \equiv a(\tau)^2 (\eta_{\mu\nu} + h_{\mu\nu}) \quad (\text{A3})$$

where  $\eta_{\mu\nu}$  is the Minkowski metric with the mostly positive signature and  $h_{\mu\nu}$  a small perturbation we decompose as

$$h_{00} = -E \quad (\text{A4a})$$

$$h_{i0} = \partial_i F \quad (\text{A4b})$$

$$h_{ij} = A \delta_{ij} + \partial_i \partial_j B. \quad (\text{A4c})$$

Because neither primordial vectors nor tensors have been detected, and because we introduce no new physics that would source them, Eq. (A4) includes only scalar perturbations  $A$ ,  $B$ ,  $E$ , and  $F$ . This parameterization is general but redundant due to gauge invariance; we discuss concrete gauge choices below.

Expanding to linear order with  $\phi(t, \mathbf{x}) = \bar{\phi}(t) + \delta\phi(t, \mathbf{x})$ , the equation of motion Eq. (A2) becomes

$$0 = \bar{\phi}'' + 2\mathcal{H}\bar{\phi}' + a^2 \frac{dV}{d\phi} \quad (\text{A5a})$$

$$0 = \delta\phi'' + 2\mathcal{H}\delta\phi' - \partial_i \partial_i \delta\phi + a^2 \frac{d^2 V}{d\phi^2} \delta\phi + \frac{\bar{\phi}'}{2} (\partial_i \partial_i [B' - 2F] + 3A' - E') + a^2 \frac{dV}{d\phi} E. \quad (\text{A5b})$$

Here primes denote derivatives with respect to conformal time  $\tau$ . The conformal Newtonian gauge has  $E = 2\Psi$ ,  $A = -2\Phi$ , and both  $F$  and  $B$  zero, in which case

$$0 = \delta\phi'' + 2\mathcal{H}\delta\phi' - \partial_i\partial_i\delta\phi + a^2\frac{d^2V}{d\phi^2}\delta\phi - (3\Phi' + \Psi')\bar{\phi}' + 2a^2\frac{dV}{d\phi}\Psi. \quad (\text{A6})$$

The synchronous gauge used in Ref. [213] sets  $A = -2\eta$  and  $\partial_i\partial_i B = h + 6\eta$  with  $E$  and  $F$  zero; Eq. (A5b) then reads

$$0 = \delta\phi'' + 2\mathcal{H}\delta\phi' - \partial_i\partial_i\delta\phi + a^2\frac{d^2V}{d\phi^2}\delta\phi + \frac{1}{2}\bar{\phi}'h'. \quad (\text{A7})$$

The scalar field's contribution to the stress-energy tensor is

$$(T_{\mu\nu})^\phi = -2\frac{\partial\mathcal{L}_\phi}{\partial g^{\mu\nu}} + g_{\mu\nu}\mathcal{L}_\phi = \partial_\mu\phi\partial_\nu\phi + g_{\mu\nu}\left(-\frac{1}{2}\partial_\alpha\phi\partial^\alpha\phi - V(\phi)\right). \quad (\text{A8})$$

At the background level, the effective energy density  $\bar{\rho}_\phi = -(\bar{T}_0^0)^\phi$  and pressure  $\bar{P}_\phi = (\bar{T}_i^i)^\phi/3$  are

$$\bar{\rho}_\phi = \frac{(\bar{\phi}')^2}{2a^2} + V(\bar{\phi}) \quad (\text{A9a})$$

$$\bar{P}_\phi = \frac{(\bar{\phi}')^2}{2a^2} - V(\bar{\phi}). \quad (\text{A9b})$$

We parameterize the scalar perturbations to the stress-energy tensor in terms of density, pressure, and velocity perturbations  $\delta\rho$ ,  $\delta P$ , and  $\delta u$ , as well as anisotropic stress  $\pi^S$ :

$$\delta T_0^0 = -\delta\rho \quad (\text{A10a})$$

$$\delta T_i^0 = (\bar{\rho} + \bar{P})\partial_i\delta u \quad (\text{A10b})$$

$$\delta T_j^i = \delta_{ij}\delta P + \left(\partial_i\partial_j - \frac{1}{3}\delta_{ij}\partial_k\partial_k\right)\pi^S. \quad (\text{A10c})$$

Often the velocity perturbation is written in terms of  $\theta = \partial_i\partial_i\delta u$ . The corresponding contributions from Eq. (A8) (at linear order) are

$$\delta\rho_\phi = -\frac{E}{2a^2}(\bar{\phi}')^2 + \frac{\bar{\phi}'\delta\phi'}{a^2} + \frac{dV}{d\phi}\delta\phi \quad (\text{A11a})$$

$$(\bar{\rho}_\phi + \bar{P}_\phi)\delta u_\phi = -\frac{\bar{\phi}'\delta\phi}{a^2} \quad (\text{A11b})$$

$$\delta P_\phi = -\frac{E}{2a^2}(\bar{\phi}')^2 + \frac{\bar{\phi}'\delta\phi'}{a^2} - \frac{dV}{d\phi}\delta\phi. \quad (\text{A11c})$$

Anisotropic stress from a scalar field is zero to leading order in perturbation theory. Recall again that  $E = 2\Psi$  in Newtonian gauge and 0 in synchronous gauge.

## 2. Effective fluid treatment

We now turn to effective fluid approximations for scalars with purely quadratic potentials,  $V(\phi) = m_\phi^2\phi^2/2$ . Following Ref. [121], we fix synchronous gauge for the remainder of the discussion

and switch to cosmic time  $t$  defined by  $dt = a d\tau$ . With these choices,

$$0 = \ddot{\bar{\phi}} + 3H\dot{\bar{\phi}} + m_\phi^2 \bar{\phi} \quad (\text{A12})$$

$$0 = \delta\ddot{\phi} + 3H\delta\dot{\phi} + \frac{k^2}{a^2}\delta\phi + m_\phi^2\delta\phi + \frac{1}{2}\dot{\phi}\dot{h}, \quad (\text{A13})$$

writing the perturbation equation in Fourier space. In the absence of metric perturbations, these equations both exhibit oscillatory solutions with a decaying envelope.

#### a. Background

Beginning at the background level Ref. [121] decomposes the solution to Eq. (A12) onto its two oscillatory modes as

$$\bar{\phi}(t) = \bar{\varphi}_c(t) \cos(m_\phi t - m_\phi t_\star) + \bar{\varphi}_s(t) \sin(m_\phi t - m_\phi t_\star), \quad (\text{A14})$$

where the amplitudes  $\bar{\varphi}_c$  and  $\bar{\varphi}_s$  evolve slowly (i.e., on timescales order  $1/H$ ). Equation (A12) expands to

$$\begin{aligned} 0 = & [\ddot{\bar{\varphi}}_c + 2m_\phi\dot{\bar{\varphi}}_c + 3H(\dot{\bar{\varphi}}_c + m_\phi\bar{\varphi}_s)] \cos(m_\phi t - m_\phi t_\star) \\ & + [\ddot{\bar{\varphi}}_s - 2m_\phi\dot{\bar{\varphi}}_s + 3H(\dot{\bar{\varphi}}_s - m_\phi\bar{\varphi}_c)] \sin(m_\phi t - m_\phi t_\star), \end{aligned} \quad (\text{A15})$$

which may be solved by solving the individual expressions in brackets as a set of two coupled differential equations. In brief, Ref. [121] defines an effective energy density and pressure

$$\bar{\rho}_{\phi,\text{ef}} \equiv \frac{1}{2} \left( \frac{1}{2} [\dot{\bar{\varphi}}_c^2 + \dot{\bar{\varphi}}_s^2] + m_\phi [\dot{\bar{\varphi}}_c \bar{\varphi}_s - \dot{\bar{\varphi}}_s \bar{\varphi}_c] + m_\phi^2 [\bar{\varphi}_s^2 + \bar{\varphi}_c^2] \right) \quad (\text{A16a})$$

$$\bar{P}_{\phi,\text{ef}} \equiv \frac{1}{2} \left( \frac{1}{2} [\dot{\bar{\varphi}}_c^2 + \dot{\bar{\varphi}}_s^2] + m_\phi [\dot{\bar{\varphi}}_c \bar{\varphi}_s - \dot{\bar{\varphi}}_s \bar{\varphi}_c] \right) \quad (\text{A16b})$$

that, via the Klein-Gordon equation Eq. (A15), exactly satisfy the standard fluid conservation law

$$\dot{\bar{\rho}}_{\phi,\text{ef}} = -3H(\bar{\rho}_{\phi,\text{ef}} + \bar{P}_{\phi,\text{ef}}). \quad (\text{A17})$$

In the scheme of Ref. [121], one solves the full Klein-Gordon equation Eq. (A12) until some transition time  $t_\star$  and matches onto the amplitudes  $\bar{\varphi}_c$  and  $\bar{\varphi}_s$  in order to evaluate the effective fluid energy density  $\bar{\rho}_{\phi,\text{ef}}$ . Matching error (due to oscillations of  $\rho_\phi$  about its time-averaged  $1/a^3$  redshifting) is minimized by choosing

$$\left. \frac{\ddot{\bar{\varphi}}_I}{\dot{\bar{\varphi}}_I} \right|_{t=t_\star} = -\frac{\langle H \rangle}{2} \left( 3 - \frac{2d\langle H \rangle/d\tau}{a\langle H \rangle^2} \right) \equiv \mathcal{M}. \quad (\text{A18})$$

for  $I = c, s$ . Here  $\langle H \rangle$  denotes the Hubble parameter averaged over the oscillations induced by the scalar's contribution to FLRW expansion; we may neglect such effects in practice and simply substitute  $H$ . Inserting the decomposed Klein-Gordon equation into Eq. (A18) and solving yields

$$\begin{pmatrix} \dot{\bar{\varphi}}_c \\ \dot{\bar{\varphi}}_s \end{pmatrix} = -\frac{3H}{\mathcal{M}^2 + 3H\mathcal{M} + 4m_\phi^2} \begin{pmatrix} 2m_\phi & 3H + \mathcal{M} \\ -\mathcal{M} & 2m_\phi \end{pmatrix} \begin{pmatrix} m_\phi \bar{\phi} \\ \dot{\bar{\phi}} \end{pmatrix} \quad (\text{A19})$$

and

$$\bar{\varphi}_c = \bar{\phi} \quad (\text{A20a})$$

$$\bar{\varphi}_s = \dot{\bar{\phi}}/m_\phi - \dot{\bar{\varphi}}_c/m_\phi. \quad (\text{A20b})$$

Ref. [121] finds these choices reduce the matching error between  $\bar{\rho}_\phi$  and  $\bar{\rho}_{\phi,\text{ef}}$  to  $\mathcal{O}([H_\star/m_\phi]^3)$ , where  $H_\star = H(t_\star)$ .

After matching, one solves the dynamics for the effective fluid approximation (efa) to the energy density  $\bar{\rho}_{\phi,\text{efa}}$ ,

$$\dot{\bar{\rho}}_{\phi,\text{efa}} = -3H(1 + w_{\phi,\text{efa}})\bar{\rho}_{\phi,\text{efa}}. \quad (\text{A21})$$

At late times,  $\bar{\rho}_\phi$  redshifts like  $a^{-3}$  to good precision, motivating the choice  $w_{\phi,\text{efa}} = 0$ . However, optimal computational efficiency switches at as large of  $H_\star/m_\phi$  as possible, at which point the (average) equation of state and rate of redshift deviate appreciably from that of cold dark matter. Ref. [121] therefore calibrated a time-dependent ansatz for  $w_{\phi,\text{efa}} = 3(H/m_\phi)^2/2$ , informed by computing Eq. (A16) using numerical solutions to the Klein-Gordon equation. However, Ref. [121] focused on scalars that begin oscillating in the radiation era ( $m_\phi \gtrsim 10^{-28}$  eV), whereas for the scenarios relevant here, the scalars necessarily begin to oscillate in the matter era. Using numerical solutions, Ref. [121] demonstrated that  $w_{\phi,\text{ef}} \approx 3(H/m_\phi)^2/2$  for  $H \gg m_\phi$ , noting that the result could also be obtained by the analytic solution to the homogeneous Klein-Gordon equation in the radiation era. Since we are interested in lighter scalars (for which matching will occur in the matter era or during the onset of dark-energy domination), we extend this result to FLRW backgrounds with arbitrary equations of state.<sup>8</sup>

The Hubble parameter in a Universe with constant equation of state  $w$  is  $H(t) = n/t$ , where  $n = 2/3(1+w)$ . In such a background, the solution to the homogeneous Klein-Gordon equation (with constant field value at early times  $t \ll 1/m_\phi$ ) is  $\phi(t) \propto J_\nu(m_\phi t)/t^\nu$  where  $\nu = (3n-1)/2$ . Taking the asymptotic (i.e.,  $m_\phi t \gg 1$ ) expansion of the energy density and pressure for this solution (at next-to-leading order, to correctly compute the  $1/t^2$  term) yields  $w_{\phi,\text{ef}} = 3n/4(m_\phi t)^2 + \mathcal{O}[(m_\phi t)^{-4}]$ . In a multicomponent Universe (like  $\Lambda$ CDM), the instantaneous equation of state may be obtained by combining the Friedmann equations to give  $w(t) = -2\dot{H}(t)/3H(t)^2 - 1$ . Given that the fluid approximation is meant to be used only when  $m_\phi/H \gtrsim 10$ , approximating expansion as a power law at any given time should be wholly sufficient [barring exotic cosmologies with  $w(t)$  evolving on timescales much shorter than the Hubble scale]. As such, we may promote our single-component result above to a general Universe via

$$w_{\phi,\text{ef}} = -\frac{3}{4} \frac{\dot{H}}{m_\phi^2} \quad (\text{A22})$$

In practice, we find Eq. (A22) works exceedingly well. Since  $\dot{H} = -2H^2$  deep in the radiation era, it reproduces the results of Ref. [121] for transitions occurring well before matter-radiation equality. Moreover, for transitions occurring in the matter era, we observe even more rapid convergence, improving with  $(H_\star/m_\phi)^4$  for  $m_\phi \geq 10^{-28}$  eV compared to cubic convergence for transitions in the radiation era.

### *b. Perturbations*

In spite of the added complications that the equation of motion for  $\delta\phi$  depends on wave number  $k$  and is sourced by metric perturbations, the treatment for spatial perturbations proceeds similarly.

<sup>8</sup> Generalization to lighter masses is also of interest for future cosmological constraints on scalar subcomponents of dark matter with such masses [128, 139–142], given projected biases from fluid approximations for future CMB experiments from Ref. [212] (which considered masses greater than  $10^{-27}$  eV). It would also be interesting to extend the formalism of Ref. [121] to potentials with minima steeper than quadratic in  $\phi$ , as relevant to early dark energy [129–132, 214]; however, the computational impetus to do so is likely not nearly so severe because scalars in steeper potentials oscillate with a frequency that decreases as the field amplitude redshifts (see, e.g., Ref. [215]).



We briefly enumerate the corresponding definitions, referring to Ref. [121] for further discussion and justification. The perturbation is again decomposed onto oscillatory modes as

$$\delta\phi(t) = \delta\varphi_c(t) \cos(m_\phi t - m_\phi t_\star) + \delta\varphi_s(t) \sin(m_\phi t - m_\phi t_\star). \quad (\text{A23})$$

The effective fluid variables defined as

$$2\delta\rho_{\phi,\text{ef}} = \dot{\bar{\varphi}}_c \delta\dot{\varphi}_c + \dot{\bar{\varphi}}_s \delta\dot{\varphi}_s + m_\phi (\bar{\varphi}_s \delta\dot{\varphi}_c - \bar{\varphi}_c \delta\dot{\varphi}_s) + m_\phi (\dot{\bar{\varphi}}_c \delta\varphi_s - \dot{\bar{\varphi}}_s \delta\varphi_c) + 2m_\phi^2 [\bar{\varphi}_c \delta\varphi_c + \bar{\varphi}_s \delta\varphi_s] \quad (\text{A24a})$$

$$(\bar{\rho}_{\phi,\text{ef}} + \bar{P}_{\phi,\text{ef}}) \theta_{\phi,\text{ef}} = \frac{k^2}{2a} [(\dot{\bar{\varphi}}_c + m_\phi \bar{\varphi}_s) \delta\varphi_c + (\dot{\bar{\varphi}}_s - m_\phi \bar{\varphi}_c) \delta\varphi_s] \quad (\text{A24b})$$

$$\delta P_{\phi,\text{ef}} = \delta\rho_{\phi,\text{ef}} - m_\phi^2 [\bar{\varphi}_c \delta\varphi_c + \bar{\varphi}_s \delta\varphi_s] \quad (\text{A24c})$$

exactly satisfy the perturbed fluid equations

$$0 = \delta\rho'_{\phi,\text{ef}} + 3\mathcal{H}(\delta\rho_{\phi,\text{ef}} + \delta P_{\phi,\text{ef}}) + (\bar{\rho}_{\phi,\text{ef}} + \bar{P}_{\phi,\text{ef}}) \left( \theta_{\phi,\text{ef}} + \frac{h'}{2} \right) \quad (\text{A25a})$$

$$0 = \partial_\tau [(\bar{\rho} + \bar{P}) \theta_{\phi,\text{ef}}] + 4\mathcal{H}(\bar{\rho}_{\phi,\text{ef}} + \bar{P}_{\phi,\text{ef}}) \theta_{\phi,\text{ef}} - k^2 \delta P_{\phi,\text{ef}}. \quad (\text{A25b})$$

Matching proceeds identically to the background, i.e., using the analogous matching condition to Eq. (A18) and solving for  $\delta\varphi_c$ ,  $\delta\varphi_s$ , and their time derivatives in analogy to Eqs. (A19) and (A20a).

After matching (and computing  $\delta\phi$  and  $\theta_\phi$  at  $t_\star$ ), one solves the effective fluid equations [205]

$$\delta'_\phi = -(1 + w_{\phi,\text{ef}}) \left( \theta_\phi + \frac{h'}{2} \right) - 3(c_s^2 - w_{\phi,\text{ef}}) \mathcal{H} \delta_\phi - 9\mathcal{H}^2 (1 + w_{\phi,\text{ef}}) (c_s^2 - c_a^2) \frac{\theta_\phi}{k^2} \quad (\text{A26a})$$

$$\theta'_\phi = -(1 - 3c_s^2) \mathcal{H} \theta_\phi + \frac{c_s^2 k^2}{1 + w_{\phi,\text{ef}}} \delta_\phi, \quad (\text{A26b})$$

where  $c_s^2$  is the rest-frame fluid sound speed and the “adiabatic sound speed” squared is

$$c_a^2 = w_{\phi,\text{ef}} - \frac{w'_{\phi,\text{ef}}}{3\mathcal{H}(1 + w_{\phi,\text{ef}})}. \quad (\text{A27})$$

Ref. [121] used a Wentzel-Kramers-Brillouin (WKB) approximation to compute an effective sound speed  $c_s^2 = (\sqrt{1 + \kappa^2} - 1)/\kappa$  (using the shorthand  $\kappa = k/am_\phi$ ) in the limit that expansion is negligible. Ref. [121] also calibrated an  $\mathcal{O}[(H/m_\phi)^2]$  correction to the squared sound speed, finding (empirically from numerical solutions) the coefficient to be 5/4, different from the factor 3/2 found for the equation of state that one might naively expect. We observe in addition that a coefficient 9/8 works well in the matter era. To reproduce both regimes, we take the ansatz

$$c_s^2 = \frac{\sqrt{1 + (k/am_\phi)^2} - 1}{k/am_\phi} - \frac{1}{4} \frac{\dot{H}}{m_\phi^2} + \frac{3}{4} \left( \frac{H}{m_\phi} \right)^2, \quad (\text{A28})$$

which we empirically observe works well across a wide range of masses.<sup>9</sup> We observe roughly an order-of-magnitude improvement in precision compared to using the sound speed from Ref. [121] (at the same  $H_\star/m_\phi$ ) for scalars that begin oscillating in the matter era. We defer a more thorough investigation of convergence and possible analytic justification for Eq. (A28) to future work.

<sup>9</sup> Curiously, the correction to the sound speed does coincide with that to equation of state [Eq. (A22)] in the matter era.

### 3. Initial conditions

We set initial conditions in the radiation era, when the scale factor evolves as  $a(\tau) = \sqrt{\Omega_r} H_0 \tau$ . The homogeneous equation of motion for the scalar has a slow-roll solution (i.e., where  $dV/d\phi$  is approximately constant) of

$$\bar{\phi}'(\tau) = -\frac{\Omega_r H_0^2}{5} \frac{dV}{d\phi} \tau^3. \quad (\text{A29})$$

In the superhorizon limit,  $h = C(k\tau)^2$ . While  $\bar{\phi}$  is slowly rolling in the radiation era, the superhorizon limit of the equation of motion for  $\delta\phi$  (i.e., at leading order in  $k\tau \ll 1$ ) is solved by

$$\delta\phi \approx C \frac{\Omega_r H_0^2}{210k^4} \frac{dV}{d\phi} (k\tau)^6. \quad (\text{A30})$$

Plugging the slow-roll solution Eq. (A29) and noting that

$$\bar{\rho}_\phi + \bar{P}_\phi = \frac{(\bar{\phi}')^2}{a^2}, \quad (\text{A31})$$

the corresponding initial conditions for the fluid variables are

$$\frac{\delta\phi}{C} \equiv \frac{\delta\rho_\phi}{C\bar{\rho}_\phi} = -\frac{\Omega_r H_0^2}{1050k^4 V(\bar{\phi})} \left( \frac{dV}{d\phi} \right)^2 (k\tau)^6 \quad (\text{A32})$$

$$\frac{\theta_\phi}{C} \equiv \frac{-k^2 \delta u_\phi}{C} = \frac{k^2 \delta\phi}{C\bar{\phi}'} = -\frac{k(k\tau)^3}{42}, \quad (\text{A33})$$

consistent with those in Ref. [131].

### 4. Implementation details

Finally, we mention a few nontrivial aspects of the implementation of the above formalism in CLASS, particularly related to switching solving schemes. To begin with, switching between solving the Klein-Gordon equation and effective fluid equations changes the system of equations (and degrees of freedom) that are solved for at some intermediate time, based on a condition that itself depends on the instantaneous value of a dynamical quantity (namely,  $H/m_\phi$ ). Aside from the fact that the exact time this transition occurs cannot be known in advanced (i.e., not without integrating the equations in question), performing such transition while using adaptive ordinary differential equation (ODE) integrations is tricky. In particular, the transition condition may be reached in the middle of an integration interval; changing the system of equations mid-step introduces discontinuities that violate the smoothness conditions required by ODE solvers. One must therefore execute the transition between integration steps. (ODE solvers evaluate the system of equations at multiple subintervals of each step.) However, when using “black box” integrators (i.e., where one passes a function that evaluates the differential equations to a solver routine that performs the entire integration from an initial condition until some endpoint, as implemented in CLASS) it is nontrivial to determine whether a function evaluation is the first evaluation of an integration step or some intermediate evaluation. When integrating the background cosmology, we therefore implement the switching logic in a callback method that CLASS’s integrator executes between integration step (i.e., the `background.sources` method, in which various derived quantities are tabulated). Still, we find that CLASS’s stiff (implicit) ODE solver still does not work with the above

procedure, requiring that we use its explicit Runge-Kutta method instead. This could be due to the resulting change in the Jacobian, which cannot be accounted for because the user cannot decide when the Jacobian is recomputed (and it is not recomputed every integration step). For the solution of perturbations, CLASS does have a built-in system for scheduling and executing approximation scheme transitions (used extensively for other sectors, e.g., tight-coupling approximations for the photon-baryon plasma). We therefore simply add another such approximation scheme to switch on the effective fluid treatment for scalar perturbations.

Several issues also arise due to CLASS's method for tabulating and interpolating the background cosmology. A standard feature of ODE solvers is so-called dense output, which combines function evaluations used for integration to additionally produce interpolating functions over solver steps. The interpolants are designed to be accurate to some high order in the step size (comparable to the accuracy of the integration itself). CLASS instead simply tabulates the results at fixed intervals in  $\ln a$  and constructs a cubic Hermite interpolant. This interpolation is therefore sensitive to the transition between the Klein-Gordon and effective fluid solutions, which can induce spurious errors in the interpolant that have a nonnegligible effect on later stages in CLASS's execution (discussed below). However, it is not tractable to simply specify that the background be tabulated with a smaller  $\ln a$  interval: CLASS restricts integration step sizes to be no larger than this interval, drastically increasing the runtime of the background solution. (Standard ODE solver libraries instead take as large of steps as the adaptive method permits and evaluates the dense output interpolants.) Decreasing the tabulation interval by just two orders of magnitude over the default [ $\Delta \ln a = \ln(a_0/a_i)/N \approx 8 \times 10^{-4}$ , where  $a_i/a_0 = 10^{-14}$  and  $N = 40,000$  by default] makes the background runtime comparable to that of the perturbations solution. Because intervals in physical time increase as  $\Delta t = \Delta \ln a / H$ , this tabulation becomes insufficient to accurately capture the scalar's oscillatory behavior when  $m_\phi \Delta t = \Delta \ln a \cdot m_\phi / H \gtrsim 1/10$ , which for the default parameters occurs when  $m_\phi / H \sim 100$ . Because of the drastic effect it has on subsequent calculations, we increase the default number of subintervals to  $N = 10^5$ , but even this is insufficient to efficiently and rigorously test the accuracy of the fluid approximation by comparing choices of  $m_\phi / H_\star$  as large as, say,  $10^4$ . This choice is, however, sufficient for a switching time  $m_\phi / H_\star = 10$  as we use in all results. The relative difference in, e.g., CMB spectra compared to solutions with larger  $m_\phi / H_\star$  is better than the  $10^{-3}$  level.

The errors from the inadequate tabulation of the background solution naturally propagate to the evolution of scalar perturbations and can qualitatively alter the dynamics if unmitigated. They also can trigger CLASS to crash when determining the sampling points in time at which to evaluate the CMB source functions (in the `perturbations.timesampling_for_sources` routine). To determine the time sampling required to capture the late ISW effect, CLASS estimates the metric growth rate, which factors in  $2a''/a - (a'/a)^2 = -a^2 \bar{P} / M_{\text{pl}}^2$ . In the matter era, the *only* contribution to  $\bar{P}$  is that from the scalar, which oscillates between  $\bar{\rho}$  and  $-\bar{\rho}$ . This metric is therefore strongly sensitive to any interpolation errors, which over the course of parameter sampling often triggered CLASS to crash due to invalid time sampling determined by this routine. To mitigate these issues, we implemented a smooth transition between the Klein-Gordon and effective fluid solutions. Namely, over some number of oscillations (specified by a parameter) after  $H$  drops below the specified threshold  $H_\star$ , we solve both the Klein-Gordon and effective fluid equations. In this intermediate interval, when computing the scalar's energy density and pressure, we average the results of the two methods with weights determined by a tanh-based window function in time. In effect, this procedure (exponentially) smoothly damps the effect of oscillations in the true (Klein-Gordon) solution before fully switching to solving the effective fluid equations alone. Since the perturbation matching requires knowing  $\bar{\varphi}_c$ ,  $\bar{\varphi}_s$ , their time derivatives, and  $\bar{\rho}_{\phi,\text{ef}}$  as well, we record these at the midpoint of this transition interval for use when matching perturbations. Note that we use still  $\bar{\rho}_{\phi,\text{ef}}$  and  $\bar{P}_{\phi,\text{ef}}$  when matching to effective fluid perturbations, *not* the weighted energy density and

pressure, which are only used in the Friedmann equations.

Finally, a minor complication arises from the effective equation of state  $w_{\phi,\text{ef}}$  [Eq. (A22)] depending on  $\dot{H}$ . The Friedmann equations set  $\dot{H} = -(\bar{\rho} + \bar{P})/2M_{\text{pl}}^2$ , but one does not know the pressure contribution from the scalar  $\bar{P}_{\phi,\text{ef}}$  without knowing the current value of  $w_{\phi,\text{ef}}$ . Since we only consider scenarios where the scalar contributes a subfraction of the total matter density, we simply iteratively compute  $\dot{H}$  (beginning by neglecting the scalar field’s pressure contribution) and  $w_{\phi,\text{ef}}$  until the values converge to a relative precision of  $10^{-12}$ .

## Appendix B: Parameter inference

### 1. Likelihoods

We use the implementation of the standard 2018 *Planck* likelihoods [75, 151] (PR3) in `clik` [216] with supporting data obtained from the *Planck* Legacy Archive [217]. For the high- $\ell$  likelihoods (covering  $30 \leq \ell < 2500$  in temperature and  $30 \leq \ell < 2000$  for  $E$ -mode polarization and temperature-polarization cross correlation) we use the `Plik_lite` (`plik_lite_v22.TTTEEE`) variant that is marginalized over the parameters of the foreground models. For the low- $\ell$  likelihoods ( $2 \leq \ell \leq 30$ ) we use `Commander` (`commander_dx12.v3.2.29`) for temperature and `SimAll` (`simall_100x143.offlike5.EE.Aplanck.B`) for  $E$ -mode polarization. Finally, we use *Planck*’s lensing autopower spectrum likelihood (`smicadx12.Dec5.ftl_mv2.ndclpp_p_teb.consext8`) over multipoles  $8 \leq L \leq 400$ .

We use BAO measurements from a variety of surveys. The Six-degree Field Galaxy Survey (6dFGS) [152] measured  $\theta_{\text{BAO}} = 0.327 \pm 0.0142$  at an effective sample redshift  $z = 0.106$ . Ref. [152] used fitting functions from Ref. [63] to compute  $r_d$ , which for their fiducial cosmology with  $h = 0.7$ ,  $\omega_b = 0.02227$ , and  $\Omega_m = 0.27$  gives  $d = 154.06$  Mpc, compared to 149.94 Mpc from CLASS. The 6dFGS measurement of  $\theta_{\text{BAO}} = 0.336 \pm 0.015$  (both the mean and standard deviation) is thus rescaled by  $149.94/154.06$ . The SDSS Main Galaxy Sample (MGS) DR7 provides a non-Gaussian likelihood for  $1/\theta_{\text{BAO}}$  evaluated at  $z = 0.15$  with tabulated values (specified relative to a fiducial value  $D_V/r_d = 638.95/148.69$ ) available in supplementary material to Ref. [153]. The BAO measurements from the Baryon Oscillation Spectroscopic Survey (BOSS) DR12 galaxies (at  $z = 0.38$  and  $0.51$ ) are a multivariate Gaussian likelihood for  $\theta_{\text{BAO},\perp}$  and  $\theta_{\text{BAO},\parallel}$  at each redshift [218]. Likewise, luminous red galaxies (LRGs) from the Extended Baryon Oscillation Spectroscopic Survey (eBOSS) DR16 [154, 155] provide a multivariate Gaussian likelihood for  $1/\theta_{\text{BAO},\perp}$  and  $1/\theta_{\text{BAO},\parallel}$  at  $z = 0.70$ . The latter are available on the SDSS-IV SVN Software Repository [219].

In addition to the former “standard” set of BAO measurements, we also implement Gaussian likelihoods for the BAO measurements from DESI DR1 [156–158] as tabulated in Table 1 of Ref. [156] (which has not yet been published at the time of writing). Ref. [156] notes that each redshift bin are effectively uncorrelated and the results from individual tracers are reasonably concordant, justifying their combination. Notably, rounding errors in Table 1 of Ref. [156] have a nonnegligible effect on the likelihoods. In particular, the effective redshift for the bright galaxy sample measurement of  $\theta_{\text{BAO}}$  is reported as 0.30, rounded from 0.295. The impact of the rounding error is notable, shifting the full DESI DR1 dataset’s preferred  $hr_d$  upward by about half a percent and  $a_{m-\Lambda}$  downward by nearly a percent. To our knowledge, at the time of writing the actual data are only available at Ref. [220].

Finally, we use the Pantheon [95], Pantheon+ [96, 97], and DES 5YR [159] measurements of the apparent magnitude [Eq. (2.33)] of type Ia supernovae. We also use a recent joint analysis of supernovae from numerous datasets, Union3 [160]. Per Ref. [96], SN Ia at redshifts less than  $10^{-2}$ , which are more sensitive to bias due to peculiar velocities and other effects, are excluded for

Pantheon+. The Pantheon+ dataset also includes Cepheid host distances from SH0ES [26] that can optionally be used as calibrators. Likelihoods are Gaussian in the distance moduli  $\mu = m - M_B$ , with measured values and covariance provided online [221–224].

## 2. Sampling methods

To generate posterior samples, we use Markov Chain Monte Carlo (MCMC) methods from the Python package `emcee` [194–196]. We utilize the ensemble move proposal based on kernel density estimation [225, 226], which (for the posteriors presented here) we find yields MCMC chains with shortest autocorrelation times of `emcee`’s methods. We sample with 80 walkers, chosen so that each step, which `emcee` performs in two batches, runs (unparallelized) likelihood evaluations on each of the 40 cores on the CPUs we use. Autocorrelation times (for sample parameters) span from  $\sim 7$  (for the best-constrained posteriors) to  $\sim 30$  steps (for, e.g., the varying-constant scenarios with a scalar, since  $F_\phi$  is poorly constrained, or for varying- $m_e$  when using only *Planck* data, for which the posteriors are broad). We sample for 5,000 steps or for 10,000 steps for those cases with more challenging posteriors, discard the first ten autocorrelation times’ worth of steps, and thin by one autocorrelation time. These choices ensure that reported posteriors include at least  $\sim 20,000 - 30,000$  independent samples, enough to draw robust posterior mass contours even in the presence of extremely strong correlations (e.g., Fig. 8) or parameters whose constraints only place upper limits (e.g.,  $F_\phi$ ). These sample sizes are entirely generous for one-dimensional marginalized posteriors and summary statistics thereof, which are all consistent among smaller subsamples of the full posterior.

Finally, we note that we checked the robustness of our results with CLASS’s default precision settings by comparing likelihood evaluations with increased precision over 1,000 samples of the posteriors for each scenario we consider. In all cases, for 95% of samples the logarithm of the high- $\ell$  Planck likelihood differs by  $\lesssim 0.15$  when increasing precision, and only 0.3 at most; the others deviate negligibly. Namely, the distribution of errors is no worse than that for  $\Lambda$ CDM at the default precision settings.

- 
- [1] S. Hannestad, Possible constraints on the time variation of the fine structure constant from cosmic microwave background data, *Phys. Rev. D* **60**, 023515 (1999), [arXiv:astro-ph/9810102](#).
  - [2] M. Kaplinghat, R. J. Scherrer, and M. S. Turner, Constraining variations in the fine structure constant with the cosmic microwave background, *Phys. Rev. D* **60**, 023516 (1999), [arXiv:astro-ph/9810133](#).
  - [3] P. P. Avelino, C. J. A. P. Martins, G. Rocha, and P. T. P. Viana, Looking for a varying alpha in the cosmic microwave background, *Phys. Rev. D* **62**, 123508 (2000), [arXiv:astro-ph/0008446](#).
  - [4] R. A. Battye, R. Crittenden, and J. Weller, Cosmic concordance and the fine structure constant, *Phys. Rev. D* **63**, 043505 (2001), [arXiv:astro-ph/0008265](#).
  - [5] P. P. Avelino, S. Esposito, G. Mangano, C. J. A. P. Martins, A. Melchiorri, G. Miele, O. Pisanti, G. Rocha, and P. T. P. Viana, Early universe constraints on a time varying fine structure constant, *Phys. Rev. D* **64**, 103505 (2001), [arXiv:astro-ph/0102144](#).
  - [6] S. J. Landau, D. D. Harari, and M. Zaldarriaga, Constraining nonstandard recombination: A worked example, *Phys. Rev. D* **63**, 083505 (2001).
  - [7] C. J. A. P. Martins, A. Melchiorri, G. Rocha, R. Trotta, P. P. Avelino, and P. T. P. Viana, Wmap constraints on varying alpha and the promise of reionization, *Phys. Lett. B* **585**, 29 (2004), [arXiv:astro-ph/0302295](#).
  - [8] G. Rocha, R. Trotta, C. J. A. P. Martins, A. Melchiorri, P. P. Avelino, R. Bean, and P. T. P. Viana, Measuring alpha in the early universe: cmb polarization, reionization and the fisher matrix analysis, *Mon. Not. Roy. Astron. Soc.* **352**, 20 (2004), [arXiv:astro-ph/0309211](#).

- [9] P. Stefanescu, Constraints on time variation of fine structure constant from WMAP-3yr data, *New Astron.* **12**, 635 (2007), [arXiv:0707.0190 \[astro-ph\]](#).
- [10] M. Nakashima, R. Nagata, and J. Yokoyama, Constraints on the time variation of the fine structure constant by the 5-year WMAP data, *Prog. Theor. Phys.* **120**, 1207 (2008), [arXiv:0810.1098 \[astro-ph\]](#).
- [11] E. Menegoni, S. Galli, J. G. Bartlett, C. J. A. P. Martins, and A. Melchiorri, New Constraints on variations of the fine structure constant from CMB anisotropies, *Phys. Rev. D* **80**, 087302 (2009), [arXiv:0909.3584 \[astro-ph.CO\]](#).
- [12] E. Menegoni, M. Archidiacono, E. Calabrese, S. Galli, C. J. A. P. Martins, and A. Melchiorri, The Fine Structure Constant and the CMB Damping Scale, *Phys. Rev. D* **85**, 107301 (2012), [arXiv:1202.1476 \[astro-ph.CO\]](#).
- [13] J. Kujat and R. J. Scherrer, The Effect of time variation in the Higgs vacuum expectation value on the cosmic microwave background, *Phys. Rev. D* **62**, 023510 (2000), [arXiv:astro-ph/9912174](#).
- [14] K. Ichikawa, T. Kanzaki, and M. Kawasaki, CMB constraints on the simultaneous variation of the fine structure constant and electron mass, *Phys. Rev. D* **74**, 023515 (2006), [arXiv:astro-ph/0602577](#).
- [15] S. J. Landau, M. E. Mosquera, C. G. Scoccola, and H. Vucetich, Early Universe Constraints on Time Variation of Fundamental Constants, *Phys. Rev. D* **78**, 083527 (2008), [arXiv:0809.2033 \[astro-ph\]](#).
- [16] C. G. Scoccola, S. J. Landau, and H. Vucetich, WMAP 5-year constraints on time variation of  $\alpha$  and  $m_e$  in a detailed recombination scenario, *Phys. Lett. B* **669**, 212 (2008), [arXiv:0809.5028 \[astro-ph\]](#).
- [17] M. Nakashima, K. Ichikawa, R. Nagata, and J. Yokoyama, Constraining the time variation of the coupling constants from cosmic microwave background: effect of  $\Lambda$ QCD, *JCAP* **01**, 030, [arXiv:0910.0742 \[astro-ph.CO\]](#).
- [18] S. J. Landau and C. G. Scoccola, Constraints on variation in  $\alpha$  and  $m_e$  from WMAP 7-year data, *Astron. Astrophys.* **517**, A62 (2010), [arXiv:1002.1603 \[astro-ph.CO\]](#).
- [19] C. G. Scoccola *et al.*, The clustering of galaxies in the SDSS-III Baryon Oscillation Spectroscopic Survey: constraints on the time variation of fundamental constants from the large-scale two-point correlation function, *Mon. Not. Roy. Astron. Soc.* **434**, 1792 (2013), [arXiv:1209.1394 \[astro-ph.CO\]](#).
- [20] L. Hart and J. Chluba, Updated fundamental constant constraints from Planck 2018 data and possible relations to the Hubble tension, *Mon. Not. Roy. Astron. Soc.* **493**, 3255 (2020), [arXiv:1912.03986 \[astro-ph.CO\]](#).
- [21] T. Sekiguchi and T. Takahashi, Early recombination as a solution to the  $H_0$  tension, *Phys. Rev. D* **103**, 083507 (2021), [arXiv:2007.03381 \[astro-ph.CO\]](#).
- [22] N. Schöneberg, G. Franco Abellán, A. Pérez Sánchez, S. J. Witte, V. Poulin, and J. Lesgourgues, The  $H_0$  Olympics: A fair ranking of proposed models, *Phys. Rept.* **984**, 1 (2022), [arXiv:2107.10291 \[astro-ph.CO\]](#).
- [23] A. R. Khalife, M. B. Zanjani, S. Galli, S. Günther, J. Lesgourgues, and K. Benabed, Review of Hubble tension solutions with new SH0ES and SPT-3G data, *JCAP* **04**, 059, [arXiv:2312.09814 \[astro-ph.CO\]](#).
- [24] A. G. Riess *et al.*, A 2.4% Determination of the Local Value of the Hubble Constant, *Astrophys. J.* **826**, 56 (2016), [arXiv:1604.01424 \[astro-ph.CO\]](#).
- [25] A. G. Riess, S. Casertano, W. Yuan, L. M. Macri, and D. Scolnic, Large Magellanic Cloud Cepheid Standards Provide a 1% Foundation for the Determination of the Hubble Constant and Stronger Evidence for Physics beyond  $\Lambda$ CDM, *Astrophys. J.* **876**, 85 (2019), [arXiv:1903.07603 \[astro-ph.CO\]](#).
- [26] A. G. Riess *et al.*, A Comprehensive Measurement of the Local Value of the Hubble Constant with 1 km s<sup>-1</sup> Mpc<sup>-1</sup> Uncertainty from the Hubble Space Telescope and the SH0ES Team, *Astrophys. J. Lett.* **934**, L7 (2022), [arXiv:2112.04510 \[astro-ph.CO\]](#).
- [27] L. W. H. Fung, L. Li, T. Liu, H. N. Luu, Y.-C. Qiu, and S. H. H. Tye, Hubble constant in the axi-Higgs universe, *Phys. Rev. Res.* **5**, L022059 (2023), [arXiv:2105.01631 \[astro-ph.CO\]](#).
- [28] L. W. H. Fung, L. Li, T. Liu, H. N. Luu, Y.-C. Qiu, and S. H. H. Tye, Axi-Higgs cosmology, *JCAP* **08**, 057, [arXiv:2102.11257 \[hep-ph\]](#).
- [29] H. N. Luu, Axion-Higgs cosmology: Cosmic microwave background and cosmological tensions, *Phys. Rev. D* **107**, 023513 (2023), [arXiv:2111.01347 \[astro-ph.CO\]](#).
- [30] R. Solomon, G. Agarwal, and D. Stojkovic, Environment dependent electron mass and the Hubble constant tension, *Phys. Rev. D* **105**, 103536 (2022), [arXiv:2201.03127 \[hep-ph\]](#).
- [31] K. Hoshiya and Y. Toda, Electron mass variation from dark sector interactions and compatibility with cosmological observations, *Phys. Rev. D* **107**, 043505 (2023), [arXiv:2202.07714 \[astro-ph.CO\]](#).
- [32] Baryakhtar, Masha and Simon, Olivier and Weiner, Zachary J., Searching for coupled, hyperlight



- scalars across cosmic history (2024), to appear.
- [33] H. Tohfa, J. Crump, E. Baker, L. Hart, D. Grin, M. Brosius, and J. Chluba, A cosmic microwave background search for fine-structure constant evolution, [arXiv:2307.06768 \[astro-ph.CO\]](#) (2023).
  - [34] N. Schöneberg, L. Vacher, J. D. F. Dias, M. M. C. D. Carvalho, and C. J. A. P. Martins, News from the Swampland — constraining string theory with astrophysics and cosmology, *JCAP* **10**, 039, [arXiv:2307.15060 \[astro-ph.CO\]](#).
  - [35] L. Vacher, N. Schöneberg, J. D. F. Dias, C. J. A. P. Martins, and F. Pimenta, Runaway dilaton models: Improved constraints from the full cosmological evolution, *Phys. Rev. D* **107**, 104002 (2023), [arXiv:2301.13500 \[astro-ph.CO\]](#).
  - [36] D. J. Fixsen, E. S. Cheng, J. M. Gales, J. C. Mather, R. A. Shafer, and E. L. Wright, The Cosmic Microwave Background spectrum from the full COBE FIRAS data set, *Astrophys. J.* **473**, 576 (1996), [arXiv:astro-ph/9605054](#).
  - [37] D. J. Fixsen, The Temperature of the Cosmic Microwave Background, *Astrophys. J.* **707**, 916 (2009), [arXiv:0911.1955 \[astro-ph.CO\]](#).
  - [38] M. M. Ivanov, Y. Ali-Haïmoud, and J. Lesgourgues, H0 tension or T0 tension?, *Phys. Rev. D* **102**, 063515 (2020), [arXiv:2005.10656 \[astro-ph.CO\]](#).
  - [39] F.-Y. Cyr-Racine, F. Ge, and L. Knox, Symmetry of Cosmological Observables, a Mirror World Dark Sector, and the Hubble Constant, *Phys. Rev. Lett.* **128**, 201301 (2022), [arXiv:2107.13000 \[astro-ph.CO\]](#).
  - [40] F. Ge, F.-Y. Cyr-Racine, and L. Knox, Scaling transformations and the origins of light relics constraints from cosmic microwave background observations, *Phys. Rev. D* **107**, 023517 (2023), [arXiv:2210.16335 \[astro-ph.CO\]](#).
  - [41] K. L. Greene and F.-Y. Cyr-Racine, Thomson scattering: one rate to rule them all, *JCAP* **10**, 065, [arXiv:2306.06165 \[astro-ph.CO\]](#).
  - [42] K. Akita and M. Yamaguchi, A precision calculation of relic neutrino decoupling, *JCAP* **08**, 012, [arXiv:2005.07047 \[hep-ph\]](#).
  - [43] J. Froustey, C. Pitrou, and M. C. Volpe, Neutrino decoupling including flavour oscillations and primordial nucleosynthesis, *JCAP* **12**, 015, [arXiv:2008.01074 \[hep-ph\]](#).
  - [44] J. J. Bennett, G. Buldgen, P. F. De Salas, M. Drewes, S. Gariazzo, S. Pastor, and Y. Y. Y. Wong, Towards a precision calculation of  $N_{\text{eff}}$  in the Standard Model II: Neutrino decoupling in the presence of flavour oscillations and finite-temperature QED, *JCAP* **04**, 073, [arXiv:2012.02726 \[hep-ph\]](#).
  - [45] M. Cielo, M. Escudero, G. Mangano, and O. Pisanti,  $N_{\text{eff}}$  in the Standard Model at NLO is 3.043, *Phys. Rev. D* **108**, L121301 (2023), [arXiv:2306.05460 \[hep-ph\]](#).
  - [46] J. Birrell, C.-T. Yang, and J. Rafelski, Relic Neutrino Freeze-out: Dependence on Natural Constants, *Nucl. Phys. B* **890**, 481 (2014), [arXiv:1406.1759 \[nucl-th\]](#).
  - [47] E. Grohs and G. M. Fuller, Insights into neutrino decoupling gleaned from considerations of the role of electron mass, *Nucl. Phys. B* **923**, 222 (2017), [arXiv:1706.03391 \[astro-ph.CO\]](#).
  - [48] K. N. Abazajian *et al.* (CMB-S4), CMB-S4 Science Book, First Edition, [arXiv:1610.02743 \[astro-ph.CO\]](#) (2016).
  - [49] K. Abazajian *et al.*, CMB-S4 Science Case, Reference Design, and Project Plan, [arXiv:1907.04473 \[astro-ph.IM\]](#) (2019).
  - [50] C. Dvorkin *et al.*, The Physics of Light Relics, in *Snowmass 2021* (2022) [arXiv:2203.07943 \[hep-ph\]](#).
  - [51] D. Blas, J. Lesgourgues, and T. Tram, The Cosmic Linear Anisotropy Solving System (CLASS) II: Approximation schemes, *JCAP* **07**, 034, [arXiv:1104.2933 \[astro-ph.CO\]](#).
  - [52] J. Lesgourgues, The Cosmic Linear Anisotropy Solving System (CLASS) I: Overview, [arXiv:1104.2932 \[astro-ph.IM\]](#) (2011).
  - [53] Y. Ali-Haïmoud and C. M. Hirata, HyRec: A fast and highly accurate primordial hydrogen and helium recombination code, *Phys. Rev. D* **83**, 043513 (2011), [arXiv:1011.3758 \[astro-ph.CO\]](#).
  - [54] N. Lee and Y. Ali-Haïmoud, HYREC-2: a highly accurate sub-millisecond recombination code, *Phys. Rev. D* **102**, 083517 (2020), [arXiv:2007.14114 \[astro-ph.CO\]](#).
  - [55] P. J. E. Peebles, Recombination of the Primeval Plasma, *Astrophys. J.* **153**, 1 (1968).
  - [56] P. J. E. Peebles and J. T. Yu, Primeval adiabatic perturbation in an expanding universe, *Astrophys. J.* **162**, 815 (1970).
  - [57] S. Seager, D. D. Sasselov, and D. Scott, A new calculation of the recombination epoch, *Astrophys. J. Lett.* **523**, L1 (1999), [arXiv:astro-ph/9909275](#).
  - [58] Y. Ali-Haïmoud and C. M. Hirata, Ultrafast effective multi-level atom method for primordial hydrogen

- recombination, *Phys. Rev. D* **82**, 063521 (2010), [arXiv:1006.1355 \[astro-ph.CO\]](#).
- [59] P. A. R. Ade *et al.* (Planck), Planck intermediate results - XXIV. Constraints on variations in fundamental constants, *Astron. Astrophys.* **580**, A22 (2015), [arXiv:1406.7482 \[astro-ph.CO\]](#).
  - [60] L. Hart and J. Chluba, New constraints on time-dependent variations of fundamental constants using Planck data, *Mon. Not. Roy. Astron. Soc.* **474**, 1850 (2018), [arXiv:1705.03925 \[astro-ph.CO\]](#).
  - [61] S. Weinberg, *Cosmology* (2008).
  - [62] D. Baumann, *Cosmology* (Cambridge University Press, 2022).
  - [63] D. J. Eisenstein and W. Hu, Baryonic features in the matter transfer function, *Astrophys. J.* **496**, 605 (1998), [arXiv:astro-ph/9709112](#).
  - [64] W. Hu and M. J. White, The Damping tail of CMB anisotropies, *Astrophys. J.* **479**, 568 (1997), [arXiv:astro-ph/9609079](#).
  - [65] W. Hu and N. Sugiyama, Small scale cosmological perturbations: An Analytic approach, *Astrophys. J.* **471**, 542 (1996), [arXiv:astro-ph/9510117](#).
  - [66] S. Vagnozzi, Consistency tests of  $\Lambda$ CDM from the early integrated Sachs-Wolfe effect: Implications for early-time new physics and the Hubble tension, *Phys. Rev. D* **104**, 063524 (2021), [arXiv:2105.10425 \[astro-ph.CO\]](#).
  - [67] A. Adil, A. Albrecht, and L. Knox, Quintessential cosmological tensions, *Phys. Rev. D* **107**, 063521 (2023), [arXiv:2207.10235 \[astro-ph.CO\]](#).
  - [68] W. T. Hu, *Wandering in the Background: A CMB Explorer*, Other thesis (1995), [arXiv:astro-ph/9508126](#).
  - [69] M. Zaldarriaga and D. D. Harari, Analytic approach to the polarization of the cosmic microwave background in flat and open universes, *Phys. Rev. D* **52**, 3276 (1995), [arXiv:astro-ph/9504085](#).
  - [70] W. Hu and M. J. White, A CMB polarization primer, *New Astron.* **2**, 323 (1997), [arXiv:astro-ph/9706147](#).
  - [71] B. Hadzhiyska and D. N. Spergel, Measuring the Duration of Last Scattering, *Phys. Rev. D* **99**, 043537 (2019), [arXiv:1808.04083 \[astro-ph.CO\]](#).
  - [72] D. W. Hogg, Distance measures in cosmology, [arXiv:astro-ph/9905116](#) (1999).
  - [73] M. Baes, P. Camps, and D. Van De Putte, Analytical expressions and numerical evaluation of the luminosity distance in a flat cosmology, *Mon. Not. Roy. Astron. Soc.* **468**, 927 (2017), [arXiv:1702.08860 \[astro-ph.CO\]](#).
  - [74] L. Knox and M. Millea, Hubble constant hunter's guide, *Phys. Rev. D* **101**, 043533 (2020), [arXiv:1908.03663 \[astro-ph.CO\]](#).
  - [75] N. Aghanim *et al.* (Planck), Planck 2018 results. VI. Cosmological parameters, *Astron. Astrophys.* **641**, A6 (2020), [Erratum: *Astron. Astrophys.* 652, C4 (2021)], [arXiv:1807.06209 \[astro-ph.CO\]](#).
  - [76] W. J. Percival *et al.* (2dFGRS Team), Parameter constraints for flat cosmologies from CMB and 2dFGRS power spectra, *Mon. Not. Roy. Astron. Soc.* **337**, 1068 (2002), [arXiv:astro-ph/0206256](#).
  - [77] C. Howlett, A. Lewis, A. Hall, and A. Challinor, CMB power spectrum parameter degeneracies in the era of precision cosmology, *JCAP* **04**, 027, [arXiv:1201.3654 \[astro-ph.CO\]](#).
  - [78] K. Jedamzik and L. Pogosian, Relieving the Hubble tension with primordial magnetic fields, *Phys. Rev. Lett.* **125**, 181302 (2020), [arXiv:2004.09487 \[astro-ph.CO\]](#).
  - [79] M. Rashkovetskyi, J. B. Muñoz, D. J. Eisenstein, and C. Dvorkin, Small-scale clumping at recombination and the Hubble tension, *Phys. Rev. D* **104**, 103517 (2021), [arXiv:2108.02747 \[astro-ph.CO\]](#).
  - [80] L. Thiele, Y. Guan, J. C. Hill, A. Kosowsky, and D. N. Spergel, Can small-scale baryon inhomogeneities resolve the Hubble tension? An investigation with ACT DR4, *Phys. Rev. D* **104**, 063535 (2021), [arXiv:2105.03003 \[astro-ph.CO\]](#).
  - [81] N. Lee and Y. Ali-Haïmoud, Probing small-scale baryon and dark matter isocurvature perturbations with cosmic microwave background anisotropies, *Phys. Rev. D* **104**, 103509 (2021), [arXiv:2108.07798 \[astro-ph.CO\]](#).
  - [82] M. Wyman, D. H. Rudd, R. A. Vanderveld, and W. Hu, Neutrinos Help Reconcile Planck Measurements with the Local Universe, *Phys. Rev. Lett.* **112**, 051302 (2014), [arXiv:1307.7715 \[astro-ph.CO\]](#).
  - [83] C. Dvorkin, M. Wyman, D. H. Rudd, and W. Hu, Neutrinos help reconcile Planck measurements with both the early and local Universe, *Phys. Rev. D* **90**, 083503 (2014), [arXiv:1403.8049 \[astro-ph.CO\]](#).
  - [84] J. L. Bernal, L. Verde, and A. G. Riess, The trouble with  $H_0$ , *JCAP* **10**, 019, [arXiv:1607.05617 \[astro-ph.CO\]](#).
  - [85] S. Bashinsky and U. Seljak, Neutrino perturbations in CMB anisotropy and matter clustering, *Phys.*

- [Rev. D \*\*69\*\*, 083002 \(2004\)](#), [arXiv:astro-ph/0310198](#).
- [86] Z. Hou, R. Keisler, L. Knox, M. Millea, and C. Reichardt, How Massless Neutrinos Affect the Cosmic Microwave Background Damping Tail, [Phys. Rev. D \*\*87\*\*, 083008 \(2013\)](#), [arXiv:1104.2333 \[astro-ph.CO\]](#).
  - [87] D. Baumann, D. Green, J. Meyers, and B. Wallisch, Phases of New Physics in the CMB, [JCAP \*\*01\*\*, 007, \[arXiv:1508.06342 \\[astro-ph.CO\\]\]\(#\)](#).
  - [88] Z. Pan, L. Knox, B. Mulroe, and A. Narimani, Cosmic Microwave Background Acoustic Peak Locations, [Mon. Not. Roy. Astron. Soc. \*\*459\*\*, 2513 \(2016\)](#), [arXiv:1603.03091 \[astro-ph.CO\]](#).
  - [89] R. K. Sachs and A. M. Wolfe, Perturbations of a cosmological model and angular variations of the microwave background, [Astrophys. J. \*\*147\*\*, 73 \(1967\)](#).
  - [90] J. Weller and A. M. Lewis, Large scale cosmic microwave background anisotropies and dark energy, [Mon. Not. Roy. Astron. Soc. \*\*346\*\*, 987 \(2003\)](#), [arXiv:astro-ph/0307104](#).
  - [91] A. Lewis and A. Challinor, Weak gravitational lensing of the CMB, [Phys. Rept. \*\*429\*\*, 1 \(2006\)](#), [arXiv:astro-ph/0601594](#).
  - [92] K. Thepsuriya and A. Lewis, Accuracy of cosmological parameters using the baryon acoustic scale, [JCAP \*\*01\*\*, 034, \[arXiv:1409.5066 \\[astro-ph.CO\\]\]\(#\)](#).
  - [93] N. Schöneberg, J. Lesgourgues, and D. C. Hooper, The BAO+BBN take on the Hubble tension, [JCAP \*\*10\*\*, 029, \[arXiv:1907.11594 \\[astro-ph.CO\\]\]\(#\)](#).
  - [94] J. L. Bernal, T. L. Smith, K. K. Boddy, and M. Kamionkowski, Robustness of baryon acoustic oscillation constraints for early-Universe modifications of  $\Lambda$ CDM cosmology, [Phys. Rev. D \*\*102\*\*, 123515 \(2020\)](#), [arXiv:2004.07263 \[astro-ph.CO\]](#).
  - [95] D. M. Scolnic *et al.* (Pan-STARRS1), The Complete Light-curve Sample of Spectroscopically Confirmed SNe Ia from Pan-STARRS1 and Cosmological Constraints from the Combined Pantheon Sample, [Astrophys. J. \*\*859\*\*, 101 \(2018\)](#), [arXiv:1710.00845 \[astro-ph.CO\]](#).
  - [96] D. Brout *et al.*, The Pantheon+ Analysis: Cosmological Constraints, [Astrophys. J. \*\*938\*\*, 110 \(2022\)](#), [arXiv:2202.04077 \[astro-ph.CO\]](#).
  - [97] D. Scolnic *et al.*, The Pantheon+ Analysis: The Full Data Set and Light-curve Release, [Astrophys. J. \*\*938\*\*, 113 \(2022\)](#), [arXiv:2112.03863 \[astro-ph.CO\]](#).
  - [98] T. M. Davis *et al.*, The Effect of Peculiar Velocities on Supernova Cosmology, [Astrophys. J. \*\*741\*\*, 67 \(2011\)](#), [arXiv:1012.2912 \[astro-ph.CO\]](#).
  - [99] T. M. Davis, S. R. Hinton, C. Howlett, and J. Calcino, Can redshift errors bias measurements of the Hubble Constant?, [Mon. Not. Roy. Astron. Soc. \*\*490\*\*, 2948 \(2019\)](#), [arXiv:1907.12639 \[astro-ph.CO\]](#).
  - [100] A. Carr, T. M. Davis, D. Scolnic, D. Scolnic, K. Said, D. Brout, E. R. Peterson, and R. Kessler, The Pantheon+ analysis: Improving the redshifts and peculiar velocities of Type Ia supernovae used in cosmological analyses, [Publ. Astron. Soc. Austral. \*\*39\*\*, e046 \(2022\)](#), [arXiv:2112.01471 \[astro-ph.CO\]](#).
  - [101] W. L. Freedman *et al.*, The Carnegie-Chicago Hubble Program. VIII. An Independent Determination of the Hubble Constant Based on the Tip of the Red Giant Branch, [Astrophys. J. \*\*882\*\*, 34 \(2019\)](#), [arXiv:1907.05922 \[astro-ph.CO\]](#).
  - [102] W. L. Freedman, B. F. Madore, T. Hoyt, I. S. Jang, R. Beaton, M. G. Lee, A. Monson, J. Neeley, and J. Rich, Calibration of the Tip of the Red Giant Branch (TRGB), [arXiv:2002.01550 \[astro-ph.GA\]](#) (2020).
  - [103] W. L. Freedman, Measurements of the Hubble Constant: Tensions in Perspective, [Astrophys. J. \*\*919\*\*, 16 \(2021\)](#), [arXiv:2106.15656 \[astro-ph.CO\]](#).
  - [104] W. L. Freedman and B. F. Madore, Progress in direct measurements of the Hubble constant, [JCAP \*\*11\*\*, 050, \[arXiv:2309.05618 \\[astro-ph.CO\\]\]\(#\)](#).
  - [105] B. Jain and U. Seljak, Cosmological model predictions for weak lensing: Linear and nonlinear regimes, [Astrophys. J. \*\*484\*\*, 560 \(1997\)](#), [arXiv:astro-ph/9611077](#).
  - [106] T. Abbott *et al.* (DES), Cosmology from cosmic shear with Dark Energy Survey Science Verification data, [Phys. Rev. D \*\*94\*\*, 022001 \(2016\)](#), [arXiv:1507.05552 \[astro-ph.CO\]](#).
  - [107] H. Hildebrandt *et al.*, KiDS-450: Cosmological parameter constraints from tomographic weak gravitational lensing, [Mon. Not. Roy. Astron. Soc. \*\*465\*\*, 1454 \(2017\)](#), [arXiv:1606.05338 \[astro-ph.CO\]](#).
  - [108] J. D. Bekenstein, Fine Structure Constant: Is It Really a Constant?, [Phys. Rev. D \*\*25\*\*, 1527 \(1982\)](#).
  - [109] T. Damour and J. F. Donoghue, Phenomenology of the Equivalence Principle with Light Scalars, [Class. Quant. Grav. \*\*27\*\*, 202001 \(2010\)](#), [arXiv:1007.2790 \[gr-qc\]](#).
  - [110] T. Damour and J. F. Donoghue, Equivalence Principle Violations and Couplings of a Light Dilaton, [Phys. Rev. D \*\*82\*\*, 084033 \(2010\)](#), [arXiv:1007.2792 \[gr-qc\]](#).

- [111] C. Brans and R. H. Dicke, Mach's principle and a relativistic theory of gravitation, *Phys. Rev.* **124**, 925 (1961).
- [112] J. Scherk and J. H. Schwarz, Dual Models for Nonhadrons, *Nucl. Phys. B* **81**, 118 (1974).
- [113] M. B. Green, J. H. Schwarz, and E. Witten, *Superstring Theory Vol. 2: 25th Anniversary Edition*, Cambridge Monographs on Mathematical Physics (Cambridge University Press, 2012).
- [114] T. R. Taylor and G. Veneziano, Dilaton Couplings at Large Distances, *Phys. Lett. B* **213**, 450 (1988).
- [115] Y. M. Cho, UNIFIED COSMOLOGY, *Phys. Rev. D* **41**, 2462 (1990).
- [116] T. Damour and A. M. Polyakov, String theory and gravity, *Gen. Rel. Grav.* **26**, 1171 (1994), [arXiv:gr-qc/9411069](#).
- [117] S. Dimopoulos and G. F. Giudice, Macroscopic forces from supersymmetry, *Phys. Lett. B* **379**, 105 (1996), [arXiv:hep-ph/9602350](#).
- [118] D. B. Kaplan and M. B. Wise, Couplings of a light dilaton and violations of the equivalence principle, *JHEP* **08**, 037, [arXiv:hep-ph/0008116](#).
- [119] M. Gasperini, F. Piazza, and G. Veneziano, Quintessence as a runaway dilaton, *Phys. Rev. D* **65**, 023508 (2002), [arXiv:gr-qc/0108016](#).
- [120] T. Damour, F. Piazza, and G. Veneziano, Runaway dilaton and equivalence principle violations, *Phys. Rev. Lett.* **89**, 081601 (2002), [arXiv:gr-qc/0204094](#).
- [121] S. Passaglia and W. Hu, Accurate effective fluid approximation for ultralight axions, *Phys. Rev. D* **105**, 123529 (2022), [arXiv:2201.10238 \[astro-ph.CO\]](#).
- [122] Zachary J. Weiner, *CLASS-ULS* (2023), branch class-uls-3.2.1, commit hash a5d05e4.
- [123] L. Senatore, S. Tassev, and M. Zaldarriaga, Cosmological Perturbations at Second Order and Recombination Perturbed, *JCAP* **08**, 031, [arXiv:0812.3652 \[astro-ph\]](#).
- [124] R. Khatri and B. D. Wandelt, Crinkles in the last scattering surface: Non-Gaussianity from inhomogeneous recombination, *Phys. Rev. D* **79**, 023501 (2009), [arXiv:0810.4370 \[astro-ph\]](#).
- [125] P. F. de Salas, D. V. Forero, S. Gariazzo, P. Martínez-Miravé, O. Mena, C. A. Ternes, M. Tórtola, and J. W. F. Valle, 2020 global reassessment of the neutrino oscillation picture, *JHEP* **02**, 071, [arXiv:2006.11237 \[hep-ph\]](#).
- [126] I. Esteban, M. C. Gonzalez-Garcia, M. Maltoni, T. Schwetz, and A. Zhou, The fate of hints: updated global analysis of three-flavor neutrino oscillations, *JHEP* **09**, 178, [arXiv:2007.14792 \[hep-ph\]](#).
- [127] F. Capozzi, E. Di Valentino, E. Lisi, A. Marrone, A. Melchiorri, and A. Palazzo, Global constraints on absolute neutrino masses and their ordering, *Phys. Rev. D* **95**, 096014 (2017), [Addendum: *Phys. Rev. D* **101**, 116013 (2020)], [arXiv:2003.08511 \[hep-ph\]](#).
- [128] R. Hlozek, D. Grin, D. J. E. Marsh, and P. G. Ferreira, A search for ultralight axions using precision cosmological data, *Phys. Rev. D* **91**, 103512 (2015), [arXiv:1410.2896 \[astro-ph.CO\]](#).
- [129] V. Poulin, T. L. Smith, T. Karwal, and M. Kamionkowski, Early Dark Energy Can Resolve The Hubble Tension, *Phys. Rev. Lett.* **122**, 221301 (2019), [arXiv:1811.04083 \[astro-ph.CO\]](#).
- [130] V. Poulin, T. L. Smith, D. Grin, T. Karwal, and M. Kamionkowski, Cosmological implications of ultralight axionlike fields, *Phys. Rev. D* **98**, 083525 (2018), [arXiv:1806.10608 \[astro-ph.CO\]](#).
- [131] T. L. Smith, V. Poulin, and M. A. Amin, Oscillating scalar fields and the Hubble tension: a resolution with novel signatures, *Phys. Rev. D* **101**, 063523 (2020), [arXiv:1908.06995 \[astro-ph.CO\]](#).
- [132] J. C. Hill, E. McDonough, M. W. Toomey, and S. Alexander, Early dark energy does not restore cosmological concordance, *Phys. Rev. D* **102**, 043507 (2020), [arXiv:2003.07355 \[astro-ph.CO\]](#).
- [133] V. Poulin, T. L. Smith, and T. Karwal, The Ups and Downs of Early Dark Energy solutions to the Hubble tension: A review of models, hints and constraints circa 2023, *Phys. Dark Univ.* **42**, 101348 (2023), [arXiv:2302.09032 \[astro-ph.CO\]](#).
- [134] W. Hu, R. Barkana, and A. Gruzinov, Cold and fuzzy dark matter, *Phys. Rev. Lett.* **85**, 1158 (2000), [arXiv:astro-ph/0003365](#).
- [135] L. Amendola and R. Barbieri, Dark matter from an ultra-light pseudo-Goldstone-boson, *Phys. Lett. B* **642**, 192 (2006), [arXiv:hep-ph/0509257](#).
- [136] D. J. E. Marsh, Axion Cosmology, *Phys. Rept.* **643**, 1 (2016), [arXiv:1510.07633 \[astro-ph.CO\]](#).
- [137] J. R. Bond, G. Efstathiou, and J. Silk, Massive Neutrinos and the Large Scale Structure of the Universe, *Phys. Rev. Lett.* **45**, 1980 (1980).
- [138] J. Lesgourgues and S. Pastor, Massive neutrinos and cosmology, *Phys. Rept.* **429**, 307 (2006), [arXiv:astro-ph/0603494](#).
- [139] K. K. Rogers, R. Hlozek, A. Laguë, M. M. Ivanov, O. H. E. Philcox, G. Cabass, K. Akitsu, and D. J. E.



- Marsh, Ultra-light axions and the  $S_8$  tension: joint constraints from the cosmic microwave background and galaxy clustering, *JCAP* **06**, 023, [arXiv:2301.08361 \[astro-ph.CO\]](#).
- [140] R. Hložek, D. J. E. Marsh, D. Grin, R. Allison, J. Dunkley, and E. Calabrese, Future CMB tests of dark matter: Ultralight axions and massive neutrinos, *Phys. Rev. D* **95**, 123511 (2017), [arXiv:1607.08208 \[astro-ph.CO\]](#).
  - [141] R. Hložek, D. J. E. Marsh, and D. Grin, Using the Full Power of the Cosmic Microwave Background to Probe Axion Dark Matter, *Mon. Not. Roy. Astron. Soc.* **476**, 3063 (2018), [arXiv:1708.05681 \[astro-ph.CO\]](#).
  - [142] A. Laguë, J. R. Bond, R. Hložek, K. K. Rogers, D. J. E. Marsh, and D. Grin, Constraining ultralight axions with galaxy surveys, *JCAP* **01** (01), 049, [arXiv:2104.07802 \[astro-ph.CO\]](#).
  - [143] E. Abdalla *et al.*, Cosmology intertwined: A review of the particle physics, astrophysics, and cosmology associated with the cosmological tensions and anomalies, *JHEAp* **34**, 49 (2022), [arXiv:2203.06142 \[astro-ph.CO\]](#).
  - [144] S. M. L. Vogt, D. J. E. Marsh, and A. Laguë, Improved mixed dark matter halo model for ultralight axions, *Phys. Rev. D* **107**, 063526 (2023), [arXiv:2209.13445 \[astro-ph.CO\]](#).
  - [145] A. Laguë, B. Schwabe, R. Hložek, D. J. E. Marsh, and K. K. Rogers, Cosmological simulations of mixed ultralight dark matter, *Phys. Rev. D* **109**, 043507 (2024), [arXiv:2310.20000 \[astro-ph.CO\]](#).
  - [146] D. J. E. Marsh, WarmAndFuzzy: the halo model beyond CDM, [arXiv:1605.05973 \[astro-ph.CO\]](#) (2016).
  - [147] J. B. Bauer, D. J. E. Marsh, R. Hložek, H. Padmanabhan, and A. Laguë, Intensity Mapping as a Probe of Axion Dark Matter, *Mon. Not. Roy. Astron. Soc.* **500**, 3162 (2020), [arXiv:2003.09655 \[astro-ph.CO\]](#).
  - [148] H. Ooguri and C. Vafa, On the Geometry of the String Landscape and the Swampland, *Nucl. Phys. B* **766**, 21 (2007), [arXiv:hep-th/0605264](#).
  - [149] K. A. Olive and M. Pospelov, Evolution of the fine structure constant driven by dark matter and the cosmological constant, *Phys. Rev. D* **65**, 085044 (2002), [arXiv:hep-ph/0110377](#).
  - [150] K. A. Olive and M. Pospelov, Environmental dependence of masses and coupling constants, *Phys. Rev. D* **77**, 043524 (2008), [arXiv:0709.3825 \[hep-ph\]](#).
  - [151] N. Aghanim *et al.* (Planck), Planck 2018 results. V. CMB power spectra and likelihoods, *Astron. Astrophys.* **641**, A5 (2020), [arXiv:1907.12875 \[astro-ph.CO\]](#).
  - [152] F. Beutler, C. Blake, M. Colless, D. H. Jones, L. Staveley-Smith, L. Campbell, Q. Parker, W. Saunders, and F. Watson, The 6dF Galaxy Survey: Baryon Acoustic Oscillations and the Local Hubble Constant, *Mon. Not. Roy. Astron. Soc.* **416**, 3017 (2011), [arXiv:1106.3366 \[astro-ph.CO\]](#).
  - [153] A. J. Ross, L. Samushia, C. Howlett, W. J. Percival, A. Burden, and M. Manera, The clustering of the SDSS DR7 main Galaxy sample – I. A 4 per cent distance measure at  $z = 0.15$ , *Mon. Not. Roy. Astron. Soc.* **449**, 835 (2015), [arXiv:1409.3242 \[astro-ph.CO\]](#).
  - [154] J. E. Bautista *et al.* (eBOSS), The Completed SDSS-IV extended Baryon Oscillation Spectroscopic Survey: measurement of the BAO and growth rate of structure of the luminous red galaxy sample from the anisotropic correlation function between redshifts 0.6 and 1, *Mon. Not. Roy. Astron. Soc.* **500**, 736 (2020), [arXiv:2007.08993 \[astro-ph.CO\]](#).
  - [155] H. Gil-Marín *et al.* (eBOSS), The Completed SDSS-IV extended Baryon Oscillation Spectroscopic Survey: measurement of the BAO and growth rate of structure of the luminous red galaxy sample from the anisotropic power spectrum between redshifts 0.6 and 1.0, *Mon. Not. Roy. Astron. Soc.* **498**, 2492 (2020), [arXiv:2007.08994 \[astro-ph.CO\]](#).
  - [156] A. G. Adame *et al.* (DESI), DESI 2024 VI: Cosmological Constraints from the Measurements of Baryon Acoustic Oscillations, [arXiv:2404.03002 \[astro-ph.CO\]](#) (2024).
  - [157] A. G. Adame *et al.* (DESI), DESI 2024 IV: Baryon Acoustic Oscillations from the Lyman Alpha Forest, [arXiv:2404.03001 \[astro-ph.CO\]](#) (2024).
  - [158] A. G. Adame *et al.* (DESI), DESI 2024 III: Baryon Acoustic Oscillations from Galaxies and Quasars, [arXiv:2404.03000 \[astro-ph.CO\]](#) (2024).
  - [159] T. M. C. Abbott *et al.* (DES), The Dark Energy Survey: Cosmology Results With  $\sim 1500$  New High-redshift Type Ia Supernovae Using The Full 5-year Dataset, [arXiv:2401.02929 \[astro-ph.CO\]](#) (2024).
  - [160] D. Rubin *et al.*, Union Through UNITY: Cosmology with 2,000 SNe Using a Unified Bayesian Framework, [arXiv:2311.12098 \[astro-ph.CO\]](#) (2023).
  - [161] D. N. Spergel *et al.* (WMAP), First year Wilkinson Microwave Anisotropy Probe (WMAP) observations: Determination of cosmological parameters, *Astrophys. J. Suppl.* **148**, 175 (2003), [arXiv:astro-](#)

- ph/0302209.
- [162] G. Efstathiou, Y.-Z. Ma, and D. Hanson, Large-Angle Correlations in the Cosmic Microwave Background, *Mon. Not. Roy. Astron. Soc.* **407**, 2530 (2010), [arXiv:0911.5399 \[astro-ph.CO\]](#).
  - [163] C. J. Copi, D. Huterer, D. J. Schwarz, and G. D. Starkman, Large angle anomalies in the CMB, *Adv. Astron.* **2010**, 847541 (2010), [arXiv:1004.5602 \[astro-ph.CO\]](#).
  - [164] C. J. Copi, D. Huterer, D. J. Schwarz, and G. D. Starkman, Large-scale alignments from WMAP and Planck, *Mon. Not. Roy. Astron. Soc.* **449**, 3458 (2015), [arXiv:1311.4562 \[astro-ph.CO\]](#).
  - [165] C. J. Copi, M. O'Dwyer, and G. D. Starkman, The ISW effect and the lack of large-angle CMB temperature correlations, *Mon. Not. Roy. Astron. Soc.* **463**, 3305 (2016), [arXiv:1605.09732 \[astro-ph.CO\]](#).
  - [166] Y. Akrami *et al.* (Planck), Planck 2018 results. VII. Isotropy and Statistics of the CMB, *Astron. Astrophys.* **641**, A7 (2020), [arXiv:1906.02552 \[astro-ph.CO\]](#).
  - [167] E. Calabrese, A. Slosar, A. Melchiorri, G. F. Smoot, and O. Zahn, Cosmic Microwave Weak lensing data as a test for the dark universe, *Phys. Rev. D* **77**, 123531 (2008), [arXiv:0803.2309 \[astro-ph\]](#).
  - [168] N. Aghanim *et al.* (Planck), Planck intermediate results. LI. Features in the cosmic microwave background temperature power spectrum and shifts in cosmological parameters, *Astron. Astrophys.* **607**, A95 (2017), [arXiv:1608.02487 \[astro-ph.CO\]](#).
  - [169] P. Motloch and W. Hu, Lensinglike tensions in the *Planck* legacy release, *Phys. Rev. D* **101**, 083515 (2020), [arXiv:1912.06601 \[astro-ph.CO\]](#).
  - [170] S. Aiola *et al.* (ACT), The Atacama Cosmology Telescope: DR4 Maps and Cosmological Parameters, *JCAP* **12**, 047, [arXiv:2007.07288 \[astro-ph.CO\]](#).
  - [171] D. Dutcher *et al.* (SPT-3G), Measurements of the E-mode polarization and temperature-E-mode correlation of the CMB from SPT-3G 2018 data, *Phys. Rev. D* **104**, 022003 (2021), [arXiv:2101.01684 \[astro-ph.CO\]](#).
  - [172] L. Balkenhol *et al.* (SPT-3G), Measurement of the CMB temperature power spectrum and constraints on cosmology from the SPT-3G 2018 TT, TE, and EE dataset, *Phys. Rev. D* **108**, 023510 (2023), [arXiv:2212.05642 \[astro-ph.CO\]](#).
  - [173] S. Alam *et al.* (eBOSS), Completed SDSS-IV extended Baryon Oscillation Spectroscopic Survey: Cosmological implications from two decades of spectroscopic surveys at the Apache Point Observatory, *Phys. Rev. D* **103**, 083533 (2021), [arXiv:2007.08991 \[astro-ph.CO\]](#).
  - [174] E. Aubourg *et al.* (BOSS), Cosmological implications of baryon acoustic oscillation measurements, *Phys. Rev. D* **92**, 123516 (2015), [arXiv:1411.1074 \[astro-ph.CO\]](#).
  - [175] T. Delubac *et al.* (BOSS), Baryon acoustic oscillations in the Ly $\alpha$  forest of BOSS DR11 quasars, *Astron. Astrophys.* **574**, A59 (2015), [arXiv:1404.1801 \[astro-ph.CO\]](#).
  - [176] G. E. Addison, D. J. Watts, C. L. Bennett, M. Halpern, G. Hinshaw, and J. L. Weiland, Elucidating  $\Lambda$ CDM: Impact of Baryon Acoustic Oscillation Measurements on the Hubble Constant Discrepancy, *Astrophys. J.* **853**, 119 (2018), [arXiv:1707.06547 \[astro-ph.CO\]](#).
  - [177] A. Cuceu, J. Farr, P. Lemos, and A. Font-Ribera, Baryon Acoustic Oscillations and the Hubble Constant: Past, Present and Future, *JCAP* **10**, 044, [arXiv:1906.11628 \[astro-ph.CO\]](#).
  - [178] M. Cortès and A. R. Liddle, On dataset tensions and signatures of new cosmological physics, *Mon. Not. Roy. Astron. Soc.* **531**, L52 (2024), [arXiv:2309.03286 \[astro-ph.CO\]](#).
  - [179] G. Efstathiou, To  $H_0$  or not to  $H_0$ ?, *Mon. Not. Roy. Astron. Soc.* **505**, 3866 (2021), [arXiv:2103.08723 \[astro-ph.CO\]](#).
  - [180] D. Camarena and V. Marra, On the use of the local prior on the absolute magnitude of Type Ia supernovae in cosmological inference, *Mon. Not. Roy. Astron. Soc.* **504**, 5164 (2021), [arXiv:2101.08641 \[astro-ph.CO\]](#).
  - [181] Y. Wen, D. Scott, R. Sullivan, and J. P. Zibin, Role of  $T_0$  in CMB anisotropy measurements, *Phys. Rev. D* **104**, 043516 (2021), [arXiv:2011.09616 \[astro-ph.CO\]](#).
  - [182] J. Carron, A. Lewis, and G. Fabbian, Planck integrated Sachs-Wolfe-lensing likelihood and the CMB temperature, *Phys. Rev. D* **106**, 103507 (2022), [arXiv:2209.07395 \[astro-ph.CO\]](#).
  - [183] P. A. R. Ade *et al.* (Planck), Planck 2015 results. XXIV. Cosmology from Sunyaev-Zeldovich cluster counts, *Astron. Astrophys.* **594**, A24 (2016), [arXiv:1502.01597 \[astro-ph.CO\]](#).
  - [184] T. de Haan *et al.* (SPT), Cosmological Constraints from Galaxy Clusters in the 2500 square-degree SPT-SZ Survey, *Astrophys. J.* **832**, 95 (2016), [arXiv:1603.06522 \[astro-ph.CO\]](#).
  - [185] G. Efstathiou and J. R. Bond, Cosmic confusion: Degeneracies among cosmological parameters derived



- from measurements of microwave background anisotropies, *Mon. Not. Roy. Astron. Soc.* **304**, 75 (1999), [arXiv:astro-ph/9807103](#).
- [186] A. Kosowsky, M. Milosavljevic, and R. Jimenez, Efficient cosmological parameter estimation from microwave background anisotropies, *Phys. Rev. D* **66**, 063007 (2002), [arXiv:astro-ph/0206014](#).
  - [187] P. Ade *et al.* (Simons Observatory), The Simons Observatory: Science goals and forecasts, *JCAP* **02**, 056, [arXiv:1808.07445 \[astro-ph.CO\]](#).
  - [188] E. Rosenberg, S. Gratton, and G. Efstathiou, CMB power spectra and cosmological parameters from Planck PR4 with CamSpec, *Mon. Not. Roy. Astron. Soc.* **517**, 4620 (2022), [arXiv:2205.10869 \[astro-ph.CO\]](#).
  - [189] M. Tristram *et al.*, Cosmological parameters derived from the final Planck data release (PR4), *Astron. Astrophys.* **682**, A37 (2024), [arXiv:2309.10034 \[astro-ph.CO\]](#).
  - [190] T. Karwal, M. Raveri, B. Jain, J. Khoury, and M. Trodden, Chameleon early dark energy and the Hubble tension, *Phys. Rev. D* **105**, 063535 (2022), [arXiv:2106.13290 \[astro-ph.CO\]](#).
  - [191] M.-X. Lin, E. McDonough, J. C. Hill, and W. Hu, Dark matter trigger for early dark energy coincidence, *Phys. Rev. D* **107**, 103523 (2023), [arXiv:2212.08098 \[astro-ph.CO\]](#).
  - [192] J. Sakstein and M. Trodden, Early Dark Energy from Massive Neutrinos as a Natural Resolution of the Hubble Tension, *Phys. Rev. Lett.* **124**, 161301 (2020), [arXiv:1911.11760 \[astro-ph.CO\]](#).
  - [193] M. Carrillo González, Q. Liang, J. Sakstein, and M. Trodden, Neutrino-Assisted Early Dark Energy: Theory and Cosmology, *JCAP* **04**, 063, [arXiv:2011.09895 \[astro-ph.CO\]](#).
  - [194] D. Foreman-Mackey, D. W. Hogg, D. Lang, and J. Goodman, emcee: The MCMC Hammer, *Publ. Astron. Soc. Pac.* **125**, 306 (2013), [arXiv:1202.3665 \[astro-ph.IM\]](#).
  - [195] D. W. Hogg and D. Foreman-Mackey, Data analysis recipes: Using Markov Chain Monte Carlo, *Astrophys. J. Suppl.* **236**, 11 (2018), [arXiv:1710.06068 \[astro-ph.IM\]](#).
  - [196] D. Foreman-Mackey, W. Farr, M. Sinha, A. Archibald, D. Hogg, J. Sanders, J. Zuntz, P. Williams, A. Nelson, M. de Val-Borro, T. Erhardt, I. Pashchenko, and O. Pla, Emcee v3: A Python ensemble sampling toolkit for affine-invariant MCMC, *Journal of Open Source Software* **4**, 1864 (2019).
  - [197] D. Foreman-Mackey, corner.py: Scatterplot matrices in python, *Journal of Open Source Software* **1**, 24 (2016).
  - [198] C. R. Harris *et al.*, Array programming with NumPy, *Nature* **585**, 357 (2020), [arXiv:2006.10256 \[cs.MS\]](#).
  - [199] P. Virtanen *et al.*, SciPy 1.0–Fundamental Algorithms for Scientific Computing in Python, *Nature Meth.* **17**, 261 (2020), [arXiv:1907.10121 \[cs.MS\]](#).
  - [200] J. D. Hunter, Matplotlib: A 2D Graphics Environment, *Comput. Sci. Eng.* **9**, 90 (2007).
  - [201] S. Hoyer and J. Hamman, xarray: N-D labeled arrays and datasets in Python, *Journal of Open Research Software* **5**, 10.5334/jors.148 (2017).
  - [202] R. Kumar, C. Carroll, A. Hartikainen, and O. Martin, Arviz a unified library for exploratory analysis of bayesian models in python, *Journal of Open Source Software* **4**, 1143 (2019).
  - [203] A. Meurer *et al.*, SymPy: symbolic computing in Python, *PeerJ Comput. Sci.* **3**, e103 (2017).
  - [204] E. van der Velden, CMasher: Scientific colormaps for making accessible, informative and 'cmashing' plots, *The Journal of Open Source Software* **5**, 2004 (2020), [arXiv:2003.01069 \[eess.IV\]](#).
  - [205] W. Hu, Structure formation with generalized dark matter, *Astrophys. J.* **506**, 485 (1998), [arXiv:astro-ph/9801234](#).
  - [206] J.-c. Hwang and H. Noh, Axion as a Cold Dark Matter candidate, *Phys. Lett. B* **680**, 1 (2009), [arXiv:0902.4738 \[astro-ph.CO\]](#).
  - [207] D. J. E. Marsh and P. G. Ferreira, Ultra-Light Scalar Fields and the Growth of Structure in the Universe, *Phys. Rev. D* **82**, 103528 (2010), [arXiv:1009.3501 \[hep-ph\]](#).
  - [208] H. Winch, R. Hlozek, D. J. E. Marsh, D. Grin, and K. Rogers, Extreme Axions Unveiled: a Novel Fluid Approach for Cosmological Modeling, [arXiv:2311.02052 \[astro-ph.CO\]](#) (2023).
  - [209] R. Bean and O. Dore, Probing dark energy perturbations: The Dark energy equation of state and speed of sound as measured by WMAP, *Phys. Rev. D* **69**, 083503 (2004), [arXiv:astro-ph/0307100](#).
  - [210] G. Ballesteros and J. Lesgourgues, Dark energy with non-adiabatic sound speed: initial conditions and detectability, *JCAP* **10**, 014, [arXiv:1004.5509 \[astro-ph.CO\]](#).
  - [211] L. A. Ureña López and A. X. Gonzalez-Morales, Towards accurate cosmological predictions for rapidly oscillating scalar fields as dark matter, *JCAP* **07**, 048, [arXiv:1511.08195 \[astro-ph.CO\]](#).
  - [212] T. Cookmeyer, J. Cookmeyer, D. Grin, and T. L. Smith, How sound are our ultralight axion approxi-

- mations?, *Phys. Rev. D* **101**, 023501 (2020), [arXiv:1909.11094 \[astro-ph.CO\]](#).
- [213] C.-P. Ma and E. Bertschinger, Cosmological perturbation theory in the synchronous and conformal Newtonian gauges, *Astrophys. J.* **455**, 7 (1995), [arXiv:astro-ph/9506072](#).
  - [214] M. M. Ivanov, E. McDonough, J. C. Hill, M. Simonović, M. W. Toomey, S. Alexander, and M. Zaldarriaga, Constraining Early Dark Energy with Large-Scale Structure, *Phys. Rev. D* **102**, 103502 (2020), [arXiv:2006.11235 \[astro-ph.CO\]](#).
  - [215] P. Agrawal, F.-Y. Cyr-Racine, D. Pinner, and L. Randall, Rock ‘n’ roll solutions to the Hubble tension, *Phys. Dark Univ.* **42**, 101347 (2023), [arXiv:1904.01016 \[astro-ph.CO\]](#).
  - [216] Planck Collaboration, [clik](#) (2018), commit hash 8eae5bd5.
  - [217] Planck Collaboration, [Planck Legacy Archive](#) (2018), baseline release 3.00.
  - [218] S. Alam *et al.* (BOSS), The clustering of galaxies in the completed SDSS-III Baryon Oscillation Spectroscopic Survey: cosmological analysis of the DR12 galaxy sample, *Mon. Not. Roy. Astron. Soc.* **470**, 2617 (2017), [arXiv:1607.03155 \[astro-ph.CO\]](#).
  - [219] SDSS collaboration, [SDSS-IV SVN Software Repository, Data Release 16](#) (2020), accessed 2023.
  - [220] DESI collaboration, [DESI DR1 dataset](#) (2024), commit hash af68b10.
  - [221] Pantheon collaboration, [Pantheon data release repository](#) (2018), commit hash 7eb29dc.
  - [222] Pantheon and SH0ES collaborations, [Pantheon+SH0ES DataRelease repository](#) (2022), commit hash 1083557.
  - [223] DES collaboration, [DES-SN5YR repository](#) (2024), commit hash f254460.
  - [224] Rubin, D. et. al., [Union3 dataset](#) (2024), commit hash 261e356.
  - [225] B. Farr, V. Kalogera, and E. Lijten, A more efficient approach to parallel-tempered Markov-chain Monte Carlo for the highly structured posteriors of gravitational-wave signals, *Phys. Rev. D* **90**, 024014 (2014), [arXiv:1309.7709 \[astro-ph.IM\]](#).
  - [226] B. Farr and W. M. Farr, *kombine*: a kernel-density-based, embarrassingly parallel ensemble sampler (2015), in prep.